eman ta zabal zazu

Universidad del País Vasco
Euskal Herriko Unibertsitatea

Manipulating Superconductivity at the Nanoscale through Magnetism and Proximity Effects

DOCTORAL THESIS by:

Stefano Trivini

Thesis Supervisor:
José Ignacio Pascual

Thesis Tutor:
José María Pitarke

May 2023

This Thesis has been carried out at CIC nanoGUNE BRTA

To my beloved Family

Our virtues and our failings are inseparable, like force and matter.
When they separate, man is no more.
Nikola Tesla

Abstract

Superconductivity is an intriguing phenomenon that crosses many fields of science with still very high interest in fundamental understanding and technology applications. Electron-electron interactions and correlations are a basic interest of condensed matter physics, in fact, they describe many phenomena including magnetism and superconductivity. In this thesis, with Ultra-High-Vacuum material synthesis we couple normal metals, superconductors, 2D materials, magnetic atoms, and molecules to study the interplay of different properties transferred by proximity at the atomic scale described within various theoretical frameworks.

The interaction of a magnetic atom with a superconductor can be described classically following the well-established Yu-Shiba-Rusinov treatment. Here, we build 2D diluted atomic lattices of Mn on the β-Bi_2Pd superconductor by means of scanning tunneling microscope (STM) atomic manipulation. The anisotropic Fermi surface of β-Bi_2Pd implies a strong dependence of the coupling on the orientation of the build structures. In cross-like structures made by 5 Mn atoms, we observe an increasing splitting while composing the cross and a different splitting depending on the orientation with respect to the substrate. In an atomically built 25 Mn atoms squared lattice, we identify three YSR collective modes. The simple model simulations reproduce the three main contributions in which spatial distribution is correlated with the experimental dIdV maps.

In this thesis, we also show how tunneling a single electron can excite a pair-breaking excitation in a proximitized gold film in the presence of magnetic impurities. Combining STM with theoretical modeling, we map the excitation spectrum of an Fe-porphyrin molecule on the proximitized surface into a manifold of entangled Yu-Shiba-Rusinov and spin excitations. Pair excitations emerge in the tunneling spectra as peaks outside the spectral gap only in the strong coupling regime, where the presence of a bound quasiparticle in the ground state ensures the even fermion parity of the excitation. Our results unravel the quantum nature of magnetic impurities on superconductors and demonstrate that pair excitations unequivocally reveal the parity of the ground state.

Graphene has many remarkable properties, it is a 2D semimetal, has relativistic-like electronic properties, and is almost free of defects. This makes very promising the study of induced superconductivity in graphene. In this thesis, we deposit Pb islands

on SiC graphene and induce superconducting by proximity effect. These islands can slide on the surface of graphene, pushed by the STM tip without being damaged critically. This manipulation tool allows the building of superconducting nanostructures that can confine superconductivity in graphene in virtually infinite geometries. We study the effect of graphene domain boundaries, twisting angles, and magnetic fields on superconducting coherence. In confined structures, the quasiparticle excitations present a spatial structure, which influences the induced Cooper pair density in graphene. For graphene grown on the two different faces of the polar crystal SiC, we observe strikingly different proximity effects. On the C-face, where graphene is at charge neutrality, the correlations only live for the coherence length, while in the Si-face graphene, n-doped, we observe an extremely homogeneous induced gap. We show that this is due to the Josephson coupling of the sparsely distributed Pb island on the surface that induces a macroscopic 2D superconducting state in graphene. The proximitized graphene superconducting substrate constitutes a novel platform to study superconductivity and magnetism at the atomic scale.

The contact between graphene and the Pb islands can be tuned by modifying the island size, which leads to the Coulomb blockade phenomenon. The interplay of Coulomb blockade and superconductivity is an intriguing phenomenon still not fully understood and interesting for engineering the parity of superconductors for quantum computing applications. In this thesis, we study the transition from conventional BCS superconducting Pb islands to small islands that manifest a Coulomb gap. These show a characteristic asymmetry of the coherence peaks that is switchable by island manipulation on the surface. We correlate the asymmetry with the presence of an excess charge on the islands. This effect can suppress completely one of the coherence peaks and can be switched by island manipulation. This joint with the manipulation can be used as a probe for the local work function of graphene.

Acknowledgments

Laura, questa tesi non sarebbe stata neanche lontanamente possibile senza di te. Averti come porto sicuro mi ha dato la possibilità di salpare verso l'ignoto e imparare rimanendo motivato. Motivazione sviluppata grazie a Riccardo, Sara e Chiara, la mia famiglia. Grazie per l'aiuto costante, le chiamate domenicali, le sciate e le camminate. Un grazie speciale a Federico, per la tua onestà e compagnia e alla tua famiglia per le conversazioni e l'accoglienza. Grazie Andrea per la lunga amicizia e per esserci sempre, a Martin per le stimolanti conversazioni e passioni condivise, a Daniele e Mattia per le cene in compagnia e a tutti gli amici di Desenzano, Diego, Francesco, Freppo, Dario, Mattia e altri... L'università mi ha cambiato, soprattutto grazie alle relazioni condivise con Laura, Simone, Daniele, Nicola, Rachele, Thomas, Enrico, Miriam, Giovanni, Matteo, Alberto e Andrea grazie per il supporto e l'amicizia. Questo viaggio che non sarebbe iniziato senza Lucio, che a Padova con pazienza e simpatia mi ha iniziato alla ricerca e che mi ha connesso con la città di Donostia.

Aquí he encontrado a Nacho, que me ha acogido cálidamente en un grupo con un ambiente muy agradable y de calidad. Estimo mucho tu fuerza para motivarnos y para ayudarnos con nuestras presentaciones y textos. Gracias por el feedback hacia un objetivo concreto, estando en primera línea tanto en la oficina como en laboratorio. Aquí aprendí muchísimo de Javier, empezando por hablar español, conducir un LT-STM, escribir en Python, bakear la máquina a las 3 de la noche. El experimento y la teoría van siempre juntos. Jon, es un honor y un placer hacer física contigo, aprecio tu simpatía y creatividad, gracias a ti he aprendido mucho de todo. Gracias a Sebas, Miguel y Carlos para colaborar en la parte de teoría. Gracias a Eva, contigo compartí un laboratorio y muchas ideas durante el COVID. Gracias a Iván y Carlos para compartir ideas y por las muchas conversaciones.

This journey was rich in wholesome conversations. Especially with Niklas. I feel that whatever the topic of our conversation, the time flies going as deep or as insane as possible. Thanks for bringing me up Igueldo, for initiating me to a great sport. Thank you Katerina for the constant support, in and out of work, for the great company, and for the great work. We shared hundreds of hours playing tennis, thanks for keeping up my motivation to play this amazing sport. Thanks to all the people in this group, in nanogune and met in Donostia for the support. In particular, the long physics discussions with Dongfei, the reparations and cycling sessions with

Leo, the surf mornings with Matteo, the game nights with Alfonso, and the trips together with Elisa L., Elisa T., Riccardo, Sara, and Gaia.

Finally, the piano has been a daily companion and source of mindful meditation. Thank you Giovanna for walking me through the first steps into music, and thank you Isabel for your endless energy. Thanks, Danilo, Jon, Irene, Pello, and Sara for the precious emotions shared playing. I learned a lot and enjoyed it more.

Contents

1 Introduction

Scanning tunneling microscopy (STM), which was developed in 1981 [1], has enabled the study of fundamental properties of matter with atomic-scale control. The technique consists in stabilizing a metallic tip on a crystalline surface with picometer precision. The exponential dependence of electron tunneling with the tip-sample distance allows for atomic-level topographic and spectroscopic imaging of materials.

One area in which STM has seen significant progress is superconductivity. By using electron tunneling spectroscopy, it became possible to measure the excitation gap Δ of a superconductor [2]. These measurements provided crucial support for the Bardeen-Shriffer-Cooper (BCS) theory, which was proposed in 1957 to explain the microscopic phenomena in superconductivity [3]. The central idea behind this theory is that the attractive interaction between electrons results in the formation of correlated electron pairs, called Cooper pairs. These pairs of electrons follow the bosonic statistics, condensing in a macroscopic state called the BCS ground state. In this ground state, all the electrons with $E < \Delta$ are paired, resulting in an energy gap for tunneling electrons.

When a magnetic impurity is deposited on a superconductor it couples to the Cooper pairs via exchange interactions. This locally modifies the excitation spectrum of the superconductor and, depending on the strength, also the ground state of the superconductor. In three seminal works Yu Shiba and Rusinov (YSR) described independently how a *classical spin* locally produces bound states for quasiparticles [4–6] visible as excitation peaks inside the superconducting gap. While their first experimental observation by STM was in 1997 [7], research on YSR states got boosted in the last decade due to many proposals for topological quantum computation based on non-abelian Majorana bound states [8, 9]. These are sought on the edges of magnetic impurity chains coupled to superconductors in the presence of spin-orbit coupling [10], fueling a great advancement in the atomic manipulation on superconductors.

Apart from this goal, these systems present very rich phenomenology often described with classical spin models. These models predict that a YSR bound state appears for each spin-polarized atomic d-orbital interacting with the superconductor [11], the wavefunction of each of these YSR interaction channels extends for distances in the order of the superconducting coherence length [12] and can mediate the coupling between YSR states in multi-impurity systems [13]. A YSR state strongly

depends on the nature of the Fermi Surface (FS), and scattering vector nesting may result in extended YSR wavefunction [12, 14, 15].

The extension of the YSR wavefunction in presence of anisotropic FS can allow the coupling of diluted structures, where no direct orbital overlap is present [16]. Moreover, 2D diluted structures of magnetic atoms in presence of spin-orbit coupling are predicted to show topological superconductivity when extended [17]. In chapter 3 of this thesis, I study the hybridization of YSR states of Mn atoms deposited on β-Bi_2Pd superconductor with a strong Fermi surface anisotropy. The 1D and 2D multi-impurity structures built with atomic precision are modeled using a Green function model, adapted in our group in collaboration with Jon Ortuzar for describing N magnetic impurities interacting with a superconductor [18]. We observe and study the weak coupling between YSR states and observe that it depends on the orientation of the 2D structures with respect to the superconductor atomic lattice.

Single atomic impurities as Mn on β-Bi_2Pd are well described by a *classical spin* approximation, where the spin is modeled as a classical vector with a fixed direction. However, the presence of spin-flip processes between spin states with different quantum numbers [19], calls for the use of a *quantum spin* description of the spin. These out-gap spin excitations have been usually considered independent from in-gap YSR states [20–22] and measured on molecules coupled to superconductors as excitations outside the superconducting gap [23]. In this thesis, I study how magnetic molecules with large magnetic anisotropy induce a rich spectrum of entangled YSR and spin-flip excitations. In collaboration with Jon Ortuzar, Sebastian Bergeret, and Miguel Cazalilla we model these excitations with a single-site quantum spin model that accounts for the interplay between magnetic anisotropy and exchange coupling [24].

BCS predicted the possibility of Cooper pair-breaking excitation at energy 2Δ can exist [3]. These pair-breaking excitations can be accessed with microwave photons and their coherent manipulation is interesting since they consist in a model q-bit system [25, 26]. However, due to parity conservation, explored in chapter 4, these excitations are forbidden for electrons. A key component to distinguish the pair excitation is the use of a proximitized superconductor, namely a gold film deposited on a vanadium superconductor.

The proximity effect refers to the transfer of a physical property between two materials when they are in contact. In this way, superconductivity is induced in a normal metal by its proximity to a superconductor. Empirically this is described as the leaking of Cooper pairs from the superconductor to the normal metal [27–29], that induces a gap in the density of states. If the proximitized material has a non-trivial band topology, topological superconductivity, and Majorana bound states can emerge [30–32]. The interaction of a magnetic impurity with a proximitized normal metal is of fundamental interest since the microscopic description of the coupling remains elusive. In chapter 4, we study the excitation spectrum of a magnetic molecule that presents YSR excitation on a proximitized Au film. This is a potential platform

for on-surface synthesis of nanographenes [33], in which localized spin moments can induce YSR states.

The proximity effect occurs also when islands of a superconductor material are deposited on a normal metal. Graphene is a semi-metallic material, one way of making it superconducting is by proximitizing it. It has been proposed that proximitized graphene can host new states of matter [34]. Induced superconductivity was studied for graphene grown on SiC0001 [35] but no further development appeared. However, an extensive theoretical effort has been done on modeling proximitized junctions and superconducting loops mainly to describe mesoscopic physics systems [36, 37]. In chapter 5 of this thesis, in collaboration with Eva Cortés-del Rio, Ivan Brihuega and Juan Carlos Cuevas we use a new method to proximitize graphene, where the Pb islands can be easily manipulated on the surface with the STM tip. This allows the construction of virtually unlimited geometries to confine and probe superconductivity in graphene. This opens many possibilities to engineer at the atomic level arbitrary superconducting nanostructures and probe how superconductivity is induced in monolayer and bilayer graphene on SiC.

The ability to manipulate Pb island on the graphene surface is due to a weak physical contact interaction between island and surface. This also affects the electrical contact between the island and the substrate. We observed by STM that with small islands on graphene, a capacitive effect gives rise to the Coulomb Blockade physics [38, 39]. While the Coulomb blockade phenomena in weakly coupled metallic grains were studied intensively in the last century [40–42], the interplay of Coulomb blockade phenomena with superconductivity remains not yet understood. In chapter 6 we study this interplay in small Pb islands, observing the presence of asymmetric quasiparticle excitation gaps that we interpret based on the presence of excess charge on the island due to local gating [43, 44].

2 Theory and experimental methods

2.1 Superconductivity

Superconductivity is a fascinating phenomenon still being studied intensively, despite being discovered more than 110 years ago by the Nobel laureate H.K. Onnes [45]. After the observation of the zero resistance drop below the critical temperature T_c, a significant contribution came by Meissner and Ochsenfeld, that discovered how superconductors expel the magnetic flux, showing perfect diamagnetism [46]. Later on, London described theoretically the Meissner effect calculating the magnetic field inside a superconductor as $B(x) \propto B_0 e^{-x/\lambda_L}$ where λ_L is the London penetration depth [47]. Later on, J. Bardeen and Pines proposed a Hamiltonian containing a phonon-mediated electron-electron attraction [48] that set the basis for the Bardeen-Cooper-Schrieffer theory.

BCS theory

Cooper took the first step by describing an instability of the Fermi surface due to an arbitrarily weak electron-electron attraction [49]. This is due to the scattering process $V_{\mathbf{k},\mathbf{k'}}$ consisting of the virtual exchange of a phonon between two electrons with opposite spin and momentum [Fig. 2.1a] and results in the formation of a Cooper pair. The interaction is attractive only for electron pairs with energy within $\hbar\omega_D$ from the Fermi surface:

$$V_{\mathbf{k},\mathbf{k'}} = \begin{cases} -V_0 & |\epsilon_{\mathbf{k}}|, |\epsilon_{\mathbf{k'}}| < \hbar\omega_D \\ 0 & \text{otherwise.} \end{cases} \tag{2.1}$$

Schrieffer advanced by proposing a ground state consisting of a coherent state of Cooper pairs operators $c^\dagger_{\mathbf{k}\uparrow} c^\dagger_{\text{-}\mathbf{k}\downarrow}$:

$$|\text{BCS}\rangle = \prod_{\mathbf{k}} (u_{\mathbf{k}} + v_{\mathbf{k}} c^\dagger_{\mathbf{k}\uparrow} c^\dagger_{\text{-}\mathbf{k}\downarrow}) \, |0\rangle \, . \tag{2.2}$$

The peculiarity of the BCS ground state is that consists of a mixture of states

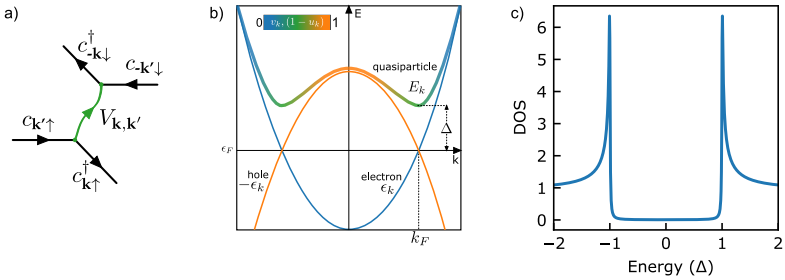

Figure 2.1: Phonon mediated coupling and superconducting gap. a) The scattering process that is responsible for the BCS pairing, is the exchange of a phonon between two electrons with opposite spin and momentum. **b)** The excitation spectrum of a BCS superconductor shows the gap with square root singularities at $\pm\Delta$.

with different particle number weighted by the coefficients defined as:

$$
\begin{aligned}
|u_{\mathbf{k}}|^2 &\equiv \frac{1}{2}\left(1+\frac{\epsilon_{\mathbf{k}}}{\sqrt{\epsilon_{\mathbf{k}}^2+|\Delta_{\mathbf{k}}|^2}}\right), \\
|v_{\mathbf{k}}|^2 &\equiv \frac{1}{2}\left(1-\frac{\epsilon_{\mathbf{k}}}{\sqrt{\epsilon_{\mathbf{k}}^2+|\Delta_{\mathbf{k}}|^2}}\right).
\end{aligned}
\tag{2.3}
$$

Finally, Bardeen Schrieffer and Cooper (BCS) solved the problem, proposing the Hamiltonian that effectively accounts for the electron-electron pairing [3]:

$$
H=\sum_{\mathbf{k},\sigma}\epsilon_{\mathbf{k}}c^\dagger_{\mathbf{k}\sigma}c_{\mathbf{k}\sigma}+\frac{1}{N}\sum_{\mathbf{k},\mathbf{k}'}V_{\mathbf{k},\mathbf{k}'}c^\dagger_{\mathbf{k}\uparrow}c^\dagger_{\text{-}\mathbf{k}\downarrow}c_{\text{-}\mathbf{k}'\downarrow}c_{\mathbf{k}'\uparrow}. \tag{2.4}
$$

The product of four fermionic operator can be simplified by mean-field approximation in this form:

$$
H^{\mathrm{MF}}=\sum_{\mathbf{k},\sigma}\epsilon_{\mathbf{k}}c^\dagger_{\mathbf{k}\sigma}c_{\mathbf{k}\sigma}+\sum_{\mathbf{k}}\Delta^*_{\mathbf{k}}c_{-\mathbf{k}\downarrow}c_{\mathbf{k}\uparrow}+\sum_{\mathbf{k}}\Delta_{\mathbf{k}}c^\dagger_{\mathbf{k}\uparrow}c^\dagger_{-\mathbf{k}\downarrow}+\text{const.}\,. \tag{2.5}
$$

This Hamiltonian gives an effective description of the physics of the low-energy pairing, where the term $\Delta^*_{\mathbf{k}}c_{\text{-}\mathbf{k}\downarrow}c_{\mathbf{k}\uparrow}$ consists in the conversion of 2 electrons into a condensate of Cooper pairs.

The mean-filed Hamiltonian in (2.5) is rewritten in a matrix form by defining a Nambu spinor basis in electron-hole space [50]:

$$H = \sum_{\mathbf{k}} (c^{\dagger}_{\mathbf{k}\uparrow}\, c_{-\mathbf{k}\downarrow}) \begin{bmatrix} \epsilon_{\mathbf{k}} & \Delta \\ \Delta^{*} & -\epsilon_{\mathbf{k}} \end{bmatrix} \begin{pmatrix} c_{\mathbf{k}\uparrow} \\ c^{\dagger}_{-\mathbf{k}\downarrow} \end{pmatrix} + \text{const.}\,. \tag{2.6}$$

This Hamiltonian is diagonalized by doing the Bogoliubov-Valatin transformation[51], from electron-hole operators ($c^{\dagger}_{\mathbf{k}\uparrow}$) to quasiparticle operators: ($\gamma^{\dagger}_{\mathbf{k}\uparrow}$):

$$\gamma^{\dagger}_{\mathbf{k}\sigma} = c^{\dagger}_{\mathbf{k}\sigma} u_{\mathbf{k}} + \text{sgn}(\sigma) c_{-\mathbf{k}\bar{\sigma}} v_{\mathbf{k}}, \tag{2.7}$$

where σ is the electronic spin, while $u_{\mathbf{k}}$ and $v_{\mathbf{k}}$ are the defined in (2.3). The Bogoliubov quasiparticle operators capture the essence of superconductivity, that is the mixture of electrons and holes. This new basis allows the recast of the Hamiltonian in a diagonal form:

$$H = \sum_{\mathbf{k}} (\gamma^{\dagger}_{\mathbf{k}\uparrow}, \gamma_{-\mathbf{k}\downarrow}) \begin{bmatrix} E_{\mathbf{k}} & 0 \\ 0 & -E_{\mathbf{k}} \end{bmatrix} \begin{pmatrix} \gamma_{\mathbf{k}\uparrow} \\ \gamma^{\dagger}_{-\mathbf{k}\downarrow} \end{pmatrix} + \text{const.}\,. \tag{2.8}$$

The ground state of this Hamiltonian is the $|\text{BCS}\rangle$ state described in eq. 2.2. This is the analog of the electron vacuum $|0\rangle$, being the vacuum for quasiparticles since its product with the quasiparticle destruction operator is $\gamma\,|\text{BCS}\rangle = 0$ (definition of vacuum), and therefore there are no quasiparticles contained. From the $|\text{BCS}\rangle$ ground state, the excitation spectrum is shown in Fig. 2.9b and consists of quasiparticle excitations with energy $E_{\mathbf{k}} = \sqrt{\epsilon^2_{\mathbf{k}} + \Delta^2}$. One of the most direct confirmations of BCS theory is the measurement of the excitation spectrum by tunneling spectroscopy [2]. Since the total number of particles is conserved, $N_s dE_{\mathbf{k}} = N_n d\epsilon_{\mathbf{k}}$, where N_s and N_n are the quasiparticle excitations density in superconducting and normal state. It follows:

$$N_s(E_{\boldsymbol{k}}) = N_n(0)\frac{d\epsilon_{\mathbf{k}}}{dE_{\mathbf{k}}} = N_n(0)\left(\frac{E_{\mathbf{k}}}{\sqrt{E^2_{\mathbf{k}} - \Delta^2}}\right)\theta(E_{\mathbf{k}} - \Delta), \tag{2.9}$$

where θ is the Heaviside function. In Fig. 2.1c we show the excitation spectrum of a superconductor, which shows a gap surrounded by the so-called coherence peaks at $\pm\Delta$. The coherence peaks represent the onset for quasiparticle excitation. Above them, the density of states shows a square-root decay asymptotically reaching $N_n(0)$, the density of states of a normal metal. The BCS density of states in eq. 2.9 goes to infinity at Δ, in a real system the peak is broadened and acquires a finite height. This is described by adding an imaginary component to the energy $E_{\boldsymbol{k}} \to E_{\boldsymbol{k}} + i\Gamma$, obtaining the Dynes formula [52, 53]:

$$N_s(E_{\boldsymbol{k}}) = N_0 \text{Re}\left[\frac{|E_{\boldsymbol{k}} + i\Gamma|}{\sqrt{(E_{\boldsymbol{k}} + i\Gamma)^2 - \Delta^2}}\right], \tag{2.10}$$

the Dynes parameter Γ is a phenomenological broadening due to a general depairing mechanism.

Single site BCS model

A very simple and instructive model is the reduction of a BCS superconductor to a single site [24, 54, 55] at the Fermi level ($\epsilon = 0$). This is formulated with the convenient choice of basis $\Psi = \{|0\rangle, c_\uparrow^\dagger c_\downarrow^\dagger |0\rangle, c_\uparrow^\dagger |0\rangle, c_\downarrow^\dagger |0\rangle\}$, which for brevity is $\Psi = \{|0\rangle, |2\rangle, |\uparrow\rangle, |\downarrow\rangle\}$. The Hamiltonian of eq. 2.6 describes only quasiparticle excitations since the ground state is more cumbersome to include due to the infinite products of eq. 2.2. This new single-site basis allows writing the Hamiltonian that also contains explicitly the BCS ground state:

$$H = \Delta c_\uparrow^\dagger c_\downarrow^\dagger + h.c. . \tag{2.11}$$

This can be cast in a 4x4 block-diagonal form:

$$H = \Psi \begin{bmatrix} H_{even} & 0 \\ 0 & H_{odd} \end{bmatrix} \Psi^\dagger, \tag{2.12}$$

where the first block H_{even} is the even parity subspace because of the even number of particles in the superconductor:

$$H_{even} = \begin{bmatrix} 0 & \Delta \\ \Delta & 0 \end{bmatrix}, \tag{2.13}$$

with two eigenvectors $|\text{BCS}\rangle = \frac{1}{\sqrt{2}}(|0\rangle + |2\rangle =$ and $|\overline{BCS}\rangle = \frac{1}{\sqrt{2}}(|0\rangle - |2\rangle)$, with eigenvalues ($-\Delta$ and Δ), and H_{odd} is the odd parity subspace $H_{odd} = 0_{2,2}$ (null matrix), with eigenvalue 0 and eigenvectors $|\uparrow\rangle$ and $|\downarrow\rangle$. Therefore there are two possible excitations from the $|\text{BCS}\rangle$ ground state, one quasiparticle excitation (Δ) that changes the parity of the system and a pair excitation (2Δ) that conserves the parity [3].

2.2 Yu-Shiba-Rusinov states induced by magnetic impurities on superconductors

Macroscopic magnetic fields destroy the coherent superconducting state at a critical value. At the nanoscale, single magnetic impurities interact with Cooper pairs modifying locally the spectrum of the superconductor. This interaction induces sub-gap excitation peaks at $E < \Delta$ called Yu-Shiba-Rusinov states that are routinely detected experimentally [7, 56–59]. The physical picture involves exchange coupling between the spin of the impurity d-electrons (**S**) and the spin of conduction electrons (**s**) [60]. This exchange interaction can be treated in a classical spin approximation or with a full quantum spin model. In the classical spin description, a preferential axis is chosen such that $\boldsymbol{S} = S_z \hat{\boldsymbol{z}}$ and the exchange coupling is considered purely longitudinal $\sim S_z s_z$. This neglects transversal exchange and breaks time-reversal symmetry

(analogous to a magnetic field). In the full quantum model, time-reversal symmetry remains unbroken and the transversal exchange is considered. This allows the description of magnetic anisotropy effects that strongly affect the excitation spectrum [24].

Classical spin Yu-Shiba-Rusinov model

Classical impurity spin models were first developed by Yu Shiba and Rusinov in their seminal work [4–6]:

$$H_{s-d} = \psi^{\dagger}(U\boldsymbol{\tau_z}\boldsymbol{\sigma_z} + J\mathbf{s}\cdot\mathbf{S})\psi, \tag{2.14}$$

where **s** is the spin operator of the conduction electrons at the impurity spin **S**, and U is a potential scattering term that reflects charge scattering and results in an asymmetry of the electron and hole wavefunctions. Adding H_{s-d} to the BCS Hamiltonian of eq. 2.6 in the classical spin approximation, pairs of Yu-Shiba-Rusinov resonances are induced inside the superconducting gap [Fig. 2.2a] at energies:

$$\varepsilon = \Delta\frac{1-\alpha^2+\beta^2}{\sqrt{(1-\alpha^2+\beta^2)^2+4\alpha^2}}, \tag{2.15}$$

where $\alpha = \pi\nu_0 JS/2$ is the dimensionless exchange coupling (ν_0 as the normal-state density of states at Fermi energy) and $\beta = \pi\nu_0 U$ the dimensionless potential scattering. Phenomenologically, the classical magnetic impurity tends to align the electrons of the Cooper pairs, lowering the "binding energy" Δ, and thus, creating bound states inside the gap. These states can be excited resulting in quasiparticle excitations, analogous to excitations of bare superconductors. At low exchange coupling the impurity spin is in the weak coupling regime. When the exchange J is increased up to a critical

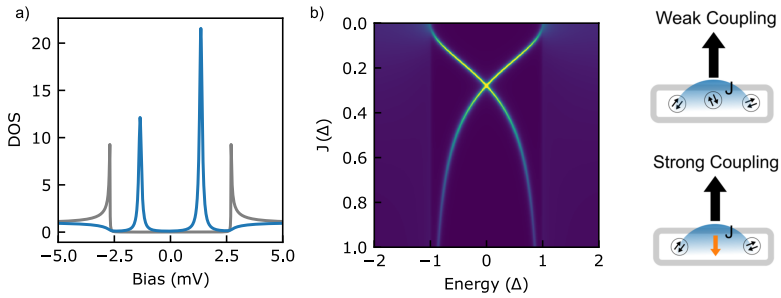

Figure 2.2: Classical spin YSR spectrum and quantum phase transition. a) The spectrum of a magnetic impurity shows in gap states, with a non-zero potential scattering U a particle-hole asymmetry is induced. **b)** As the exchange J is increased a level crossing occurs inducing a quantum phase transition. On the right: in the weak coupling regime the spin is free and in the strong coupling regime, the impurity spin binds a quasiparticle forming a singlet.

value the YSR excitation peak crosses zero energy inducing a *quantum phase transition* [Fig. 2.2b] to the strong coupling regime, where a quasiparticle binds to the impurity forming a singlet state [60].

The YSR excitation has a spatial shape that is obtained by solving the problem with the Green Function approach. Given a general Hamiltonian, the Green function (or propagator) is defined as [37]:

$$[\epsilon - \mathbf{H}(\boldsymbol{r})]G(r, r', \epsilon) = \delta(\boldsymbol{r} - \boldsymbol{r}'). \tag{2.16}$$

The Green function $G(r, r', \epsilon)$ is a complex-valued function that depends on the spatial coordinates and the energy. This function is directly connected to the density of states:

$$\rho(\boldsymbol{r}, \epsilon) = \pm\frac{1}{\pi}\mathrm{Tr}\{\mathrm{Im}[G^{a,r}(r, r', \epsilon)]\}. \tag{2.17}$$

The function $\rho(\boldsymbol{r}, \epsilon)$ is peaked at the poles of the Green function (YSR peaks in [Fig. 2.2a]), which are the eigenvalues of the Hamiltonian (eq. 2.16). The *retarded* and *advanced* Green Functions ($G^{a,r}(r, r', \epsilon)$) are defined by adding an infinitesimal imaginary part to the energy $\epsilon \rightarrow \epsilon \pm i\eta$. This has the practical application of giving a non-zero line width (η) to the peaks in the spectrum, which accounts for a finite lifetime and energy resolution.

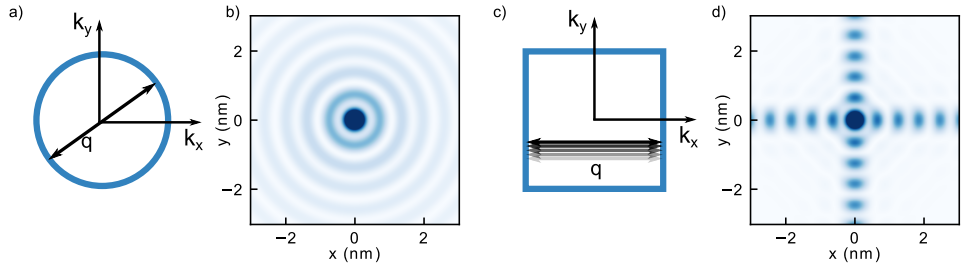

Figure 2.3: Impurity scattering and Fermi surface anisotropy. a) Constant energy contour in the k-space showing a back-scattering process q. **b)** Real-space modulation resultant from the scattering process in a), reproduced from [18]. **c)** Constant energy contour in k-space of a metal with anisotropic Fermi surface. The scattering vectors with q-direction perpendicular to the parallel energy branches are called nested vectors. **d)** Real-space modulation with focusing resultant from the nested scattering vectors in c), reproduced from [18].

With this approach, the spatial distribution of $\rho(\boldsymbol{r}, \epsilon)$ is calculated for the electron and hole component of the YSR state [60]. For an isotropic superconductor, an analytical solution can be easily obtained which yields:

$$\rho(\boldsymbol{r}, h/e) \sim \frac{sin(k_F r - \delta_0^{+/-})}{(k_F r)^{(1-d)/2}} e^{-r/\xi|\sin(\delta_0^+ - \delta_0^-)|}, \tag{2.18}$$

this is an oscillating wavefunction that decays away from the impurity with the coherence length (ξ) and the dividing factor depends on the dimensionality of the system d=1,2,3 [12]. The spatial distribution of the YSR state depends on the shape of the Fermi surface. For a 2D superconductor with a circular Fermi contour [Fig. 2.3a] the radial oscillations of Fig. 2.3b are observed in real space. For anisotropic Fermi contours, the scattering vector nesting occurs between parallel sectors of the Fermi surface [Fig. 2.3c] inducing focusing of the extensions along preferred directions [Fig. 2.3d] [14, 18] that makes inter-impurity coupling strongly anisotropic.

Quantum treatment of spin, beyond the Yu-Shiba-Rusinov model

While the classical YSR models are quite successful [13, 60–62], they cannot capture the correct degeneracies of the ground and excited states and usually preclude the consideration of anisotropy effects. The superconducting single-site model, introduced previously (eq. 2.11), was extended by von Oppen in [24] to describe the YSR states of a quantum spin in presence of magnetic anisotropy. For an S = 1/2 coupled to a superconductor, one uses the single site superconductor basis $\psi_{S=1/2} = [(|0\rangle\,|2\rangle\,|\uparrow\rangle\,|\downarrow\rangle) \otimes |\pm 1/2\rangle]$, i.e. the vector product of BCS states and impurity spin states, obtaining the following Hamiltonian:

$$H = \Delta_s c_\uparrow^\dagger c_\downarrow^\dagger + \text{h.c.} + \sum_{\sigma\sigma'} c_\sigma^\dagger \left[V\delta_{\sigma\sigma'} + J_z \hat{S}_z s^z_{\sigma,\sigma'} + J_\perp \left(\hat{S}_+ s^-_{\sigma\sigma'} + \hat{S}_- s^+_{\sigma\sigma'} \right) \right] c_{\sigma'}, \quad (2.19)$$

where J_z and $J_\perp$ are the axial and transverse magnetic exchange couplings, and V is the impurity scattering potential, which we set to 0 for now. This Hamiltonian can be recast in an 8x8 block diagonal matrix as eq. 2.12, where:

$$H_{even} = \begin{bmatrix} 0 & 0 & \Delta & 0 \\ 0 & 0 & 0 & \Delta \\ \Delta & 0 & 0 & 0 \\ 0 & \Delta & 0 & 0 \end{bmatrix} H_{odd} = \begin{bmatrix} J_z/4 & 0 & 0 & 0 \\ 0 & -J_z/4 & J_\perp & 0 \\ 0 & J_\perp & -J_z/4 & 0 \\ 0 & 0 & 0 & J_z/4 \end{bmatrix}. \quad (2.20)$$

The even parity subspace has eigenvectors $|\pm 1/2\rangle\,|\text{BCS}\rangle$ and $|\pm 1/2\rangle\,|\overline{BCS}\rangle$ with eigenenergies ($-\Delta$ and Δ), while the odd parity subspace has one in-gap eigenvector (YSR state):

$$|\text{odd}\rangle = \frac{1}{\sqrt{2}}(|1/2\rangle\,|\downarrow\rangle - |-1/2\rangle\,|\uparrow\rangle), \quad (2.21)$$

with eigenvalue $(-J/4 - J_\perp)$. While the even states merge with the continuum in a real superconductor, the $|\text{odd}\rangle$ state (eq. 2.21), i.e. the YSR resonance, is an entangled state of a quasiparticle and the impurity spin in the weak coupling regime. The energy of the in-gap YSR lowers for increasing J and when it reaches $-\Delta$ there is a quantum phase transition like in the classical approximation. The new ground state $|\text{odd}\rangle$ has S=0 since the spin of the impurity is screened by the quasiparticle.

In chapter 4 we use the Hamiltonian of eq. 2.20 generalized for an S=5/2 system with magnetic anisotropy to describe a molecular spin coupled to a proximitized superconductor. In this study, we will show how the single-site model describes well the YSR physics also in the case of a proximitized superconductor, the subject of the following section.

2.3 Superconducting proximity effect

The proximity effect is a phenomenon that occurs when a normal metal N is contacted with a superconductor S and Cooper pairs leak from S to N [63]. In S there are no fermionic states at energies below the gap, therefore to connect the electrons reservoir of N with the Cooper pairs reservoir of S, a process called Andreev reflection occurs at the interface [27]. This process was described in detail by Blonder et al. [28] who solved the Bogoliubov de Gennes (BDG) equation at the interface. To describe a realistic system one must face the possible disorder that causes scattering and inhomogeneities in the order parameter. The complexity is reduced in the quasi-classical theory that consists in the calculation of the impurity-averaged Green function resulting in the Usadel equations that reduce the complexity of a full BDG treatment [64]. In the limit of a perfectly clean ballistic SN, one can directly solve the BDG equation setting the boundary conditions that respect the geometry of the system.

Andreev reflection

Starting from the mean-field Hamiltonian of eq. 2.5 and writing $c_{-\mathbf{k}\downarrow} = h^{\dagger}_{\mathbf{k}\uparrow}$ as a hole operator, one can rewrite the same term as $h^{\dagger}_{\mathbf{k}\uparrow}\Delta^{*}c_{\mathbf{k}\uparrow}$, this is a scattering process called Andreev reflection where an electron is converted into a condensed pair and a hole [51]:

$$\text{Andreev reflection}: e^{-} \rightleftharpoons \text{pair}^{2-} + h^{+}, \tag{2.22}$$

where the reflected hole has the same momentum of the incoming electron, but opposite group velocity, leading to a non-specular reflection [Fig. 2.4]. The mixing of electron and hole degrees of freedom opens the gap Δ in the quasiparticle excitation

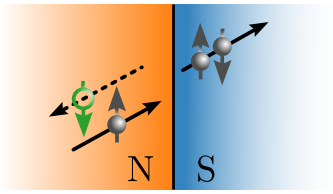

Figure 2.4: Andreev reflection. One incident electron from the normal metal N is reflected into a hole and a Cooper pair is transferred in the superconductor S.

spectrum. The quasiparticle excitation of eq. 2.1 is described in the BDG formalism by a two-column vector [28]:

$$\psi = \begin{bmatrix} f(x) \\ g(x) \end{bmatrix}, \tag{2.23}$$

where the functions $f(x)$ and $g(x)$ they are proportional to u_k and v_k and satisfy the differential equations:

$$\begin{aligned} i\hbar\frac{\partial f(x)}{\partial t} &= Hf(x) + \Delta g(x), \\ i\hbar\frac{\partial g(x)}{\partial t} &= -Hg(x) + \Delta f(x). \end{aligned} \tag{2.24}$$

two coupled equations for electron and hole quasiparticle components.

The wavefunctions of the particles incident, reflected, and transmitted for $E > \Delta$ are:

$$\psi_{inc} = \begin{bmatrix} 1 \\ 0 \end{bmatrix} e^{iq^+x}, \quad \psi_{ref} = \frac{v_0}{u_0}\begin{bmatrix} 0 \\ 1 \end{bmatrix} e^{iq^-x}, \quad \psi_{trans} = \frac{1}{v_0}\begin{bmatrix} u_0 \\ v_0 \end{bmatrix} e^{ik^+x}, \tag{2.25}$$

where u_0 and v_0 are the k-dependent particle-hole weights. At the steady state, there is an incident electron and a time-reversed hole in N and a quasiparticle propagating in S. At $E < \Delta$ the incident electron is totally reflected as a hole ($k^+ = k_F + i\frac{\sqrt{\Delta^2 - E^2}}{\hbar v_F}$), the resultant quasiparticle current is exponentially suppressed in S:

$$J_q = 2ev_F \exp\left(\frac{-2\sqrt{\Delta^2 - E^2}x}{\hbar v_F}\right). \tag{2.26}$$

This disappearing quasiparticle current is converted into a reappearing supercurrent when entering the superconductor:

$$J_S = 2ev_F\left(1 - \exp\left(\frac{-2\sqrt{\Delta^2 - E^2}x}{\hbar v_F}\right)\right). \tag{2.27}$$

Thus the incident electrons are effectively converted into Cooper pairs that propagate in S. In N, the time-reversed electron-hole pair also carry a charge 2e, resembling a super-current.

Diffusive limit of the proximity effect

In the 1960s, a qualitative description of the proximity effect emerged [63]. The superconducting correlations in a normal metal are quantified by the amplitude of condensation $F(r) =< \psi_\uparrow(r)\psi_\downarrow(r) >$ which is the probability of finding a Cooper pair at r. In a superconductor, the pair potential is $\Delta(r) = V(r)F(r)$, where $V(r)$ is the pairing interaction (electron-phonon coupling). The function $\Delta(r)$ reduces to the order parameter inside the superconductor and vanishes in the normal metal,

although $F(r)$ does not [64]. So in the normal metal, there is no order parameter, but the condensation amplitude can be non-zero.

This was rationalized later by Andreev and Klapwijk [27, 29] who use Andreev reflection to interpret this condensation in the normal metal as the formation of correlated electron-hole pairs that travel in the normal metal for a distance called *coherence length* (ξ). A pair dephases by a factor of $-2iEt/\hbar$ after entering the normal metal. For a dephasing of order 1, $t \approx \hbar/E$, so a pair travels a distance of the order $d_E = \sqrt{D_N t} = \sqrt{\hbar D_N/E}$ with D_N the diffusion constant of the normal metal. Therefore d_E is the coherence length of the electron-hole pairs in the metal. If we consider now an SNS geometry, if the length L of the normal metal region is $d < d_E$, correlated pairs flow between the two superconducting leads of SNS (Josephson current) [65]. This is equivalent to saying that electrons with $E < E_{\text{Th}} = \hbar D/d^2$, where E_{Th} is the Touless Energy, are still correlated when reaching the opposite lead.

For a dirty superconductor, the electronic mean free path (l) can be lower than ξ. Usadel realized that in this dirty limit, the Green function is almost isotropic in space and he further simplified the Gorkov equation in a diffusion-like form [66]:

$$\frac{\hbar D}{\pi}\nabla(G\nabla G) + \mathbf{H} = 0. \tag{2.28}$$

where G is the retarded Green function that depends on energy and position. Setting the boundary conditions, the DOS is determined with eq. 2.17. This treatment is very powerful and allows us to describe the modification of the DOS depending on the system geometry.

The most significant examples are SN and SNS structures. In Fig. 2.5a we reproduce a calculation from [64] for an SN junction with a normal part of length $d = 4\xi$ the local DOS in the function of energy shows a constant minigap along the N part with the DOS evolving continuously from standard BCS DOS to a smooth DOS

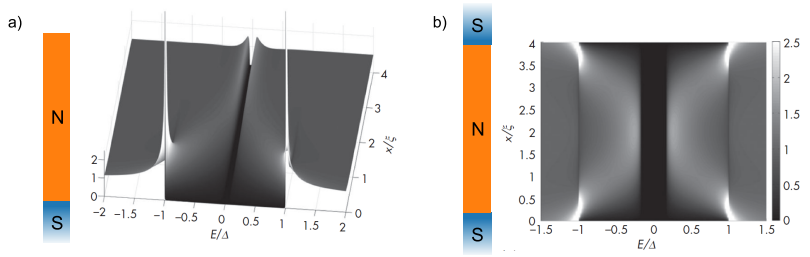

Figure 2.5: Diffusive SN and SNS junctions DOS. a) Diffusive Usadel equations for SN junction with a normal part of $d = 4\xi$, reproduced from [64]. **b)** Simulation of an SNS junction with a normal part of $d = 4\xi$. In both a and b, there is a constant minigap, and the coherence peaks decay getting far from S, reproduced from [64]

with no peaks in N. The constant minigap is determined by the Thouless energy $\Delta_g = 0.765E_{\mathrm{Th}}$, which depends on the ratio of ξ and L since $E_{\mathrm{Th}} = \Delta(\xi/d)^2$, where Δ is the bulk gap of S. In an SNS junction, the DOS is symmetric with the appearance of a minigap constant through the structure. In Fig. 2.5b we reproduce from [64] the calculation for a junction of $d = 4\xi$. The BCS singularity goes from being peaked close to S to a faint dip in the middle of the junction.

So far we have considered the ideal situation where the SN interfaces are perfectly transparent and the two superconducting leads have the same macroscopic phase. A phase difference also closes the minigap reaching the normal state at $\phi = \pi$ [Fig. 2.6a]. A similar behavior occurs with the interface opacity, r>0 closes the minigap that scales as $1/r$ [Fig. 2.6b].

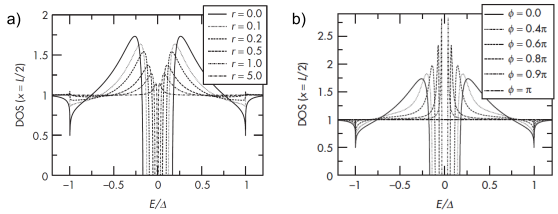

Figure 2.6: Interface reflection coefficient and phase dependence of SNS junction. a) DOS in the middle of a diffusive SNS junction, changing the phase of the two superconducting leads to the minigap closes, reproduced from [64] **b)** DOS in the middle of a diffusive SNS junction, changing the reflection coefficient of the SN interfaces, reproduced from [64]

Ballistic limit of the proximity effect

We described the proximity effect in the dirty limit where the diffusive model simplifies the problem. For clean systems, the mean free path is much longer than the coherence length and the full Bogoliubov equations (eq. 2.24) have to be solved with proper boundary conditions.

Phenomenologically, the confinement of Bogoliubov quasiparticle in the normal metal induces the presence of bound states at an energy below the bulk gap of the leads. These are the so-called Andreev bound states. While in SNS geometries only Andreev reflections are involved, in SN geometries an additional normal reflection occurs at the N-vacuum interface. The proximity gap is defined by the energy separation E_0 of the two lowest Andreev bound states. The mean time τ_{dwell} between Andreev reflections sets the Thouless Energy $E_0 = E_{gap} = \hbar/\tau_{dwell}$. Like in the diffusive case, the minigap is smaller than the bulk gap by a factor $\xi/v_F\tau_{dwell}$ [67], where $\xi = \hbar v_F/\Delta$.

The approach was first developed by McMillan [69] and adapted to SN and SNS junctions by Arnold [68] and Kulik [70]. The SN system is depicted in Fig. 2.7a, with

the superconductor at x>0 and a normal metal at $-d < x < 0$. We are interested in the DOS of the system that is calculated from the Green function. From the Bogoliubov equations (eq. 2.24) and the Gorkov equation (eq. 2.16) one can calculate the Green function applying the boundary conditions at the SN interface:

$$\left.\frac{dG_{N,S}(x,x')}{dx}\right|_{x=0} = 0 = \left.\frac{dG_{N,S}(x,x')}{dx}\right|_{x'=0}, \tag{2.29}$$

where $G_{N,S}$ is the Green function in N or S and at x=0 is the NS interface. At free surfaces, the Green's function must vanish. We give directly the simplified form of the Green function calculated in [68] expressed here in atomic units ($\hbar = 1$):

$$G_{S,N} = \frac{m}{k_F}\frac{iF(E)\cos\left(K_+x + K_-d\right) - \sin\left(K_+x + K_-d\right)}{iF(E)\sin\left[(K_+ - K_-)d\right] - \cos\left[(K_+ - K_-)d\right]}, \tag{2.30}$$

where

$$\begin{aligned} F(E) &= \frac{E}{\sqrt{E^2 - \Delta^2}}, \\ K_+ &= \sqrt{k_F^2 + 2mE}, \\ K_- &= \sqrt{k_F^2 - 2mE}. \end{aligned} \tag{2.31}$$

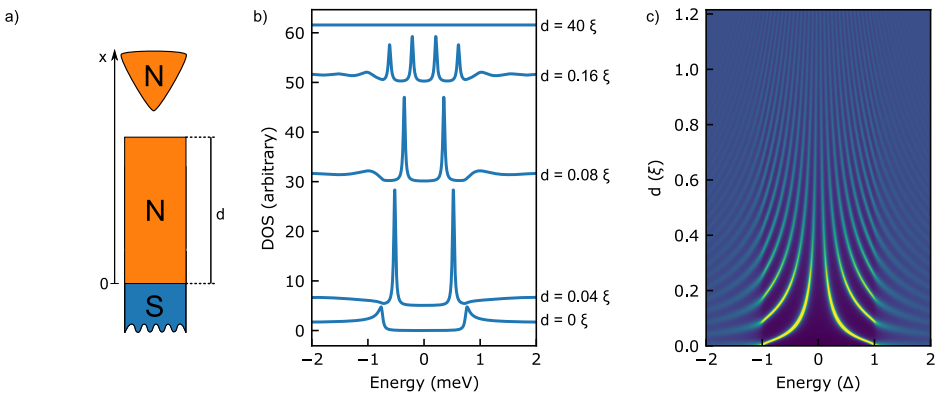

Figure 2.7: Ballistic SN junction DOS. a) SN geometry adopted by Arnold [68], we take the limit of large S and large tunnel probe c. **b)** The plot of the ballistic SN junction DOS using eq. 2.30 for different thickness values d = (0,0.4,0.8,0.16,40)·ξ of N. c) Thickness-dependent evolution of the SN DOS, increasing number of Andreev bound states appear in the superconducting gap with the normal metal thickness with out-gap oscillations.

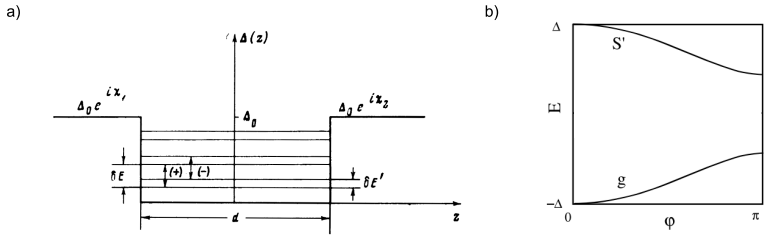

Figure 2.8: Ballistic SNS junction level scheme. a) Energy level diagram for the ballistic SNS junction model [70].**b)** Phase dependence of the Andreev bound states energy [71].

From $G_{S,N}$ one can calculate the DOS with eq. 2.17 and plot it in the function of the thickness of the normal layer in Figs. 2.7b-c. We can see the formation of multiple in-gap states increasing d In the limits of large d, we have a flat, metallic density of states and in the limit of small d, the DOS reduces to the standard BCS gap equation.

Kulik in [70] calculated the same quantities in the SNS junction case. Where the phase of the two superconductors is an additional parameter Also in this case, a set of doubly degenerate bound states is obtained with energies:

$$E_n^{\pm} = (v/2d)[2\pi(n + 1/2) \mp \chi] \ (n = 0, 1, 2, ...). \tag{2.32}$$

Fig. 2.8a, adapted from [70] sketches the energy levels as bound states with constant energy along the junction, split by the phase difference (χ). The energy of the levels is constant across the junction and depends on the phase difference between the leads. In Fig. 2.8b, we see how Andreev bound states shift towards zero energy as the phase is increased, and a change in phase of 2π returns to the initial state.

In chapter 4 we study thin films of Au deposited on vanadium superconductor and we observe sub-gap peaks whose energy position depends on the thickness of Au, which we associate to Andreev bound states formed in the SN junction. In chapter 5 we study induced superconductivity in graphene where we build SNS structures where we have evidence of both diffusive and ballistic proximity effects.

2.4 Coulomb blockade phenomena in ultra-small tunnel junctions

In chapter 6 we observe how superconductivity is affected by reducing the size of Pb nanoislands deposited on graphene. This is well described by the Coulomb blockade that arises due to the weak coupling of the island with the substrate.

The coulomb blockade effect in tunneling experiments results in the suppression of the tunneling conductance due to the reduction of the density of states at zero energy by e-e interaction [72]. This can have two possible origins, the first consists

in the existence of finite charging energy in ultra-small junctions with small capacitances, where the energy $E_C = e^2/2C$ is needed to add an extra electron. The second phenomenon is called dynamical Coulomb blockade (DBC) and is caused by the redistribution of charges in junctions induced by electron tunneling where the time scale of propagation becomes important. These two effects were unified and described within the same framework by Rollbühler et al. in the so-called P(E) theory [72]. The function P(E) describes the probability for an electron to emit energy E into the electromagnetic environment.

Coulomb blockade phenomena also arise for double barrier tunnel junctions (DBTJ) systems, for example, when tunneling to nanosized grains that present very small tunneling capacitance to the substrate underneath. This is described by the "orthodox" theory of correlated electron tunneling [73], which was described and proved experimentally by Hanna and Tinkham [41]. These two frameworks describe two types of phenomenology, the Coulomb blockade gap (or Coulomb gap) that appears for both single and double tunneling junctions, and the Coulomb staircase, a series of steps in the tunneling current that appear only in the double junction regime [41]. We briefly introduce in the following sections the DBC (single junction) and DBTJ (double junction) models.

Dynamical Coulomb blockade model

We describe here the steps for calculating the Coulomb blockade gap in the DBC framework from [38, 74], the first step is to calculate the P(E) function given by [75]:

$$P(E) = \frac{1}{2\pi\hbar}\int_{-\infty}^{\infty} dt \exp\left[J(t) + iEt/\hbar\right] \tag{2.33}$$

This expression is the Fourier transform of the equilibrium correlation function of the phase across the junction and can be expressed in terms of the impedance $Z(\omega)$ of the total system, following [75]:

$$J(t) = \frac{2e^2}{h}\int_0^{\infty} \frac{d\omega}{\omega} Z(\omega)\left\{ \coth\left(\frac{\hbar\omega}{2k_BT}\right)\left[\cos(\omega t) - 1\right] - i\sin(\omega t)\right\}. \tag{2.34}$$

For the circuit in the inset of Fig. 2.9a the tip-island-substrate total impedance reads $Z(\omega) = [i\omega C_T + Z_{ex}^{-1}]^{-1}$ where C_T is the tip-island capacitance and $Z_{ex}(\omega) = 1/(i\omega C + 1/R)$ is the impedance related to the island-substrate contact. This results in a total impedance of $Z(\omega) = [i\omega(C + C_T) + 1/R]^{-1}$. Since the tunneling resistance $R_T = 1M\Omega - 1G\Omega$ is generally much larger than the quantum of resistance ($\sim 12.9k\Omega$) we follow a treatment where the tunnel junction coupling is treated as a small perturbation [38].

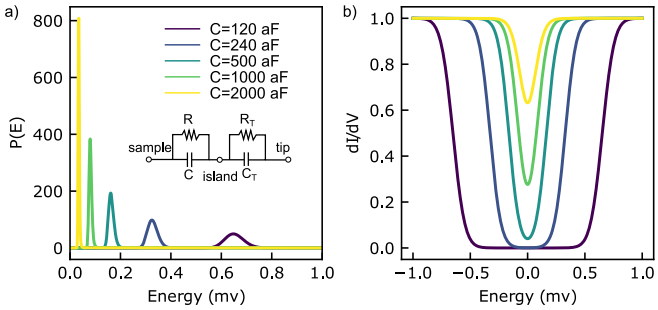

Figure 2.9: Dynamical Coulomb blockade. a) P(E) function of eq. 2.33 computed for various values of island-surface capacitance. **b)** Resultant dynamical Coulomb blockade gap using the P(E) shown in a) calculated in collaboration with Jon Ortuzar.

The tunneling current is given by $I(V) = e[\Gamma_{\text{isl}\to\text{tip}}(V) - \Gamma_{\text{isl}\leftarrow\text{tip}}(V)]$, with:

$$\Gamma_{\text{isl}\to\text{tip}}(V) = \frac{1}{h}\int_{-\infty}^{\infty} dE \int_{-\infty}^{\infty} d\epsilon f(E)[1 - f(E - \epsilon + eV)]P(\epsilon), \tag{2.35}$$

and the tip and substrate were considered with a constant density of states. We show in Fig. 2.9a the P(E) function for different values of capacitance, and the Coulomb gap in Fig. 2.9b. Lowering C the onset of the Coulomb blockade gap shifts at higher energies, while increasing R just increases a broadening of the gap edge. The gap is well visible when $E_c = e/2C < k_BT$, while it is smeared for higher temperatures. For a very high capacitance P(E) resembles a Dirac-delta and the effect on the DOS is negligible and only visible at very low temperatures [76].

Double tunnel junction model

The orthodox model describes the I(V) characteristic of double tunnel junction (DBTJ) systems, where the Coulomb blockade and Coulomb staircase interplay with the excess charge leading to a rich diagram of charged states. We follow the treatment of Hanna and Tinkham that consider the DBTJ model in the didactic limit of $R_T >> R$, where the expressions are analytic [41]. The system is depicted in Fig. 2.10a, a center electrode (island) is connected to two side electrodes (tip and sample) by two tunnel junctions (j=1,2). The electron tunneling rate for the two junctions is:

$$\Gamma_j^{\pm}(n) = \frac{1}{R_j e^2}\left(\frac{-\Delta E_j^{\pm}}{1 - \exp(\Delta E_j^{\pm}/k_BT)}\right). \tag{2.36}$$

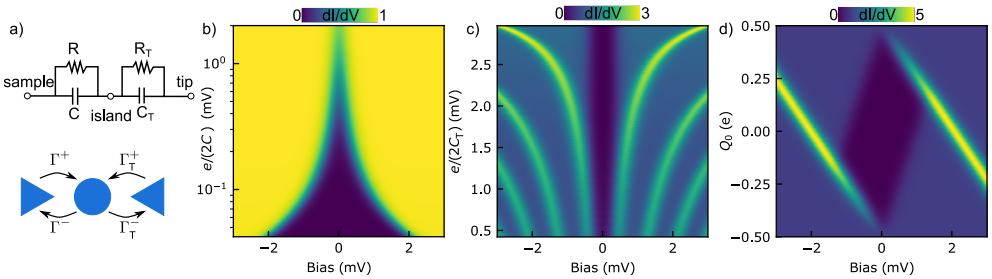

Figure 2.10: dI/dV of a double tunnel junction. a) Scheme of a DBTJ and the tunneling rates in the tip-island-substrate system. **b)** Coulomb blockade gap dependence on the island-substrate capacitance in the $R_T >> R$ limit with $C_T << C$. **c)** Appearance of Coulomb staircase (charging peaks in dI/dV) increasing C_T (C = 200 aF, $e/2C$ = 0.4 mV). **d)** Coulomb blockade gap dependence on the Excess charge, generating a Coulomb diamond.

The ΔE_1 is the energy change of the system subsequent to a tunneling event:

$$\begin{aligned}\Delta E_1^{\pm} &= \frac{e}{C_\Sigma}\left(\frac{e}{2} \pm (ne - Q_0) \pm C_T V\right),\\ \Delta E_2^{\pm} &= \frac{e}{C_\Sigma}\left(\frac{e}{2} \pm (ne - Q_0) \mp C V\right),\end{aligned} \tag{2.37}$$

where $C_\Sigma = C + C_T$ and Q_0 is the excess charge on the central island, usually associated with a difference in work functions of tip and sample.

The general net current is given by the expression:

$$I(V) = e\sum_{n=-\infty}^{\infty} \sigma(n)[\Gamma_{\text{isl}\to\text{tip}}(n) - \Gamma_{\text{isl}\leftarrow\text{tip}}(n)] \tag{2.38}$$

where σ_n is the probability of having n electrons on the center electrode. This infinite sum simplifies greatly in the $R_T >> R$ limit where n_0, the most probable number of electrons in the center electrode, is determined only by junction 1 (since $\Gamma >> \Gamma_T$ and therefore depends only on C_T [41]:

$$e^{-1}(-C_T V + Q_0 - e/2) \leq n_0 \leq e^{-1}(-C_T V + Q_0 + e/2) \tag{2.39}$$

The resultant current I(V) is 0 in the so-called Coulomb blockade when:

$$(-e/2 + n_0 e - Q_0)/C \leq V \leq (e/2 + n_0 - Q_0)/C \tag{2.40}$$

Outside the Coulomb gap, the current is:

$$I(V) = \frac{1}{R_T(C_\Sigma)}\left(-(n_0 e - Q_0) + CV - \frac{e}{2}\text{sgn}(V)\right) \tag{2.41}$$

where n_0 is obtained from eq. 2.39. The coulomb gap opens with decreasing C as shown in Fig. 2.10b where we plot the calculated dI/dV with a thermal broadening. The Coulomb staircase manifests as charging peaks outside the Coulomb gap [Fig. 2.10c] that with increasing C_T move at higher energy. Finally, we show in Fig. 2.10d how excess charge Q_0 shifts the Coulomb gap and the charging peaks resulting in the well-known Coulomb diamond plots where the Coulomb gap closes at $Q_0 = \pm e/2$.

2.5 Scanning tunneling microscopy and spectroscopy

Scanning tunneling microscopy (STM) is an established scanning probe technique that allows the topographic and spectroscopic mapping of the surface of solids at the nanoscale, giving access to single atoms and molecules and their electronic properties. STM was invented in 1982 by G. Binnig and H. Rohrer, who were awarded the Nobel Prize in physics in 1986. From these early days, the technology developed consistently, especially in cryogenic solutions to cool down the setup at temperatures as low as 10mK [77]. The low T, the isolation from mechanical vibrations, and the ultra-high vacuum allow the scanning of a sharp metallic tip by piezoelectric actuators with pm precision while measuring the tunneling current.

One electron with energy E can penetrate a barrier $\phi > E$. In the barrier, the electron wavefunction decays exponentially [78]:

$$I_t \propto V\rho_s(E_F)e^{-1.025z\sqrt{\phi}} \tag{2.42}$$

where V is the bias voltage between tip and sample, ρ_s is the density of states of the sample and 2 is the tip-sample distance. With a typical barrier of $\phi = 5eV$ (gold work function), the tunneling current decays one order of magnitude when z is changed by 1Å.

In eq. 2.42 the current is directly proportional to Vρ_s and a constant dependent on the tip-sample height. The most powerful feature of an STM is scanning tunneling spectroscopy (STS), where V is swept at constant z. The general form for the bias-dependent current flowing between tip and sample is:

$$I_t(V) = \frac{4\pi e}{\hbar}\int_{-\infty}^{\infty}\rho_s(\varepsilon - eV)\rho_t(\varepsilon)|T^2|[f(\varepsilon - eV) - f(\varepsilon)]d\varepsilon, \tag{2.43}$$

where we set $E_F = 0$. This mathematically is a convolution between the density of states weighted by the Fermi Dirac distributions $f(E)$ and the tunneling matrix element M. Then the differential conductance dI/dV is equal to ρ_s. This is true in the approximation of a constant ρ_t and at low voltages.

Tunneling between two Superconductors

In this thesis, the quantities ρ_t and ρ_s of eq. 2.43 are frequently BCS density of states (DOS). In Fig. 2.11a we show the BCS DOS seen with a normal tip (not superconducting, with a constant DOS). The coherence peaks are broadened by the metallic

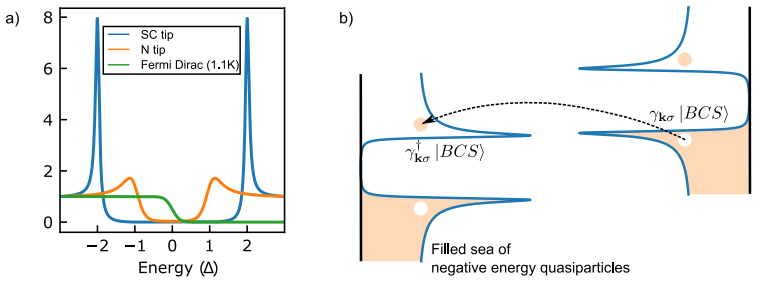

Figure 2.11: Tunneling between two superconductors. a) DOS of a superconductor at T=1.1K measuring with a metallic and superconducting tip, showing the increased energy resolution. Note that the Fermi Dirac distribution is flat at the coherence peak. **b)** Semiconductor analogy for the tunneling between two superconductors, that occurs when aligning empty with filled states. The same description applies to YSR states.

tip Fermi-Dirac distribution. With a superconducting tip, the coherence peaks appear at 2Δ or $\Delta_t + \Delta_s$ if sample and tip have different gaps. The Fermi Dirac distribution can be approximated to a step-function if the tip and sample superconducting gaps are larger than k_BT, and therefore the coherence peaks appear as very sharp resonances. The conductance outside the superconducting gap is usually constant at the *normal state conductance* (G_N). In this Thesis, we will frequently normalize the dI/dV expressing it in units of G_N. This is useful to compare spectra taken at different current setpoint values.

Microscopically, the tunneling between two superconductors can be rationalized with a semiconductor analogy. This is done by rewriting eq. 2.5 [51] dividing the Brillouin zone into two halves and using the fermionic commutation relations:

$$H = \sum_{k \in \frac{1}{2}BZ, \sigma} E_{\mathbf{k}}(\gamma^{\dagger}_{\boldsymbol{k}\sigma}\gamma_{\boldsymbol{k}\sigma} - \gamma_{-\boldsymbol{k}\sigma}\gamma^{\dagger}_{-\boldsymbol{k}\sigma}) \tag{2.44}$$

in this picture, the BCS ground state can be regarded as a filled sea of negative energy quasiparticles (first term) and an empty sea of positive energy quasiparticles (second term). At T=0 the tunneling between two such a semiconductor is possible only when aligning holes and electrons bands [Fig. 2.11b], therefore applying a bias voltage of $V = \pm 2\Delta/e$. This picture works in the same way with in-gap YSR states, where the YSR component below Fermi energy is filled and the one above is unoccupied. Thermal tunneling can occur when $k_BT \approx \Delta$ or in the presence of in-gap features when $k_BT \approx \varepsilon$, where ε is the in-gap feature position with respect to zero energy [79]. This is rationalized in the semiconductor analogy with partial filling of the electron/hole bands with holes/electrons.

Dynes deconvolution

The density of states measured by STS is the convolution of tip and sample DOS. The numerical operation to retrieve the sample DOS knowing the tip DOS is called deconvolution. The convolution is a linear operation that, with a discretized data set, is effectively a matrix multiplication [80]:

$$\left[\frac{dI}{dV}\right] = M_g \cdot [\rho_s] \tag{2.45}$$

where M_g is a function (matrix form) that contains the Fermi-Dirac distribution and ρ_t. While the Fermi-Dirac is known, here we consider a conventional BCS tip gap described by the Dynes function of eq. 2.1. The deconvolution process then reduces to the inversion of the M_g matrix. As this is a non-rectangular matrix the Moore-Penrose pseudoinverse M_g^+ is used instead, which is based on least squares fit. The sample density of states is therefore obtained as:

$$[\rho_s] \sim M_g^+ \left[\frac{dI}{dV}\right]. \tag{2.46}$$

Edge effects can be seen when the range of measurement is limited. In the case of a superconductor spectrum, the DOS outside the gap is constant, therefore additional points with normal conductance can be added to solve the problem [80]. When both DOS are BCS-like the temperature parameter has a negligible effect since the Fermi-Dirac can be approximated to a step function. The Dynes parameter is chosen in order to provide an artifact-free density of states and usually in the order of $\Delta/20$. The outcome of the deconvolution is also very sensitive to the data sampling and spectral background noise, a problem solved by colleague Jon Ortuzar that implemented an interpolation procedure and Savizky-Golay filtering of the data prior to deconvolution.

STM operation modes

In this section, we will briefly describe the measurement modes used to measure the data that will be presented.

Topography

During a constant current scan, the tunneling current is maintained constant following the topographical features by controlling the tip z position via piezoelectric actuators with a feedback loop. The feedback loop can be also deactivated in scanning conditions, and the topography information is then contained in the tunneling current. This is called constant height mode and is often used to map the atomic lattice resolution of the substrates.

Bias spectroscopy

The spectroscopy is recorded by sweeping the sample-tip bias voltage while the tip is held at a fixed distance with respect to the sample. We use two methods for measuring dI/dV, the first, to do fast checks, consists in numerically differentiating the I(V) curve. The second, to take fine measurements, involve the use of an AC voltage modulation at 1kHz generated by a lock-in amplifier. This, with phase-sensitive detection, collects the response from the current signal, that has the same frequency giving the local dI/dV. The modulation amplitude must be chosen to be lower than the interested DOS features ($\approx 50-100\mu$V for coherence peaks), to avoid their broadening.

The dI/dV is recorded on user-defined patterns, for example, in horizontal lines, grids, and vertical lines to see how the tip-sample interaction affects the dI/dV. This signal can also be recorded during scanning to obtain dI/dV maps, setting the scanning speed slow enough to integrate the signal at least one time constant (voltage modulation period) per scan pixel.

Atomic and island manipulation

A tool that was used extensively in this work is the STM tip manipulation of atoms and Pb islands on graphene. This allowed studying the coupling in magnetic atom lattices and the tuning of the superconducting proximity effect in graphene.

The atom manipulation technique depends on many factors, such as the tip apex composition, the affinity of the atom with the substrate, and its adsorption configuration. In this work, we manipulate Mn atoms on β-Bi_2Pd using β-Bi_2Pd tips, with tunneling resistance of 100-200 kΩ. Fig. 2.12a shows how the tip is moved with respect to the atom with the feedback on while monitoring the tunneling current (horizontal manipulation). The typical manipulation current profile has a saw-tooth

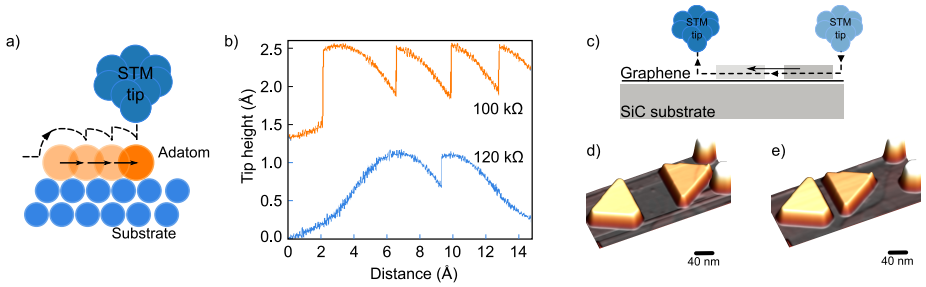

Figure 2.12: a) Lateral atomic manipulation where an STM tip pulls an atom on the surface. **b)** Tip height registered during the manipulation event, approaching the tip from R = 120 kΩ to R = 100 kΩ allows for continuous manipulation. **c)** Lateral manipulation scheme of a Pb island on graphene. **d-e)** Two manipulation stages of two Pb islands on Gr/SiC.

shape as the one we report in Fig. 2.12b each jump corresponding to the atom jumping between lattice sites. The tip must be prepared carefully, indenting slightly in clean β-Bi_2Pd until the manipulation works. Usually, tips with isotropic topography can manipulate atoms in all directions more reliably.

In this thesis, we use the Pb island manipulation technique on graphene, optimized in collaboration with Ivan Brihuega and Eva Cortez-del Rio. This allows moving laterally Pb islands on the surface of graphene with nanometric control. The methodology is sketched in Fig. 2.12c and consists in stabilizing the tip on graphene, removing the feedback, changing the bias to 0mV, and moving the tip towards the islands until contact. Then keep moving the tip in the same direction until the tip is in the desired final position for the island edge. The islands slide smoothly on the surface with no preferential directions and the process leaves the graphene intact with the island showing only slight defects at the touching point. Figs. 2.12c-e shows two frames before and after Pb island manipulation. The right island is pushed in the direction of the left island closing what we call a superconducting resonator. The islands align to the underneath graphene lattice allowing the natural placement of the islands' edges parallel to each other.

2.6 Experimental setup

The experiments were carried out in a commercial JT SPECS STM [Fig. 2.13] that works at a base temperature of 1.3K, in UHV conditions ($P < 1e^{-10}$ mbar) and allows up to 3 teslas out of the plane magnetic field. The STM is controlled by a Nanonis v4 SPECS unit. This provides the voltage and receives the current signal from a DLPCA-200 FEMTO Messtechnik current amplifier. The controller has an integrated lock-in amplifier, where the modulation is added directly to the generated bias. Both signals are filtered by an LC filter and divided by a 1/100 voltage divider that improves the applied bias resolution.

The STM chamber is attached to a preparation chamber and an MBE chamber. Here the samples are cleaned by sputtering-annealing cycles using an ion gun and an e-beam heating stage. The Au/Pb evaporation is done by pointing a metal evaporator directly to the sample surface and monitoring the evaporation rate with a quartz balance. In situ evaporation on the cold sample is done to have single Mn atoms on the surface. The Mn atom beam (e-beam evaporator) reaches the cold sample thanks to the evaporation ports in the STM radiation shields.

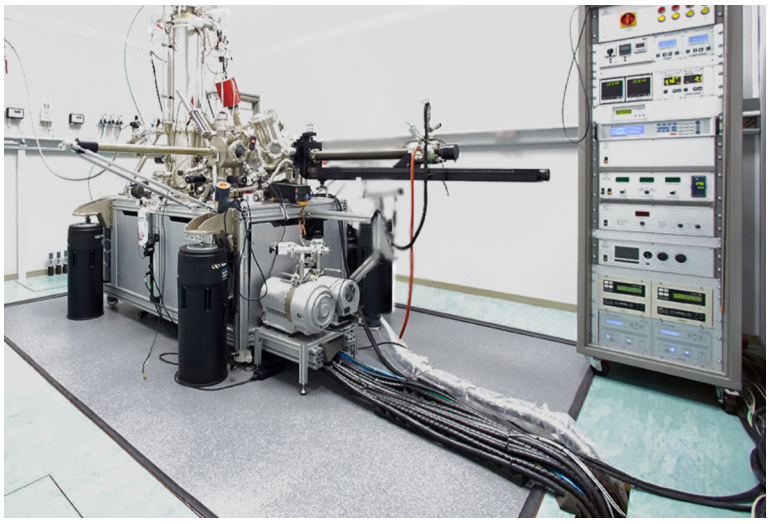

Figure 2.13: JT SPECS low-temperature STM. The machine is on the left, sitting on a concrete block for vibration isolation. The rack on the right allows for control of the STM and the preparation chamber.

3 Collective Yu-Shiba-Rusinov states in atomic lattices of Mn impurities on the β-Bi_2Pd superconductor

3.1 Introduction

Research on interacting spin ensembles on superconductors is a major interest in condensed matter physics. A common objective for this research is the study of Yu-Shiba-Rusinov (YSR) states [4–6], bound states for quasiparticles in superconductors that are induced by magnetic impurities and appear as excitations inside the superconducting gap [24, 56, 81].

Isolated magnetic impurities may present multiple YSR states spin-polarized along the impurity spin alignment direction [82–84] of the multiple impurity d-orbitals [11, 85–88]. Rusinov in [6] already predicted that ferromagnetically (FM) aligned impurities undergo energy splitting of the YSR peaks in bonding and anti-bonding states [Fig. 3.1a] when brought in close vicinity [13, 86, 89–92], while for anti-ferromagnetic (AFM) dimers only a small energy shift is expected. This phenomenology is due to the overlap of the oscillatory YSR wavefunction that together with Ruderman-Kittel-Kasuya-Yosida (RKKY) coupling results in an oscillatory behavior of the coupling [89]. This is reflected in the dI/dV spectra that we calculate for a YSR dimer in the function of the atomic spatial separation, showing an oscillatory splitting for FM con-

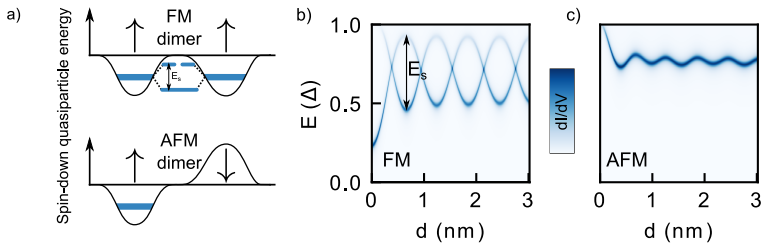

Figure 3.1: YSR coupling. **a)** Sketch of the potential well for quasiparticles for a magnetic atoms dimer. Ferromagnetic (FM) alignment results in overlap and in the formation of bonding-anti-bonding states, while in the AFM alignment, no overlap is present. **b)** Green function simulations adapted from [18] for FM atomic dimer where the splitting E_s oscillates with the distance. **c)** Same calculation for the AFM dimer, the YSR state does not split, and its energy oscillates with the distance merging with the coherence peak for small distances.

figuration [Fig. 3.1b] and a small oscillatory shift for AFM configuration [Fig. 3.1c] [18].

Two classes of YSR lattices can be defined on the basis of the coupling, the densely packed limit, where impurities couple via direct d-orbital overlap, and the diluted impurity limit, where YSR wavefunction overlap mediates the coupling. In the high-density limit, their YSR states form 1D or 2D quasiparticle bands. This was observed in spin chains [59, 93–95] or in 2D magnetic islands directly grown on superconductors [12, 31, 96–98]. Under specific circumstances, the bands may be topologically non-trivial, and become a potential platform for topological superconductivity and Majorana fermions [10, 99–101].

In the diluted impurity limit the coupling is mediated by the extended wavefunction of YSR states. As treated in chapter 2.2 the spatial extension of the YSR states is mediated by the dimensionality of the superconducting host and the shape of its band structure. This extends the YSR wavefunction nanometers away from the impurity [12, 14]. The large extension also enables an additional mechanism of indirect magnetic exchange between impurities, which competes with RKKY coupling [102]. YSR lattices in this diluted impurity limit have been proposed for the realization of topological superconductivity [17, 103]. 1D YSR structures in the diluted limit show collective behavior leading to delocalized excitations [16]. A natural extension is towards building structures, where the atomic spacing and the alignment with the crystal lattice are expected to play a crucial role in defining the excitation picture.

We start this chapter by giving a brief introduction to the study done on Mn dimers on β-Bi_2Pd started by Zaldivar in [104]. In this thesis, we continue this work exploring the formation of YSR lattices of Mn on β-Bi_2Pd where we demonstrate the importance of the orientation of the multi-impurity lattice with respect to the β-Bi_2Pd substrate lattice.

3.2 Mn single atoms and dimers on β-Bi_2Pd

The layered material β-Bi_2Pd is an s-wave superconductor with a critical temperature $T_c = 5.4$ K [106] and a superconducting gap Δ/e of around 0.75 mV [107–109]. The samples, were synthesized by E. Herrera, I. Guillamón. H. Suderow (IFIMAC, Madrid), are thin crystals (<1mm) 1-3 mm wide, and they are glued with low temperature conductive epoxy on Mo sample holders [104]. Thanks to the β-Bi_2Pd layered structure sketched in Fig. 3.2a, the samples are prepared via mechanical exfoliation in UHV conditions, exposing a square-symmetrical Bi-terminated surface with $a = 3.3$ Å (atomic resolution in the inset of Fig. 3.2b). The surface topography has frequent Bi vacancies visible as dark spots [Fig. 3.2b], that does not affect the superconducting gap [Fig. 3.2c], which is homogeneous on the surface. In this experiment, we use superconducting tips that are prepared by dipping the tip in the

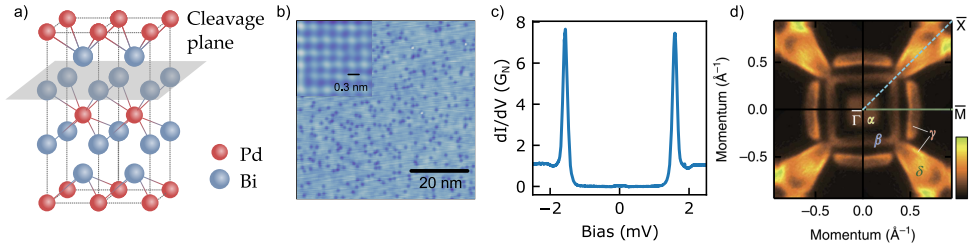

Figure 3.2: β-Bi_2Pd superconductor. a) The crystallographic structure of β-Bi_2Pd alternates Bi-Pd-Bi layers, with cleavage planes in between, reproduced from [104]. **b)** STM topography of a cleaved β-Bi_2Pd crystal showing Bi vacancies as depressions (V = 1 V, I = 100 pA) and the a = 3.3 Å atomic resolution in the inset (V = 3 mV, I = 10 nA), both reproduced from [104]. **c)** dI/dV spectrum of β-Bi_2Pd showing a superconducting gap that is homogeneous on the surface (V = 2.5 mV, I = 250 pA). **d)** Four-fold symmetrized Fermi surface of β-Bi_2Pd measured by ARPES, reproduced from [105].

β-Bi_2Pd substrate. In the result presented here, we use mainly tips with $\Delta_t/e = 0.68$ mV, giving coherence peaks at $(\Delta_s + \Delta_t)/e \sim 1.46$ mV.

The electronic structure of this material has been described by quasiparticle interference STM (QPI-STM), density functional theory (DFT) [110], spin- and angular-resolved photoemission spectroscopy (SARPES) [105]. Given its layered structure, the bands acquire strong 2D character with the presence two surface states [110]. The material has also strong spin-orbit coupling that causes most of the surface bands to be spin-polarized as demonstrated by SARPES. Fig. 3.2d shows ARPES results from [105] that reproduce the squared shape of the Fermi surface (FS) in reciprocal space. The FS anisotropy gives rise to high-density vector nesting along the parallel con-

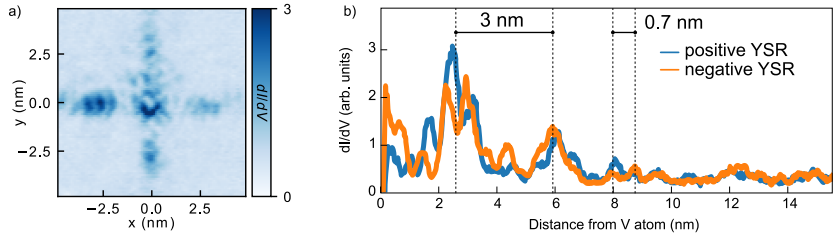

Figure 3.3: YSR wavefunction of a V atom on β-Bi_2Pd . a) dI/dV map the YSR state of a vanadium atom on Bi2Pd that reflects the anisotropy of the YSR wavefunction, reproduced from [18]. **b)** YSR intensity profile for positive and negative YSR of a V atom on β-Bi_2Pd extracted from a line-scan, that shows the presence of two modulations periods of 0.7 and 3 nm used as input for the model, adapted from [104].

tour branches [111], which is essential to understand the peculiar pattern of the YSR wave-function extension away from the impurity [12, 14, 104].

The long YSR extension in β-Bi_2Pd was studied in [104] mapping the YSR intensity on a single vanadium atom [Fig. 3.3a]. The spatial oscillation of the wavefunction display two modulations [Fig. 3.3b] resulting from the spin-polarized character of the YSR states and β-Bi_2Pd bands [104], a short modulation with $\lambda_1 \sim 0.7$ nm ($p_{F1} \sim 0.2/a_0$) and a longer one with $\lambda_2 \sim 3$ nm ($p_{F2} \sim 0.05/a_0$). Since in this work we explore mainly atomic distances < 1 nm and along directions non-collinear to the oscillations, we consider λ_1 as the main source of overlap modulation. Therefore we use p_{F1} as fixed parameter to model multiple Mn atom structures, which properties derive from the fundamental nature of the YSR wavefunction. Our model framework is a Green function approach developed with Jon Ortuzar and Sebastian Bergeret to describe N impurities in the presence of the squared Fermi surface of β-Bi_2Pd [18].

The Mn impurities were evaporated on a freshly cleaved sample at the STM base temperature T = 1.3K, and they absorb on 4-fold hollow sites. Single Mn atoms on β-Bi_2Pd are characterized by two types of spectrum (I,II) reported in Fig. 3.4a, adapted from [104] with majority of type I atoms. We found that this is not related to a different Mn atomic species since the same Mn atom can switch reversibly between two types of the spectrum when manipulated between different 4-fold hollow sites. This is probably related to the vicinity of the lattice site with a vacancy in the top or second substrate layer. The lateral manipulation with β-Bi_2Pd -coated superconducting tips grants high-resolution spectroscopy maintained during the building stages. This allows for identifying the type of lattice site, fundamental for engineering a homogeneous structure. Therefore, before constructing a structure, every lattice site used was checked by manipulating the same Mn atom at all sites making sure of having only type I Mn atoms.

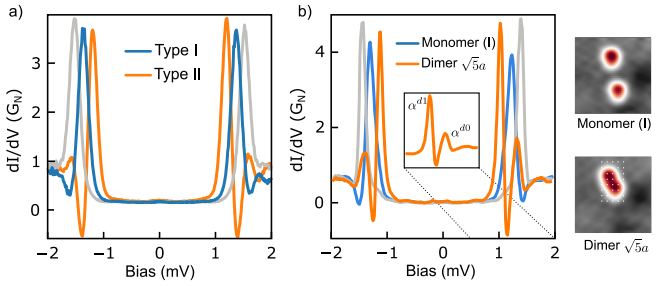

Figure 3.4: Isolated Mn atom and $\sqrt{5}$a Mn dimer. a) YSR state of the two Mn types found on β-Bi_2Pd (V = 3mV, I = 300 pA), adapted from [104]. **b)** Spectrum of a Mn dimer before and after dimer formation (topography on the right) showing the splitting in two components α^{d0} and α^{d1} (V = 3mV, I = 300 pA), adapted from [104].

In this chapter, we build YSR lattices of magnetic Mn atoms with atomic precision on β-Bi_2Pd superconductor. Structures with atoms in contiguous sites frequently change to form direct bonds [104], these structures are avoided in our experiments. The structures are stable when lying at next-neighboring sites, still being able to exchange interact and resulting in YSR splitting into two components [Fig. 3.4b] that we refer to as α^{d0} and α^{d1} . We build three different 5-Mn structures, differently oriented with respect to the β-Bi_2Pd lattice. The YSR splitting increases monotonically with the number of Mn atoms along (120) and (110) directions of β-Bi_2Pd , indicating ferromagnetic spin-alignment. Along the (100) direction, the YSR states shift towards the gap onset, pointing to anti-ferromagnetic spin alignment. The (120) direction shows the most pronounced splitting and a monotonic increase in particle-hole asymmetry that is absent in the (110) structures. To model the behavior, I use in collaboration with Jon Ortuzar a multiple impurity Green Function approach (model details in [18]) that we implement numerically in Python language for N impurities to get insight into the hybrid YSR states. In the 5 Mn structures, we model quantitatively the monotonic splitting depending on the cluster orientation. Surprisingly a small potential scattering results in a monotonic increase of the particle-hole asymmetry only for the (120) direction. In a 25 Mn atom square lattice, we map the YSR state spatial distribution and, with the aid of the simulations, associate it with collective YSR modes raising from the coupling.

3.3 Mn atoms linear chain along (120) direction

The Mn chains we present are built by adding the Mn atoms always on the same side of the chain along the (120) direction, resulting in an atomic separation of $\sqrt{5}$a . In Fig. 3.5a we show the STM topography of 3 snapshots of an 18 Mn atoms chain built along the (120) direction. In Fig. 3.5b we report a line of spectra along the three-atom chain. On the central atom, we see a YSR splitting greater than the atoms on the sides indicating wave-function overlap. This is more evident in the 9-atom chain snapshot of Fig. 3.5c, where the YSR energy of the last 3-4 atoms shows a continuous energy modulation indicating a collective behavior. The last snapshot with 18 Mn atoms of Fig. 3.5d start showing sign of disorder in the YSR energy, probably due to nearby Bi vacancies that start affecting the YSR coupling.

In Figs. 3.5e-f-g we show the simulated DOS done using only parameters extracted from the behavior of the single atom: $p_{F1} = 0.191/a_0$, $\xi = 20.4$ nm, $\alpha = \pi\nu_0 JS/2 = 0.030$, $\beta = \pi\nu_0 U = 0$ and the atomic coordinates extracted from STM. For the three-atom chain, the agreement is quantitative, and for the longer chains, it is evident that the YSR energy modulation interest the last Mn atoms on the side, while in the chain center, the YSR splitting is constant. This scenario does not change for the last snapshot of 18 Mn atoms, indicating a possible energy saturation.

To investigate this, we summarize the complete data set of all 18 different snapshots calculating the average α^{d1} component energy position. We plot the result in

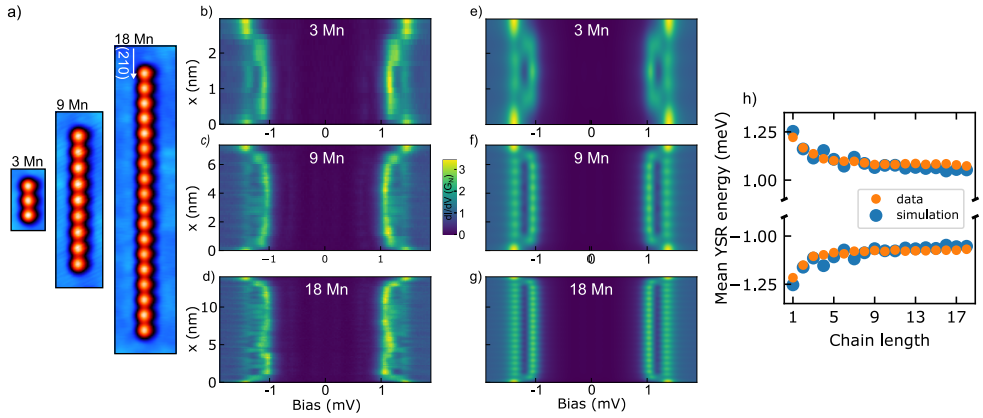

Figure 3.5: Building and measurement of 18 atom Mn chain along $\sqrt{5}a-(120)$. a) STM topography of three building stages of the Mn chain, final length 13.3 nm (V = 100 mV, I = 30 pA). **b-g)** STS line of spectra along the chains (V = 3mV, I = 300 pA) with the corresponding simulation using the Green function approach (parameters in the text). **h)** Energy of the α_{d1} YSR component extracted from the experiment and comparison with the model simulation (simulation parameters $p_{F1} = 0.191/a_0$, $\xi = 20.4$ nm, $\alpha = \pi\nu_0 JS/2 = 0.030$, $\beta = \pi\nu_0 U = 0$).

Fig. 3.6h and we observe that the average energy decreases relatively fast for the first 3-4 atoms added and then saturates at a constant energy value. In the background of Fig. 3.6h we plot the average of α^{d1} extracted from the simulated dI/dV. The isolated atom behavior defines all the input parameters, the excellent simulation agreement is the result of only one fitting parameter, the coherence length (ξ). Varying ξ we fit the data of Fig. 3.6h and obtain the best agreement with $\xi \sim 20$ nm, slightly higher than reported in the literature, but still reasonable for this material. We use this estimated value to perform all the simulations in this chapter.

The energy saturation is related to the fast decay of the YSR wavefunction along the (120) direction [Fig. 3.3b]. Although we have evidence of collective behavior, this configuration does not reach a zero energy crossing that is one requirement for topological superconductivity [10, 59, 112]. An obvious direction is to build structures along the (100) direction, that potentially has greater overlap. However, Mn dimers along the (100) with distance $2a$ were studied by Zaldivar and did not show any splitting, suggesting AFM spin alignment, and therefore not interesting for the absence of hybridization. In the next section, we corroborate this (100) AFM spin alignment assignation done by Zaldivar and study the rich behavior of 2D atomic lattices built along the different directions.

3.4 2D cross-like structures along different crystalline directions

In this section, we present three cross-like structures made by 5 Mn atoms made along the (100), (110), and (120). We measure the YSR splitting of the central Mn atom that results from the collective YSR wavefunction overlap of the 4 peripheral Mn atoms. In Figs. 3.6a-c we show a sequence of manipulation snapshots where the starting point is a central Mn atom with 4 atoms positioned at $3a$, $2\sqrt{2}a$ and $2\sqrt{5}a$ distance from it. The spectra of the atoms for the last two configurations are the same as for an isolated Mn atom. This changes for the $3a$ cluster where the YSR peak is at lower energy, this can be rationalized on the basis of the AFM interaction with the 4 neighboring atoms that shift the initial YSR energy.

Next, we manipulated with the STM tip the neighboring Mn atoms, sequentially pulling them towards the central Mn while its STS is monitored. For the structure along the (100) direction, we move the atoms from $3a$ distance to $2a$. In the spectra reported in Fig. 3.6a we observe how the energy of the main YSR peak maximum shifts slightly towards the gap edge. This indicates a sequential lowering of the exchange coupling, that occurs in the case of antiferromagnetic coupling.

We find a different behavior for the two non-collinear directions. In Fig. 3.6b we report the spectra mnipulating the atoms from $3\sqrt{2}a$ to $2\sqrt{2}$a . In the first step, we do not see a clear splitting, which could suggest a negligible interaction along the (110) direction. However, when we approach the additional atoms we indeed see a monotonic splitting of the peaks. The shift of internal YSR component α^{d1} increases

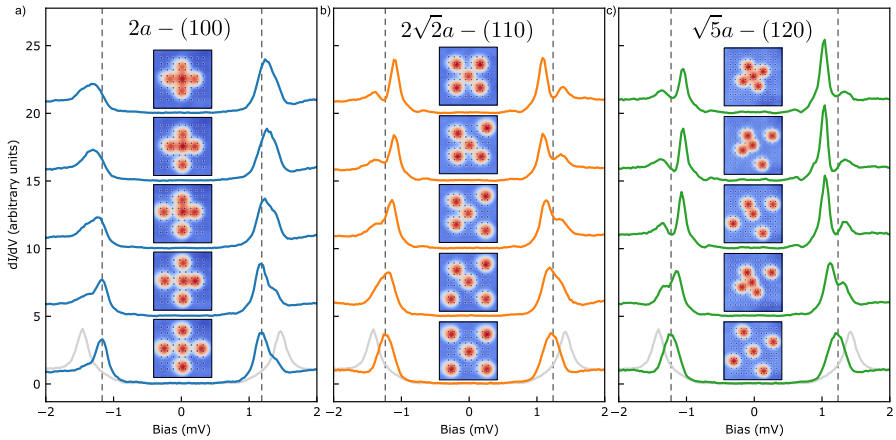

Figure 3.6: Central spectroscopy of Mn_5 cross like structures. a-c) STS of the central atom of the Mn structures after moving each lateral Mn atom, offset vertically for clarity (V = 5 mV, I = 500 pA). In the in-sets STM topography of the Mn cross-like structures of Mn on β-Bi_2Pd at the different stages of manipulation (V = 300 mV, I = 30 pA).

at every atom addition becoming maximum when the cross is completely formed. A slightly greater splitting is observed for the cross along the (120) direction, already visible from the first stage in Fig. 3.6c.

While the characteristics of the splitting are similar for the $\sqrt{5}$a and $2\sqrt{2}$a structures, the positive and negative YSR intensities behave differently. In STM for positive bias, we are tunneling with electrons and for negative bias, we are removing electrons (tunneling with holes). Therefore an asymmetry in the intensity of the positive and negative YSR is referred to as particle-hole asymmetry. If we compare this in the datasets of Figs. 3.6b-c, we see that for $2\sqrt{2}$a no particle-hole asymmetry is developed. Differently, the $\sqrt{5}$a cross develops a particle-hole asymmetry that monotonically increases after each addition. This is also present in the $2a$ cluster but the analysis is hindered since the peak is merging with the β-Bi_2Pd continuum.

We rationalize the observation by comparing the measured spectra with the Green function model simulation for the central Mn atom of all configurations. The gradual YSR shift towards the gap energy in the $2a$ cluster points to AFM spin orientation that effectively lowers the exchange. The simulation of the $2a$ clusters with an AFM spin alignment are shown in Fig. 3.7a. We note that the YSR peak slightly shifts at higher energy, qualitatively reproducing the effect observed in the experiment. For simulating the $2\sqrt{2}$a and $\sqrt{5}$a crosses we set an FM spin orientation, guided by the pronounced splitting observed experimentally. Remarkably the simulations in [Figs. 3.7b-c] quantitatively reproduce the YSR component α^{d1} that monotonically

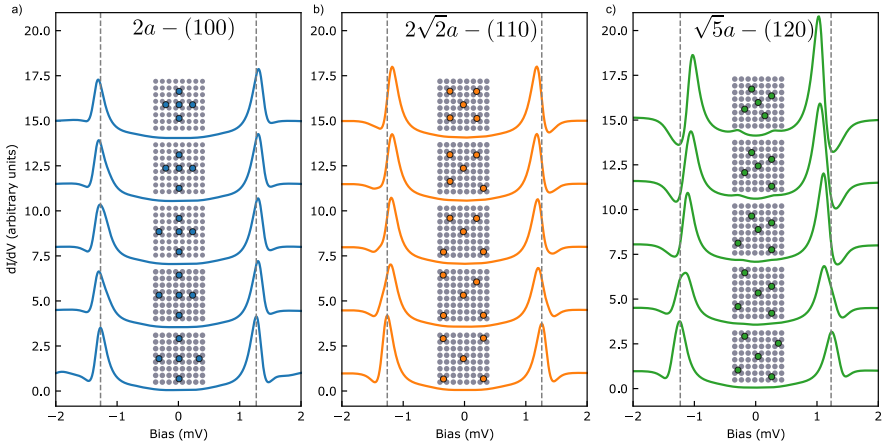

Figure 3.7: Model simulation of the 5 impurity structures with the Green function approach. a-c) The dashed lines indicate the energy position of the isolated atom. Same parameters (text) for all simulations except the atom positions (insets) and the spin orientation angle that is 90° for 2a-(100) while 0° for the other two configurations (simulation parameters $p_{F1} = 0.191/a_0$, $\xi = 20.4$ nm, $\alpha = \pi\nu_0 JS/2 = 0.030$, $\beta = \pi\nu_0 U = 0.014$).

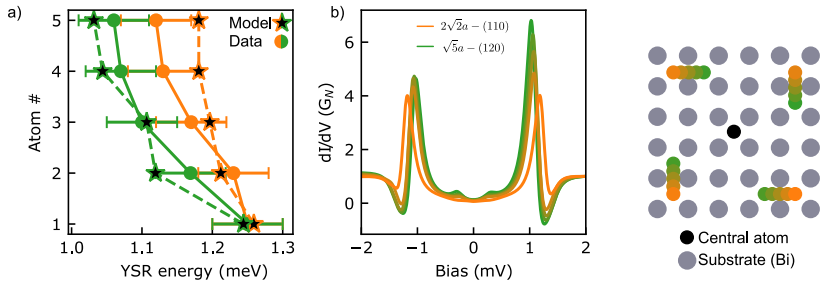

Figure 3.8: YSR energy and asymmetry simulation. a) Measured energy of the α^{d1} component for the $\sqrt{5}$a (green) and $2\sqrt{2}$a (orange) crosses, extracted from Fig. 3.6. The stars are energies of α^{d1} extracted from the model simulation of Fig. 3.7. **b)** Simulated dI/dV spectrum for the central atom of 5 Mn atom crosses going from a (110) to a (120) alignment (simulation parameters $p_{F1} = 0.191/a_0$, $\xi = 20.4$ nm, $\alpha = \pi\nu_0 JS/2 = 0.030$, $\beta = \pi\nu_0 U = 0.014$). On the right, we sketch the atomic positions for the calculated structures.

increases as the atoms are added to the structures. The α^{d0} component at energies close to the gap in the experiment is suppressed in the simulation due to the vicinity of the gap edge. In Fig. 3.8a we compare the measured and modeled magnitude of the α^{d1} components, obtaining a reasonable agreement. The splitting of the YSR state is monotonic with the number of added Mn atoms joined to the central atom, trend that tends to a saturation as observed for the linear chains.

Adding the Mn atoms to the crosses the YSR states also change gradually the particle-hole symmetry after every Mn atom addition. Considering the FM-aligned clusters, the behavior only manifests in the (120) cross, while is absent in the (110) cross. To model this we include a potential scattering term $\beta = \pi\nu_0 U = 0.014$ in our simulation. Remarkably, in Figs. 3.7c-d, the model reproduces the particle-hole asymmetry that is strongly dependent on the cluster orientation. In Fig. 3.8b we calculate the dI/dV for a cluster at various rotation stages between (110) and (120), observing a gradual increase of the particle-hole asymmetry.

3.5 Collective YSR modes in 25 Mn atom squared lattice

In this section, we present a 25 Mn atom squared lattice with a spacing $a_{Mn} = \sqrt{5}a = 0.74$ nm. In Fig. 3.9 we compare the spectra of the central Mn atom of three structures increasing the dimensionality. The general trend in the central Mn atom spectrum is a decrease in the YSR energy and the emergence of additional components induced by the coupling. We built the Mn square atom by atom using a normal tip that does not allow the recognition of type1 and type2 Mn atoms. After preparing a superconducting tip and relocating the structure, we recognize one of the atoms as accidentally a Mn type2, with a lower YSR energy (larger J) (see Fig. 3.4a). We show in Fig. 3.10a the dI/dV spectra for three atoms far away from the type 2 atom where

we observe 3 main in-gap spectroscopic features labeled α, β, and γ, apart from the coherence peaks. To rationalize this apparently complex spectrum, we employ our Green function model using the same simulation parameters as the previous sections, apart from the potential scattering, which we set here to zero for simplicity. The black line in Fig. 3.10a is a simulation of the central atom showing three main in-gap YSR resonances that dominate the spectrum for all the square atoms.

With a 64x64 points spectroscopic grid, we mapped experimentally the YSR energies at $V_\alpha \sim 0.95$ mV, $V_\beta \sim 1.05$ mV, $V_\gamma \sim 1.30$ mV. In Fig. 3.10b, in the experimental raw data grid, we observe that the symmetry of the maps is reduced, due to the presence of a type 2 Mn lattice site indicated by a cross. In Fig. 3.10b we show the grid simulated with our model for a perfect square. We plot the model grid cuts at the energy of the three resonances α, β, and γ. Although we can find some similarities with the experimental map, the presence of the defect hinders direct comparison with the simulation. To circumvent this we use two methods: first, we perform a symmetrization of the raw data, and second we simulate the structure by inserting a type II Mn atom in the square to reproduce the defect.

The structures together with the substrate have C_4 symmetry that does not contain mirror planes, due to the rotation between the β-Bi_2Pd and the Mn lattice. In fact, the main symmetry direction of the Mn lattice is the (120), which is rotated by $\sim 26.6°$ with respect to the β-Bi_2Pd surface lattice. According to the C_4 group we symmetrized the maps in Fig. 3.10b averaging 4 maps rotated by 90° each with respect to the Mn lattice high symmetry direction. The symmetrized maps in Fig. 3.10b show indeed a better correlation with the simulated map. The state α is located in the center, β on the atoms close to the corners, and the state γ in the edge of the square. We note that these features are also visible in the raw maps, with a lowered symmetry and modified intensity. Instead of symmetrizing the experimental maps we can break the symmetry in the simulation, setting a higher exchange for the defective

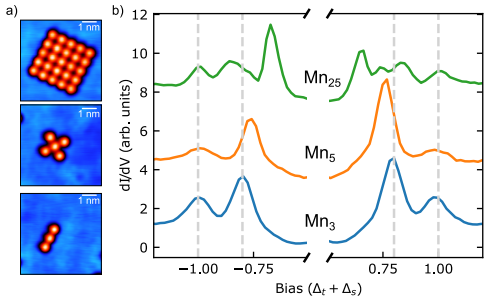

Figure 3.9: Comparison of YSR excitation for increasing dimensionality. a) STM topography of three Mn structures built with a minimum spacing of $\sqrt{5}$a with an increasing number of atoms (3,5 and 25 Mn). **b)** From the bottom: STS on the central atom of the 3Mn chain (blue), and the 5Mn structure (orange).

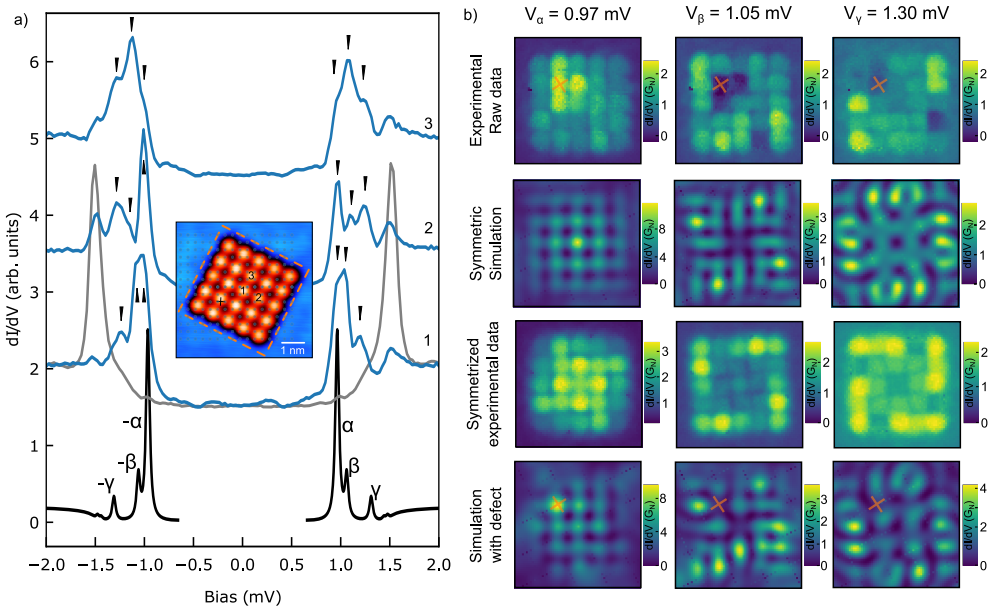

Figure 3.10: Squared Mn_{25} structure. a) In the STM topography the type 2 Mn atom is indicated with an orange cross. Spectra on indexed atoms of the structure (1,2,3), far from the type 2 Mn. The recurrent YSR modes (α, β, and γ) are highlighted in the spectra and visible in the simulation of the central atom at the bottom of the graph (black curve). **b)** In the first raw of the raw dI/dV maps extracted from grids. In the second raw the C_4 symmetrized maps. In the third row the simulations at the three modes' energies. In the fourth row the simulation including the effectual Mn type 2 (simulation params $p_{F1} = 0.191/a_0$, $\xi = 20.4$ nm, $\alpha = \pi\nu_0 JS/2 = 0.030$, $\alpha_{\text{Mn type2}} = \pi\nu_0 J^* S/2 = 0.06$, $\beta = \pi\nu_0 U = 0$).

atom to simulate the presence of a type 2 Mn [Fig. 3.4a]. The result is reported in Fig. 3.10b where we see a better agreement with the raw experimental maps. This is evident in peak β where the state is more localized to the bottom of the Mn lattice, with α, where the spectral density is enhanced around the defect, and in γ where the symmetry of the edge state is broken.

3.6 Discussion and conclusions

Mn atoms have an S = 5/2 spin configuration, and multiple YSR resonances due to the orbital character [11] are observed in other substrates, where the crystal field lifts the degeneracy of the d orbitals [11, 86, 92]. For Mn on β-Bi_2Pd the YSR peak width is relatively broad and was interpreted by Zaldivar as 5 YSR components overlapping [104]. In our experimental data, the YSR channels upon hybridization show the same coupling without the appearance of additional components in our energy resolution window. Our model can capture the experimental observations

quantitatively with a minimal classical-spin single-channel (S=1/2) model without any orbital structure. This seems rather coincidental, but plausible since the coupling is mediated only by the YSR overlap and not by the direct orbital overlap.

The Fermi surface anisotropy of β-Bi_2Pd shapes the coupling between magnetic atoms along different crystallographic directions. This phenomenology is visualized in the cross-like structures, which splitting depends on the cluster orientation. In this study, we show that the cluster orientation also affects the particle-hole asymmetry of the central YSR state. The presence of particle-hole asymmetry in the YSR states is often connected with potential scattering effects [113, 114]. Previous studies did not report a change of particle-hole asymmetry on the orientation of the structures [59, 112, 115] or did not focus on this aspect [91, 116]. Our model calculation reproduces this behavior observed in the (120) cluster with the simple addition of a potential scattering. This points to an interplay of the anisotropy of the overlap with the potential scattering resulting in a gradual increase of the particle-hole asymmetry in the central atom. This effect gradually disappears when the structure is oriented along the (110) direction, confirming the fundamental role of the coupling anisotropy in defining the particle-hole asymmetry.

This symmetry breaking is well visible in the simulated maps for the 25 Mn atoms lattice. A common behavior that occurs in atom lattices is the lifting of the level degeneracy and the formation of delocalized modes when increasing the lattice extension [117]. In the dimers and atomic crosses, the wave functions of the lateral atom are concurrently overlapping, resulting in an increasing splitting of the central Mn atom. In the extended 25-atoms squared lattice, we can change from a dimer overlap perspective to a delocalized YSR modes perspective. The dI/dV maps allow visualizing the spatial distribution of three confined YSR modes in Fig. 3.10 that are differently distributed on the structure, α having a central maximum, β mainly on 4 peripheral atoms, and γ distributed on the edges. Note how the simulated maps have a 4-fold symmetry, importantly lacking the mirror planes due to the rotation with respect to the β-Bi_2Pd . This has the consequence that there are two possible squared lattices that one can build on the surface, connected by a mirror symmetry operation.

In conclusion, we show how we can control and simulate the YSR states in atomically precise Mn lattices on β-Bi_2Pd . The anisotropic character of the Fermi surface implemented in a Green function formalism can account for the different stages and orientation of the structures when additional impurities are added. The symmetry breaking due to the rotation with respect to the β-Bi_2Pd lattice of the 5-Mn structure changes the splitting and particle-hole asymmetry that raises from the YSR lattice rotation with respect to the substrate. This offers an alternative route to tune YSR energy and particle-hole asymmetry [116, 118, 119]. In a 25 Mn atom squared lattice we observe multiple YSR modes that can be connected to collective YSR modes. With our multi-impurity model, we can simulate arbitrary structures, allowing com-

parison with the experiment to obtain agreement and insight into the YSR collective excitations.

4 Cooper Pair Excitation Mediated by a Molecular Quantum Spin on a Superconducting Proximitized Gold Film

Cooper Pair Excitation Mediated by a Molecular Quantum Spin on a Superconducting Proximitized Gold Film
Stefano Trivini, Jon Ortuzar, Katerina Vaxevani, Jingchen Li, F. Sebastian Bergeret, Miguel A. Cazalilla and José Ignacio Pascual.
Phys. Rev. Lett. **130**, 136004 - Published 30 March 2023

4.1 Introduction

Superconducting materials are an ideal platform for designer quantum states with potential as qubits [25, 120, 121]. The superconducting ground state, a condensate of Cooper pairs, is protected from quasi-particle excitations by a pairing energy gap Δ. Ground state excitations can be achieved by electrons [2], correlated pairs in Josephson currents [122, 123], or microwave photons [26, 124, 125]. In bulk superconductors, these excitations populate a continuum of Bogoliubov quasiparticles (QPs) and admix with other states that quickly quench their quantum coherence. Sub-gap quasi-particle excitations, in contrast, can live long in a coherent state. For example, sub-gap Andreev bound states in a proximitized link between two superconductors host addressable (doublet) QPs and (singlet) pair-breaking excitations with long quantum coherence [25, 120]. QP states are odd in fermion parity and can be excited by adding a fermion to the even-parity BCS ground state [Fig. 4.1a]. Pair excitations require *two* correlated QPs into the pair-excited state, thus, with even-parity [3]. Therefore, they are only accessible by absorption of one microwave photon or by the addition of two fermions with opposite spin [Fig. 4.1a].

Sub-gap excited states can also appear when a magnetic impurity interacts with a superconductor via magnetic exchange J. These are the Yu-Shiba-Rusinov (YSR) [4–6] excitations, which are typically addressed by tunnelling electrons from a scanning tunneling microscope (STM) [15, 23, 59, 85]. YSR excitations correspond to the addition of a tunneling electron/hole into the ground state and appear in tunneling spectra as sub-gap bias-symmetric pairs of narrow peaks. In the regime of weak exchange interaction J compared to the pairing energy Δ, YSR peaks are thus QP excitations of the BCS ground state. Pair excitations are, however, forbidden because these would require the tunneling of two correlated electrons simultaneously [Fig. 4.1b].

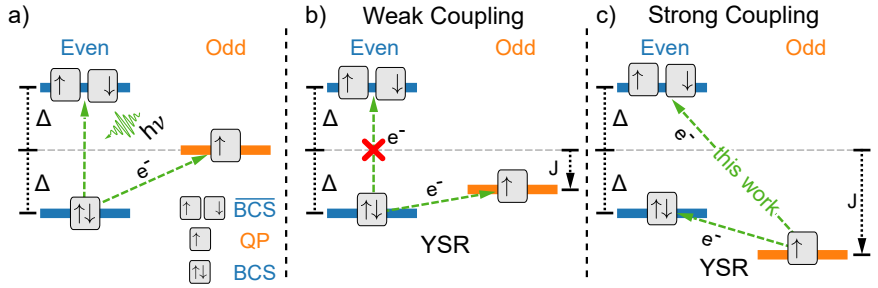

Figure 4.1: Excitation scheme of a superconductor exchange coupled to a magnetic impurity. **a)** Scheme of the excitations of a superconductor with energy gap Δ. Pair excitations ($\overline{\text{BCS}}$) can be probed by microwaves, while electrons can excite Bogoliubov quasiparticles. The arrow boxes refer to the number of quasiparticles involved. **b)** The exchange J induces YSR bound states below Δ. Due to parity selection rule single electrons cannot excite the pair excitation ($\overline{\text{BCS}}$). **c)** Increasing J, the ground state becomes odd in parity, and the $\overline{\text{BCS}}$ state becomes accessible.

Here, we report the observation of Cooper pair excitations in the YSR spectrum of an Iron Porphyrin molecule on a proximitized gold thin film. Owing to the magnetic anisotropy of the molecule, YSR states appear split in multiple resonances both inside and outside the proximitized gap. When the molecule lies in the Kondo-screened regime (J larger than Δ) pair excitations emerge as faint spectral resonances, scaling in energy with twice Δ. Supported by model calculations for quantum spins, we show that inducing pair excitations with single particles does not contradict parity-conservation rules when the magnetic molecule lies in the Kondo regime because the magnetic impurity is screened by a captured QP, turning the ground state odd in fermion-parity. [81, 118, 128–130]. From this ground state, single-particle tunneling allows now YSR excitations into even states such as the BCS state and its higher-lying pair-breaking excitation $\overline{\text{BCS}}$ [Fig. 4.1c].

4.2 FeTPPCl on proximitized Gold film

Our measurements were performed at 1.2 K using an STM (SPECS GmbH) under ultra high vacuum conditions. We used a V(100) single crystal as superconducting substrate (T_c= 5.4 K and Δ_V(1K)=0.75 meV). The clean V(100) surface appears with the characteristic (5x1) oxygen reconstruction [131, 132], which does not affect its superconducting properties [58, 62, 133–135]. The V(100)-O(5x1) surface was covered with gold films, with thicknesses ranging from 1 to 10 ML, and shortly annealed to ∼550°C to produce epitaxial layers [Fig. 4.2a] with a 2.9Å square lattice [inset Fig. 4.2a], compatible with an unreconstructed Au(100) surface [136, 137], probably with some intermixing with the vanadium substrate [138].

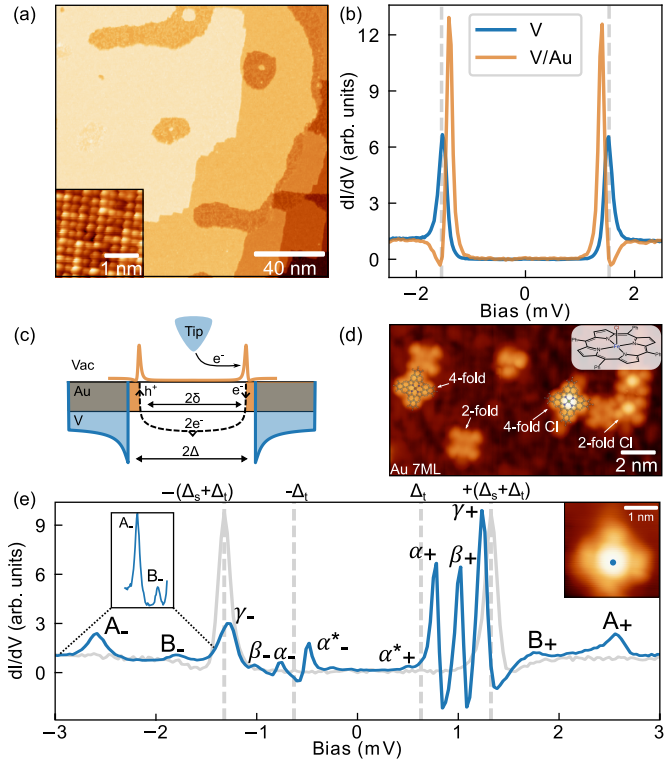

Figure 4.2: FeTPPCl on a proximitized Gold film. **a)** STM image of the epitaxial film produced by depositing 2 ML of Au on V(100) and annealing to 550°C (V_S = 10 mV, I = 100 pA). Inset: constant height STM image of its square atomic lattice (V_S = 10 mV). **b)** dI/dV spectra measured on V(100) and on Au/V. **c)** Andreev reflections at the interface with V(100) deplete the film DOS and open a gap in the normal metal. **d)** STM image showing different FeTPP and FeTPPCl species on 7 ML Au/V(100) (V_S = 300 mV, I = 30 pA), Inset: chemical structure of FeTPPCl. **e)** *dI/dV* spectrum measured over a 4-fold FeTPPCl molecule (in gray on the Au film), labelling two extra-gap states (A,B) and four intra-gap resonances ($\alpha, \alpha^*, \beta, \gamma$). ($V_S$ = 3 mV, I = 75 pA). Data analysed with WSxM [126] and SpectraFox [127].

The proximitization of the gold thin film was ascertained by comparing *dI/dV* spectra over the films and the bare V(100)-O(5x1) surface [Fig. 4.2b]. To enhance the spectral resolution we used superconducting tips obtained by tip indentations in the V(100) substrate. Spectra on V(100) show an absolute gap and two sharp peaks at $\pm(\Delta_t + \Delta_V)/e = \pm$ 1.5 mV [Fig. 4.2b], corresponding to the convolution of the superconducting density of states of tip (Δ_t) and sample ($\Delta_V/e = 0.75$ mV). Spectra on the investigated gold films also exhibit a similar hard gap [139], but with a pair of very sharp resonances at slightly smaller bias of $\pm(\Delta_s + \Delta_t)/e = 1.4$ mV. These peaks are attributed to QP excitations of de Gennes Saint-James (dGSJ) bound states in the gold film [140], which are Andreev pairs confined between the Au surface and the

Au-V interface [Fig. 4.2c]. Owing to their confinement, the dGSJ QP excitation peaks shift to lower energy with increasing Au film thickness [68, 141–144], and therefore are a useful knob for tuning the gap Δ_s in the experiment.

Next, we deposited the organometallic molecule iron tetraphenylporphyrin chloride (FeTPPCl) [Fig. 4.2d] on the proximitized gold films. This species hosts an Fe^{3+} ion with a S=5/2 spin and easy plane magnetic anisotropy, which survives on metallic surfaces [23, 145]. Some of the molecules retain the Cl ligand [Fig. 4.2d], and appear with two different shapes: the two-fold symmetric FeTPPCl interact weakly with the substrate [144], while the four-fold symmetric molecules investigated here behave as quantum impurities coupled to the superconducting substrate.

Spectra on the four-fold FeTPPCl molecules are characterized by a complex pattern of intra- and extra-gap resonances, as summarized in Fig. 4.2e. Measuring with a superconducting tip, direct YSR resonances appear between $\pm\Delta_t$ and $\pm(\Delta_t+\Delta_s)$. We typically find three intra-gap pairs of peaks ($\alpha_\pm$, $\beta_\pm$ and $\gamma\pm$) that appear with larger intensity at positive bias due to finite potential scattering [57, 146]. Additionally, the thermal YSR excitation $\alpha^*_\pm$ is observed below $\pm\Delta_t$ in the spectra.

In addition, *dI/dV* spectra show fainter peaks [$A_\pm$ and $B_\pm$ in Fig. 4.2e] above the proximitized gap. Since peak A lies at 1.3 meV above the gap-edge resonances, it can be associated with the $M_s = \pm 1/2 \rightarrow M_s = \pm 3/2$ spin-flip excitation of the molecular spin multiplet, with axial anisotropy constant D=0.65 meV [20–23, 144]. The origin of peak B, at $\sim$ 0.6 meV outside the gap, cannot be directly connected with inelastic spin transitions. Instead, as shown in the following, peak B corresponds to a pair excitation of the superconducting condensate.

A hint on the origin of superconductors excitations can be obtained from their evolution with exchange coupling (J) variations [81, 118, 119, 129, 130]. In tunneling regime, the STM tip exerts attractive forces that distort the *flexible* molecular system and reduce J. Moving the tip away from the molecular center reduces this effect and causes an increase in J and a shift in *dI/dV* peaks. In the spectral map of Fig. 4.3a, the three intra-gap YSR resonances shift to lower energies as the measuring position is laterally changed from the center towards the phenyl groups. For the α state the shift is large enough to cross the Δ_t line and exchange position with the thermal state α^*. This is a fingerprint of a parity-changing quantum phase transition (QPT) in the ground state of the molecule-superconductor system [81, 118, 129].

Unexpectedly, the extra-gap peaks A and B change intensity and position with J following different trends [Fig. 4.3b]: peak A vanishes towards the sides, while peak B, fainter in the center, shift to higher energies. The apparent connection of the shifts of extra-gap peaks with intra-gap excitations [Fig. 4.3c] suggests they are all related to the same many-body state, renormalized by the tip-induced changes in J. This state is formed by the spin S=5/2 of the quantum impurity, with D $\sim$0.65 meV, coupled to the superconducting substrate with quasi-particle excitation peaks at Δ_s.

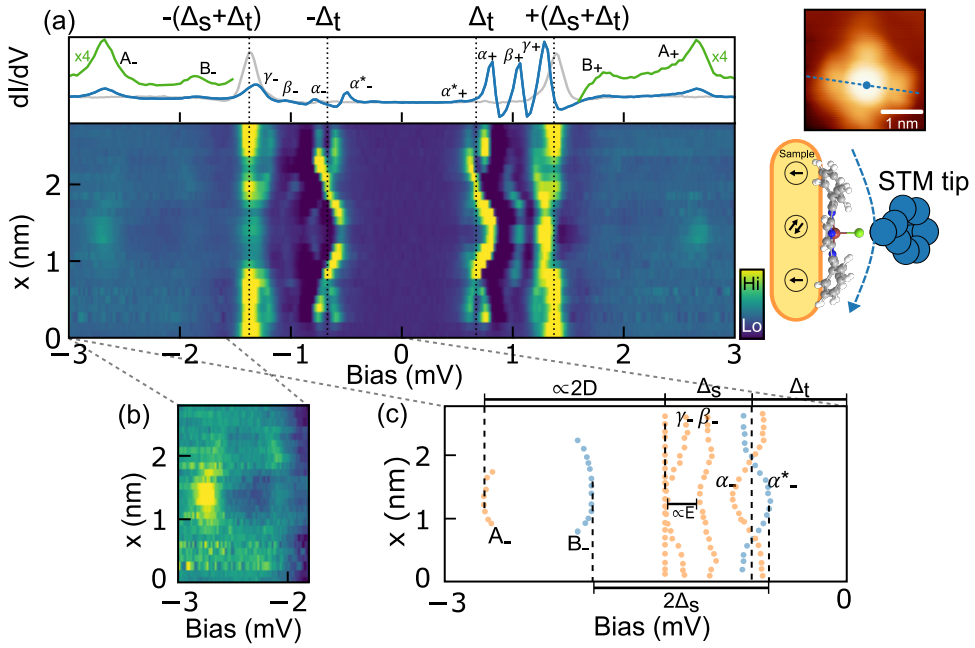

Figure 4.3: STM tip tuning of the exchange coupling. **a)** Map of dI/dV spectra measured across a 4-fold FeTPPCl molecule (sketched on the right) with V_S = 3 mV and I = 75 pA. The spectrum on top is measured over the center. **b)** Zoom of the extra-gap spectral region to highlight signals A and B. **c)** Energy position of peaks at negative bias extracted from the line profile.

4.3 Spin-5/2 quantum spin coupled to a single site superconductor

To interpret the results we used a minimal single-site model [54, 147], extended for quantum impurities on superconductors by von Oppen and Franke [24, 148]. Calculations using this model are light and provide useful insights into the many-body spectrum of the system. The Hamiltonian reads:

$$\begin{aligned} H_s &= H_0 + H_M + H_J \\ H_0 &= \Delta_s c_\uparrow^\dagger c_\downarrow^\dagger + \text{h.c.} \\ H_M &= DS_z^2 + E(S_x^2 - S_y^2) \\ H_J &= \sum_{\sigma\sigma'} c_\sigma^\dagger [J_z S_z s_{\sigma\sigma'}^z + J_\perp (S_+ s_{\sigma\sigma'}^- + S_- s_{\sigma\sigma'}^+)] c_{\sigma'}, \end{aligned} \tag{4.1}$$

where H_0 describes a single-site superconductor, and H_M accounts for the magnetic impurity spin anisotropy, with transversal components E. The term H_J represents the (anisotropic) J between impurity and superconductor states characterized by J_z and $J_\perp$, axial and transverse exchange couplings, respectively.

In Fig. 4.4a we display the evolution with D and J of excitation energies in a tunneling experiment, obtained from the eigenstates of Eq. (4.1). Adding a tunneling electron (or hole) to the ground state of the system leads to a change in fermion parity. Therefore, only transitions between even and odd parity states are allowed [blue and orange in Fig. 4.4a]. For negligible exchange J, the molecular anisotropy D splits the spin multiplet into non-degenerate levels of equal S_z (left side in Fig. 4.4a. The ground state is a product state of the molecular spin-doublet and the BCS ground state:

$$|\text{even}\rangle = |S_z\rangle \otimes |\text{BCS}\rangle = |\pm 1/2\rangle \otimes (|0\rangle + |2\rangle) \tag{4.2}$$

with $|0\rangle$ the vacuum and $|2\rangle = c_\uparrow^\dagger c_\downarrow^\dagger |0\rangle$. Tunneling experiments in this regime resolve peaks caused by a QP excitation at $\pm\Delta_s$, and by an additional spin excitation at $\pm(\Delta_s + 2D)$ [22, 23, 144]. The spin multiplet in the BCS ground state can also be thermally populated when $k_b T > 2D$ [129].

A finite exchange J [right panel in Fig. 4.4a] mixes the spin multiplet with Bogoliubov QPs into *symmetric* (+) and *anti-symmetric* (-) entangled states with definite total spin projection S_z^T [149, 150]. As shown in Fig. 4.4a, symmetric states appear as excitations outside the gap, while the anti-symmetric ones correspond to intra-gap excitations. For example, peak A in our experiments corresponds to the excitation of the entangled symmetric state with S_z^T=1 [22], while the antisymmetric state is a YSR excitation split by the axial magnetic anisotropy [24, 129, 149, 150]. In fact, resonances β and γ observed in the experiment are reproduced when a small transversal anisotropy E is also included to further split this state into two (see appendix 4.6).

Increasing J above a critical value induces a QPT [Fig. 4.3a], where the ground state becomes an odd parity entangled state of impurity's spin and a QP [60, 118]:

$$|\text{odd}\rangle = |1/2\rangle\,|\downarrow\rangle - |-1/2\rangle\,|\uparrow\rangle \ . \tag{4.3}$$

From $|\text{odd}\rangle$, there are two even parity states accessible by tunneling electrons or holes: the state (4.2), resulting in the YSR peaks α in spectra, and the state:

$$\overline{|\text{even}\rangle} = |\pm 1/2\rangle \otimes \overline{|\text{BCS}\rangle} = |\pm 1/2\rangle \otimes (|0\rangle - |2\rangle). \tag{4.4}$$

This second state is a pair excitation, i.e. the excitation of two QPs over the BCS state: $\gamma_\uparrow^\dagger \gamma_\downarrow^\dagger |\text{BCS}\rangle = \overline{|\text{BCS}\rangle}$ [3]. The pair excitation lies at an energy $2\Delta_s$ above the YSR state, hence, it is independent of the molecular magnetic anisotropy [Fig. 4.5a]. As we discuss next, peak B in the spectra corresponds to this pair excitation.

In Fig. 4.4b we show a calculated spectral line profile simulating the experimental results of Fig. 4.3a, obtained by solving the Hamiltonian (4.1). We obtain J from the position of α, $D = 0.65$ mV from measurements on weakly coupled molecules [144], and we include a small transversal anisotropy E that replicate β (see appendix 4.6). The results account for all excitations observed and reproduce their evolution with J, by using a single orbital channel. Fermion parity selection rules explain

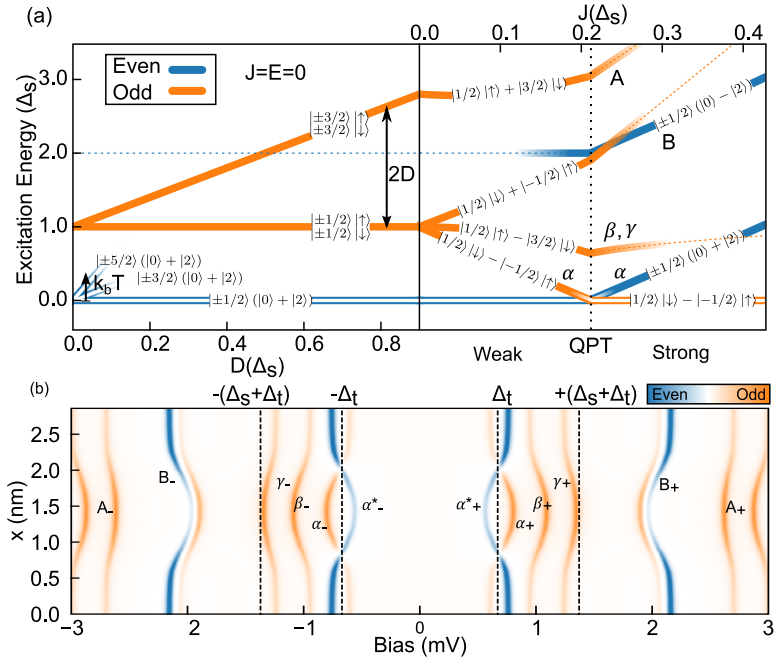

Figure 4.4: Single site model for S=5/2 single channel quantum spin. a) Allowed electron excitations, and their parity, for a spin $5/2$ coupled to a superconductor, obtained from eq. 4.1 Left: spin multiplet split by magnetic anisotropy D. Right: exchange coupling J leads to in-gap states. Around the QPT, thermal effects are shown as gradient lines. **b)** Simulation of a spectral map like in Fig. 4.3a using the effective model, adopting as input the position of α and the re-normalized D (see appendix 4.6).

that peaks A, β and γ fade away when the molecule enters in the strong interaction regime. Furthermore, the stronger intensity of peak B in this regime, and its shift with J agrees with the behaviour of pair-excited state $\overline{\text{BCS}}$.

4.4 Pair excitation correlation with Δ_s

To further corroborate the identification of peak B as a pair excitation, we studied the evolution of peak A and B on 15 molecules lying on different regions and film thicknesses [Fig. 4.5a], with different values of Δ_s [Fig. 4.5b]. In these molecules, the position of peak B, measured with respect to α, scales with $2\Delta_s$ [Fig. 4.5d], as expected for pair excitations, ruling out other possible origins [151]. In contrast, the position of peak A with respect to Δ_s, i.e. $2D$, is uncorrelated from Δ_s [Fig. 4.5c].

The different evolution of peaks A and B with J is reflected by comparing spectra on the center of three molecules in different interaction regimes [Fig. 4.5e]. Peak A

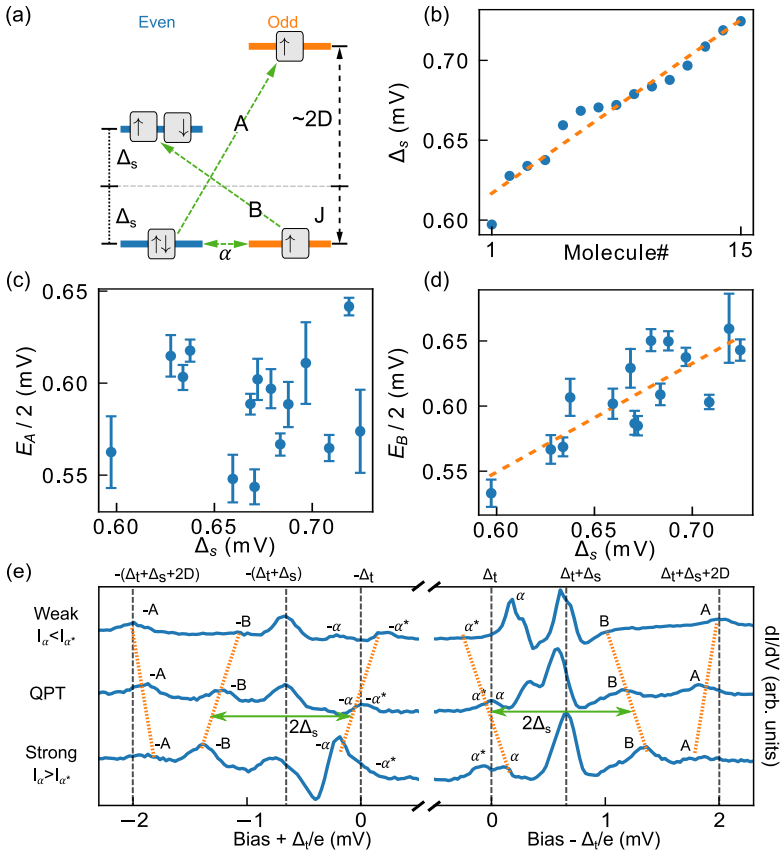

Figure 4.5: Pair excitation correlation with Δ_s. a) Scheme of A and B excitations (J fixed to the QPT point); Peak A scales with anisotropy D and Peak B with Δ_s. **b)** Value of Δ_s measured close to 15 different molecules lying on different positions on the substrate, and on film with different thickness. **c)** Position of peak A for the 15 molecules, showing no correlation with Δ_s. **d)** Evolution of peak B with Δ_s, showing a linear dependence. E_A is the energy of peak A over the gap edge, while E_B is the energy of peak B with respect to YSR state α. **e)** Spectra of three molecules of the set, in weak, at QPT, and strong regimes (detected through the particle-hole asymmetry of α). Peak A is more intense in the weak coupling case, while peak B in the strong coupling regime.

shifts to lower energy with increasing J, due to renormalization of D [22], and vanishes in the strong coupling case. Peak B, in contrast, becomes more intense in the strong coupling regime and shifts with J parallel to α, spaced by $2\Delta_s$, as expected for the pair excitation.

To date, pair excited states were only observed through adsorption of microwaves [25, 120] photons or Andreev pairs [123]. Fermion-parity conservation forbids a sin-

gle tunneling electron from exciting a pair of Bogoliubov quasi-particles (the $\overline{\text{BCS}}$ state) in a superconductor. In our experiment, the observation of the pair excitation with electrons was made possible by the existence of an odd-parity Kondo-screened ground state of a magnetic molecule state on a superconductor, which enabled the excitation of two even-parity states [Fig. 4.3]: the BCS state, leading to the intra-gap YSR resonance and the $\overline{\text{BCS}}$ pair excited state, observed as peak B. Even if this resonance appears outside the spectral gap, the pair state in the proximitized film is a double population of a subgap state and, hence, it is expected to have a larger lifetime, facilitating its detection.

It is noteworthy that the quantum spin model used here accounted for all observed resonances using just one single channel. Multiple sub-gap excitations resulted by entangled states of impurity and quasiparticles, mixed by magnetic anisotropy constants D and E. As we show in the appendix 4.6, a small value of E suffices to justify peak β, because the YSR excited state is integer and with large spin. This model successfully explains the important role of transversal and axial anisotropy and the effect of exchange on the magnetic anisotropy.

4.5 Conclusions

In conclusion, we have used a proximitized gold film as a platform for studying many-body excitations in magnetic impurities [139]. The magnetic molecule FeTPPCl interacting with the substrate electrons host subgap YSR states and spin excitations outside the gap that are readily described by a superposition of Bogoliubov quasiparticles and impurity spin states using a zero-bandwidth model. Interestingly, we found an excitation of a $\overline{\text{BCS}}$ pair state on molecules in the Kondo-screened regime, which scales with the different pairing energy of proximitized films of different thicknesses. This is an excitation that remains hidden to tunneling electrons and becomes available for magnetic impurities that bind a quasi-particle, thus behaving as a detector of the parity of the ground state. In a proximitized metal film, the excited pair populates dGSJ sub-gap states and inherits their coherent and spatial evolution and, thus, their potential for becoming elementary states for quantum processing.

4.6 Appendix

Deconvolution and fitting of the proximitized gap

In this section we show how the V(100)/Au system can be well described by a ballistic SN junction model developed by Arnold [68]. The clean V(100) surface shows the known (5x1) oxygen reconstruction that manifests in the STM topography [Fig. 4.6a] as a series of lines with periodicity 5 times the vanadium lattice parameter [131, 132]. As explained before, annealing to 550C after Au deposition forms homogeneous Au films on the surface [Fig. 4.6b]. The spectrum of vanadium is strongly modified by the presence of gold. In Fig. 4.7c we report the DOS spectra before and

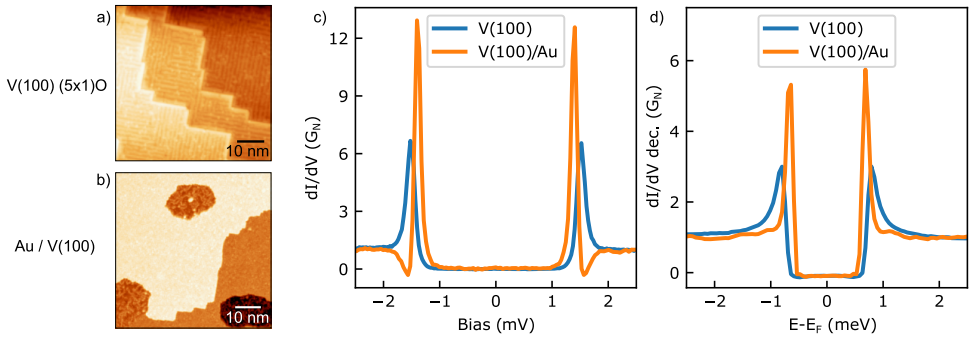

Figure 4.6: BCS gap compared with dGSJ resonances. a) STM topography of V(100) with the 5x1 oxygen reconstruction. **b)** STM topography after gold evaporation showing Au layers. **c)** On bare V(100) the spectrum shows BCS like density of states, after Au deposition the coherence peaks shift at lower energy and a dip feature appears at $2\Delta_V$. **d)** Deconvolution of the spectra in b).

after deposition. Note as the gap closes and a dip-like feature appears at $2\Delta_s$. If we deconvolute the two spectra [Fig. 4.6d] we see that V(100)/Au has a sharper peak line-shape.

The most direct way to model this line-shape is using the ballistic Arnold model density of states [eq.2.30] that describes the tunneling density of states of an SN junction. To do so, we implement the Python code to compute the temperature-broadened convolution [eq2.43] of a BCS dos (tip) with the Arnold dos (substrate). Than we fit the spectrum varying the ratio d/ξ and adjusting the broadening param-

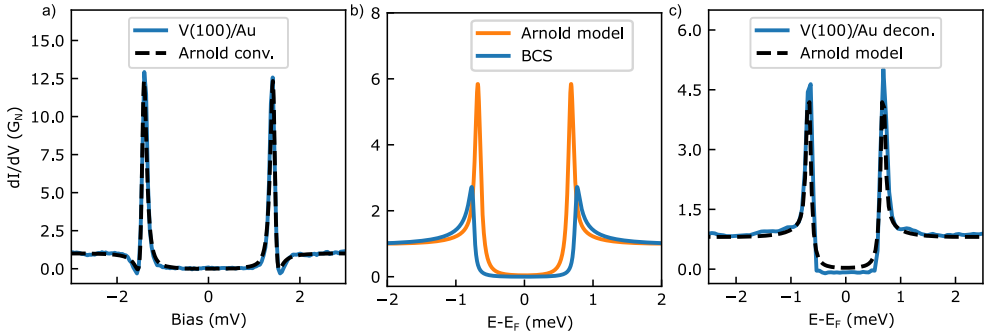

Figure 4.7: Arnold model description and deconvolution of the dGSJ spectrum. a) Fit of the Au/V spectrum with the Arnold model ($\Delta_t = \Delta_s = 0.75$ meV, $d/\xi = 0.0135$, $T = 1.3$ K, $\Gamma_t = 3.0 \cdot 10^{-5}$, $\Gamma_s = 2.2 \cdot 10^{-6}$) convoluted with a BCS density of states (tip). **b)** Components of the fit. **c)** Comparison of the Arnold model with the Au/V deconvoluted spectrum.

eters of tip and sample with a $\Delta = 0.75$ meV for both tip and S part of the sample. We obtain the best fit shown in Fig. 4.7a, with $d/\xi = 0.013$. This means that the actual thickness is 1.3% of the coherence length of the system, the very thin film limit. The tip and sample DOS components of the fit are shown in Fig. 4.7b and the in Fig. 4.7c we compare the deconvoluted spectrum of the sample [Fig. 4.6c] with the calculated one showing the quantitative agreement.

Line profile of a strongly coupled FeTPP-Cl

Most of the FeTPP-Cl molecules investigated behave like the example shown in Fig. 4.3 of the main text. However, some species appear in a different interaction regime. In every case, we can identify the coupling regime by analyzing both the energy shift of the α and B peaks with the tip position over the molecule and the particle-hole asymmetry (as shown in Fig. **??**e.

In Fig. 4.8 we study a FeTPP-Cl molecule in the strong coupling regime and show that this specie appears with protruding pair excitation spectral features. A spectrum on the center of the molecule (Fig. 4.8a appears with sub-gap YSR α peaks lying close to zero energy (detected at Δ_t/e bias, because of the superconducting tip), indicating that it lies very close to the quantum phase transition (QTP) between the two YSR interaction regimes. Accordingly, the molecule shows both A and B peaks outside the superconducting gap with similar intensity.

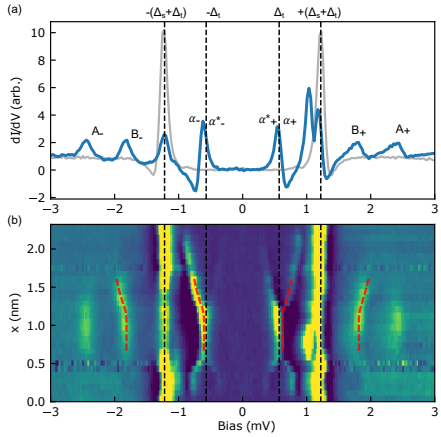

Figure 4.8: Additional exchange tuning line in a strongly coupled molecule. a) Tunneling Spectrum of a 4-fold FeTPP-Cl molecule measured at its center. The α peak is tuned to the quantum critical point of QPT whilst the A and B peaks outside of the gap are clearly distinguishable. **b)** For the same molecule, a line of dI/dV spectra taken along the transversal direction.

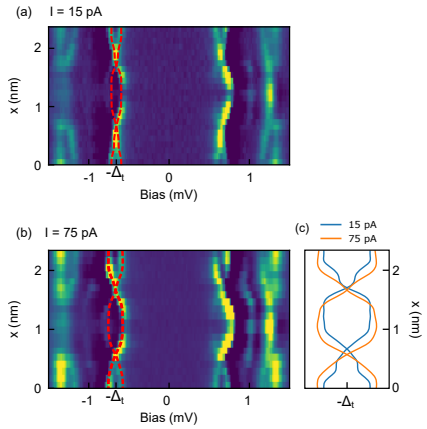

Figure 4.9: Height dependence of the exchange interaction tuning. a-b) Linescan of the molecule presented in Fig. 4.3 of the main text at two set-point current values (V= 3mV I = 15, 75 pA). **c)** The α peak energy shift (dotted traces on the maps), both in the strong and weak coupling, is enhanced by raising the tunneling current.

As shown in Fig. 4.8b, both the sub-gap YSR α peak and the pair excitation peak B shift towards higher energies as the STM tip moves away from the molecule center. The stronger interaction regime explains the strong pair excitation detected in the spectrum.

Dependence of molecule-surface interaction on tip vertical position

The attractive effect induced by the STM tip over the molecule can be slightly controlled via variations of tip proximity to the molecule. In Fig. 4.9 we compare spectral profiles across the molecule in Fig. 4.3 of the manuscript with different junction resistances. The increased interaction with the tip for the higher resistance case leads to larger variations of YSR peaks as the tip is moved across. This dependence on the tip's vertical distance also proves that the observed variations of J are not an intrinsic property of the molecule but are induced by the interaction of the molecule with the STM tip [119].

Dependence of pair excitation amplitude on the exchange interaction J

In Fig. 4.5 of the manuscript we have shown that the pair excitation is a property of the molecule in the strong coupling regime (the Kondo-screened regime). In Fig. 4.10 we plot the amplitudes of the pair excitation peak B, measured at the center of a set of 15 FeTPP-Cl molecules, as a function of the corresponding exchange interaction J. The molecules are those studied in Fig. 4.5a of the manuscript. The

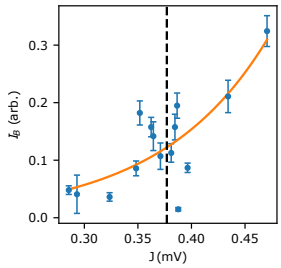

Figure 4.10: Amplitude of the pair excitation as a function of the exchange interaction. For a set of 15 FeTPP-Cl molecules we measured the amplitude of peak B. The solid line is a Boltzmann fit, showing how the peak is more intense in the strong coupling regime.

value of J is obtained in each of them by fitting the position of YSR peaks α with the theoretical model.

The intensity of the pair excitation B is very small in the weak interaction regime (free-spin case). In this regime and at zero temperature, this transition should be zero. The finite temperature of our experiment enables a small excitation probability due to the thermal population of the α YSR state. The pair excitation amplitude increases significantly beyond the QPT, where now the ground state is odd in fermion parity and enables direct excitation of the pair state with a single tunneling electron. We fit the behavior with a Boltzmann distribution obtaining a temperature T = (1.2 ± 0.2) K, that is compatible with the experimental temperature.

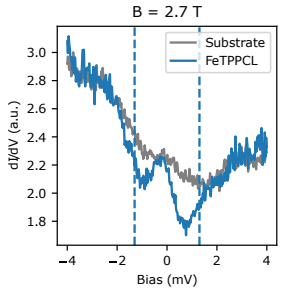

Figure 4.11: Kondo and step excitations without superconductivity. dI/dV spectra of a 4-fold FeTPP-Cl with an applied magnetic field of 2.7 T applied in the direction perpendicular to the substrate. The superconducting gap of the surface and tip is suppressed.

Spectrum of a FeTPP-Cl in the normal state

We quenched the superconducting state of tip and sample with a perpendicular magnetic field of 2.7 T to study the spectral shape of FeTPP-Cl at low energy in the absence of superconductivity. The resulting spectrum (Fig. 4.11) reflects the presence of Kondo-screening interactions and spin excitation, as we also find in the superconducting state. In particular, we observe a step excitation at 1.3mV (dashed line in Fig. 4.11) corresponding to the spin excitation $S_s = 1/2$ to $S_z = 3/2$ (D = 0.65 mV) and a weak Kondo resonance at 0 energy, signature of a ground state with $S_z = 1/2$.

Theoretical model

As mentioned in the main text, we describe the superconductor by using a single-site model which is an extension of the one discussed in Ref. [24]. Including the tip, the Hamiltonian reads:

$$H_{\text{model}} = H_s + H_t + H_{ts},, \tag{4.5}$$

where H_s and H_t describe sample and tip, respectively, and H_{ts} is the tunneling Hamiltonian; H_s is a single site superconductor coupled to a quantum impurity with spin $S = 5/2$:

$$\begin{aligned} H_s &= H_0 + H_M + H_J \\ H_0 &= \Delta_s c_\uparrow^\dagger c_\downarrow^\dagger + \text{h.c.} \\ H_M &= D S_z^2 + E(S_x^2 - S_y^2) \\ H_J &= \sum_{\sigma\sigma'} c_\sigma^\dagger \left[V\delta_{\sigma\sigma'} + J_z S_z s^z_{\sigma,\sigma'} \right. \\ &\qquad \left. + J_\perp \left(S_+ s^-_{\sigma\sigma'} + S_- s^+_{\sigma\sigma'} \right) \right] c_{\sigma'}. \end{aligned} \tag{4.6}$$

Here Δ_s is the strength of the superconducting pairing in the substrate, D and E are the axial and transverse magnetic anisotropy of the molecule, and J_z and $J_\perp$ are the axial and transverse magnetic exchange couplings, and V is the impurity scattering potential. The effects of different terms on the spectrum of the system will be described in the following subsections.

We also treat the Hamiltonian describing the superconducting tip, H_t, as a single-site superconductor:

$$H_t = \Delta_t c_{t\uparrow}^\dagger c_{t\downarrow}^\dagger + \text{h.c.}\ . \tag{4.7}$$

Finally, the tunneling between the tip and sample is described by

$$H_{ts} = \sum_\sigma T_{\sigma\sigma'} c_{t\sigma}^\dagger c_{\sigma'} + \text{h.c.} \tag{4.8}$$

with $T_{\sigma\sigma'} = T_0 + T_1 \boldsymbol{S}\cdot\boldsymbol{\sigma}_{\sigma\sigma'}$, where T_0 is normal tunneling and T_1 is the spin-flip tunneling. Throughout we assume no Josephson current or multiple Andreev reflections between the tip and the sample, as expected in the weak tunneling regime.

The Hamiltonian (4.5) is invariant under time-reversal symmetry (TRS) and commutes with the parity operator of combined the tip+sample system, $P_T = (-1)^{N_T}$, where $N_T = N_t + N_s$ is the total electron number operator. Notice that the tunneling Hamiltonian H_{ts} does not commute with the sample (tip) parity operator $P_s = (-1)^{N_s}$ ($P_t = (-1)^{N_t}$). However, P_s is still a good quantum number when considering the diagonalization of H alone, as we shall do below. Thus, the Hilbert space of the sample can be separated into two parity sectors: even parity with $P_s = 1$ and odd

parity with $P_s = -1$. In addition to TRS and parity, Eq.(4.5) exhibits other symmetries in certain limiting cases. For example, in the limit where the transverse magnetic anisotropic E vanishes, the Hamiltonian is invariant under the Z_2 symmetry that maps $S_{T,z} \to -S_{T,z}$ and interchanges $S_{T,x} \leftrightarrow S_{T,y}$, where $\boldsymbol{S}_T = \boldsymbol{S} + \frac{1}{2} c^\dagger_\sigma \boldsymbol{\sigma}_{\sigma\sigma'} c_{\sigma'}$ is the total spin operator. This symmetry is generated by the rotation $\hat{U} = e^{i\pi S_{T,y}} e^{i\pi S_{T,z}/2}$. In addition, we neglect the scattering potential V in Eq. (4.6). This potential breaks particle-hole symmetry (PHS) and would modify the spectral weights of the peaks as mentioned in the main text. However, it does not modify the overall structure of the spectrum and only adds an additional fitting parameter to the model. Therefore, for the sake of simplicity, it can be taken to be zero, which renders the model invariant under PHS.

Single site Superconductor

To gain some basic understanding of the single-site superconductor model and fix the notations, let us start by ignoring the magnetic molecule entirely:

$$H_s = H_0 = \Delta_s c^\dagger_\uparrow c^\dagger_\downarrow + \text{h.c.}\,. \tag{4.9}$$

The Hilbert space of the above Hamiltonian is a four-dimensional linear space spanned by $\{|2\rangle, |0\rangle, |\uparrow\rangle, |\downarrow\rangle\}$, where $|\sigma = \uparrow, \downarrow\rangle = c^\dagger_\sigma |0\rangle$, $|2\rangle = |\uparrow\downarrow\rangle = c^\dagger_\downarrow c^\dagger_\uparrow |0\rangle$, and $|0\rangle$ is the zero-particle or vacuum state. In this basis, the Hamiltonian takes the following matrix form:

$$H_0 = \begin{pmatrix} 0 & \Delta_s & 0 & 0 \\ \Delta_s & 0 & 0 & 0 \\ 0 & 0 & 0 & 0 \\ 0 & 0 & 0 & 0 \end{pmatrix}. \tag{4.10}$$

Upon diagonalization, the eigenstates are:

$$\left\{ |BCS\rangle = \frac{1}{\sqrt{2}}(|2\rangle + |0\rangle), |\overline{\text{BCS}}\rangle = \frac{1}{\sqrt{2}}(|2\rangle - |0\rangle), |\uparrow\rangle, |\downarrow\rangle \right\}, \tag{4.11}$$

with (eigen-) energies $\{-\Delta_s, \Delta_s, 0, 0\}$, respectively. The eigenstates have well defined parity: $P_s|BCS\rangle = |BCS\rangle$, $P_s|\overline{\text{BCS}}\rangle = |\overline{\text{BCS}}\rangle$, i.e., they are even under parity, whilst $P_s|\sigma\rangle = -|\sigma\rangle$ ($\sigma = \uparrow, \downarrow$), i.e. they are odd under parity.

Fig. 4.12 a) shows the spectrum and the possible transitions between the different states of the sample in the single-site approximation. The even and odd parity states are connected by a single creation/annihilation operator of an electron (or a Bogoliubov quasi-particle, see below). However, the two even-parity states are connected by two electrons/holes or two Bogoliubov operators, i.e. $|\overline{\text{BCS}}\rangle \propto \gamma^\dagger_\uparrow \gamma^\dagger_\downarrow |\text{BCS}\rangle$ (see Sec. 4.6). Note that the tunneling of a single electron from the tip will always change the parity of the sample.

Let us consider now the tunneling between the tip and the sample at zero temperature, when both, the tip and the sample, are in their respective ground states:

$|GS\rangle = \frac{1}{2}(|2\rangle_t + |0\rangle_t)(|2\rangle_s + |0\rangle_s) = |BCS\rangle_t |BCS\rangle_s$. When e.g. a spin up electron tunnels from sample to tip (see Fig. 4.12 a)), we have

$$c^\dagger_{t\uparrow} c_\uparrow |GS\rangle = \frac{1}{2} |\uparrow\rangle_t |\downarrow\rangle_s \ . \tag{4.12}$$

This corresponds to a transition of energy $\Delta_s + \Delta_t$, whilst the process in the opposite direction (from tip to sample) involves an energy $-(\Delta_t + \Delta_s)$. This translates into two peaks at $\pm(\Delta_t + \Delta_s)$ in the tunneling spectrum, which mimic the coherence peaks observed in the tunneling between two s-wave superconductors.

Spin-5/2 impurity with zero exchange coupling

Next, we consider how the excitation of the molecular spin reflects on the tunneling spectra. Since D is a large energy scale, we will first neglect the exchange coupling and set $J_z = J_\perp = 0$. This limit is expected to capture some of the physics on the weak coupling side of the quantum phase transition (QPT, see below) [21, 22]. Now the Hamiltonian of the sample is $H_s = H_0 + H_M$, where the spin Hamiltonian H_M accounts for the intrinsic magnetic anisotropy of the molecular spin:

$$H_M = DS_z^2. \tag{4.13}$$

We assume easy-plane anisotropy ($D > 0$) and, for the sake of simplicity, zero transverse magnetic anisotropy $E = 0$. The effect of the latter will be discussed in the last subsection where the spectrum of full Hamiltonian is described.

Since in this limit, there is no exchange coupling, the Hilbert space of the sample is the tensor product of the Hilbert space of the superconducting site and the molecular spin (see Fig. 4.12 b)). We use the basis $\{(|2\rangle, |0\rangle, |\uparrow\rangle, |\downarrow\rangle) |M\rangle\}$, where M is the eigenvalue of z-projection of the impurity spin, S_z. In the even parity sector $S_{T,z} = S_z = M$, which is half-integer (recall that $S = 5/2$) and therefore, by TRS the eigenstates $\{|\text{BCS}\rangle |M\rangle$ ($|\overline{\text{BCS}}\rangle |M\rangle\}$) with the $S_{T,z} = \pm M$ are Kramers pairs and therefore degenerate in energy. In the odd parity sector, the Z_2 discussed above ensures the same for the eigenstates $|\sigma\rangle |M\rangle$. Since $D > 0$, the ground state is the doublet $S_{T,z}$ in the even parity sector, i.e. $|GS\rangle = |\text{BCS}\rangle |\pm\frac{1}{2}\rangle$. The eigenstates in the odd parity sector describe single (quasi-) particle excitations and, in this limit, have higher energy (see Fig. 4.12).

Let us consider the tunneling of a single electron between the tip and the sample in this limit. The tunneling Hamiltonian, Eq. (4.8), contains a spin-independent and spin-dependent terms with amplitude T_0 and T_1, respectively. Since the tunneling current is second order in the tunneling amplitude, there are three different contributions. The term of order $|T_0|^2$ yields a spectrum identical to the one described in the previous subsection. The term of order $T_0 T_1^*$ and its complex conjugate vanish due to TRS (but they would not in an external magnetic field that breaks TRS). Finally,

the term of order $|T_1|^2$ accounts for the spin-flip processes which we discuss in the following. One of the possible tunneling processes is:

$$\begin{aligned} c^\dagger_{t\downarrow} c_{s\uparrow} S_+ \left|GS\right\rangle &= c^\dagger_{t\downarrow} c_{s\uparrow} S_+ \left[\left|\text{BCS}\right\rangle_t \left|\text{BCS}\right\rangle_s \left|\tfrac{1}{2}\right\rangle\right] \\ &\propto \left|\downarrow\right\rangle_t \left|\downarrow\right\rangle_s \left|\tfrac{3}{2}\right\rangle \ . \end{aligned} \tag{4.14}$$

This process involves an excitation of the molecular spin and costs an energy $\pm(\Delta_s + \Delta_t + 2D)$, the minus sign corresponding to tunneling in the opposite direction (i.e. from tip to sample). Transitions (Fig. 4.12 b)) to higher spin states are enabled by spin pumping [23].

Spin-5/2 impurity with finite exchange coupling

Next, we account for the exchange coupling between the impurity and the substrate in the single site approximation and explain how the parity changing QPT takes place. The sample Hamiltonian is given in Eq. (4.6), where H_J is the exchange term. We begin by investigating the isotropic limit where $J_z = J_\perp = J$ and $D = E = 0$, i.e. $H_M = 0$. The situation is not quite realistic but makes the discussion of the QPT particularly clear.

In the isotropic limit, the total spin of the superconductor plus impurity $\boldsymbol{S}_T$ is conserved. Therefore, the eigenstates are organized into multiplets of $0 \otimes \frac{5}{2} = \frac{5}{2}$, for the even parity sector with $P_s = +1$, and $\frac{1}{2} \otimes \frac{5}{2} = 2 \oplus 3$, for the odd parity sector with $P_s = -1$. In the latter sector, the lowest energy state belongs to the multiplet with the smallest total spin, i.e. $S_T = 2$. Note that, by introducing a new energy scale $J > 0$, the ground state is no longer uniquely determined by Δ_s (see Fig. 4.12 c)). In particular, the parity eigenvalue P_s of the ground state can change from even to odd by tuning J, resulting in a QPT [60, 118]. The transition takes place when the energies of the lowest energy states in the even and odd parity sectors cross as J increases. For a $S = 5/2$ quantum impurity in the isotropic exchange limit the critical value is $J_C = 4\Delta/7$.

Regarding the overall structure of the spectrum, in the even parity sector, the spin of the single-site superconductor is zero and therefore the exchange coupling has no effect. The eigenstates take the form $\{\left|\text{BCS}\right\rangle \left|M\right\rangle, \left|\overline{\text{BCS}}\right\rangle \left|M\right\rangle\}$, i.e, there are two eigenstates per impurity spin $S_z = M$ projection. The states with the same superconductor component are Kramers pairs for $S_z = \pm M$ and therefore degenerate in energy.

On the other hand, in the odd parity sector, the exchange coupling is effective and the total spin of the eigenstates is an integer, as discussed above. In the multiplet with $S_T = 2$, the eigenstate $(\left|\frac{1}{2}\right\rangle \left|\downarrow\right\rangle - \left|-\frac{1}{2}\right\rangle \left|\uparrow\right\rangle)/\sqrt{2}$ with zero $S_{T,z}$ eigenvalue becomes the lowest energy state. Indeed, for $D > 0$ both multiplets of $\boldsymbol{S}_T$ split, resulting in the states with the smallest $S_{T,z}$ eigenvalue *from both multiplets* having the smallest energy. The Z_2 symmetry implies that the eigenstates with the opposite $S_{T,z}$ eigenvalue are degenerate.

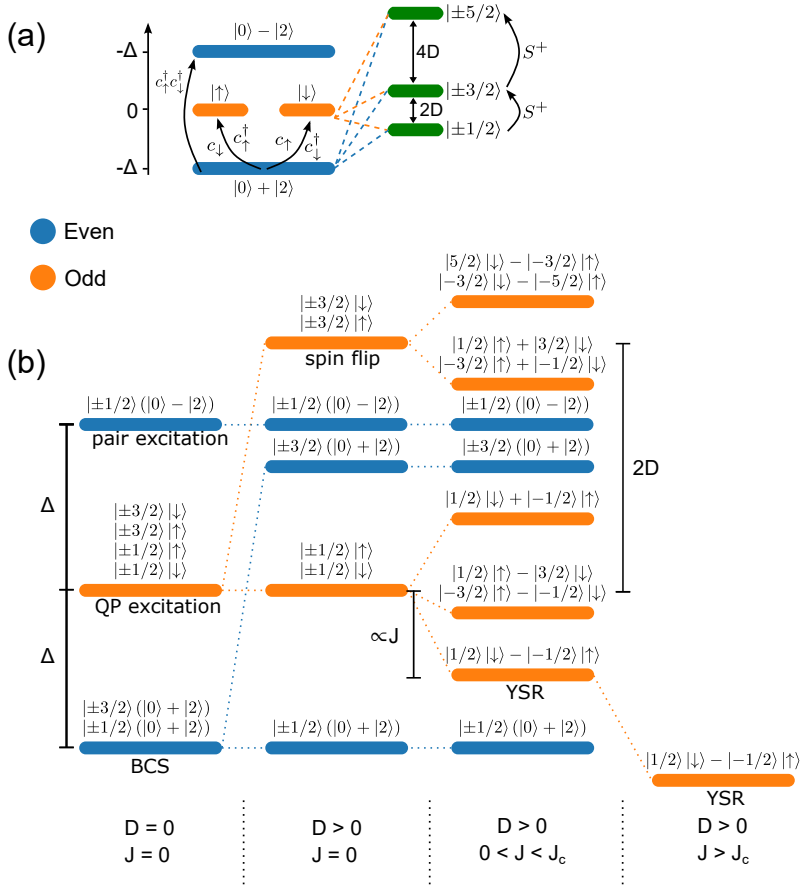

Figure 4.12: Full energy level scheme of a single-site superconductor coupled with a S=5/2 single channel quantum impurity. a) Spectrum of a single-site superconductor with states labeled by fermion parity: even (blue) and odd (orange) parity. When adding a spin $S = 5/2$ quantum impurity with easy-axis magnetic anisotropy D but negligible exchange each eigenvalue split in three components. **b)** Effect of a finite exchange coupling together with axial magnetic anisotropy on eigenvalues and eigenvectors. The parity changing QPT occurs for exchange greater than a critical value. To simplify the notation the coefficients of the linear combinations have been suppressed.

Full Hamiltonian

We now discuss the combined effect of all terms in the model of Eq. (4.6). In Fig. 4.13 we show the evolution of the spectrum as the values of the different couplings are turned on up to values compatible with the experimental ones. The blue and orange lines correspond to the eigenstates with even and odd parity, respectively. The

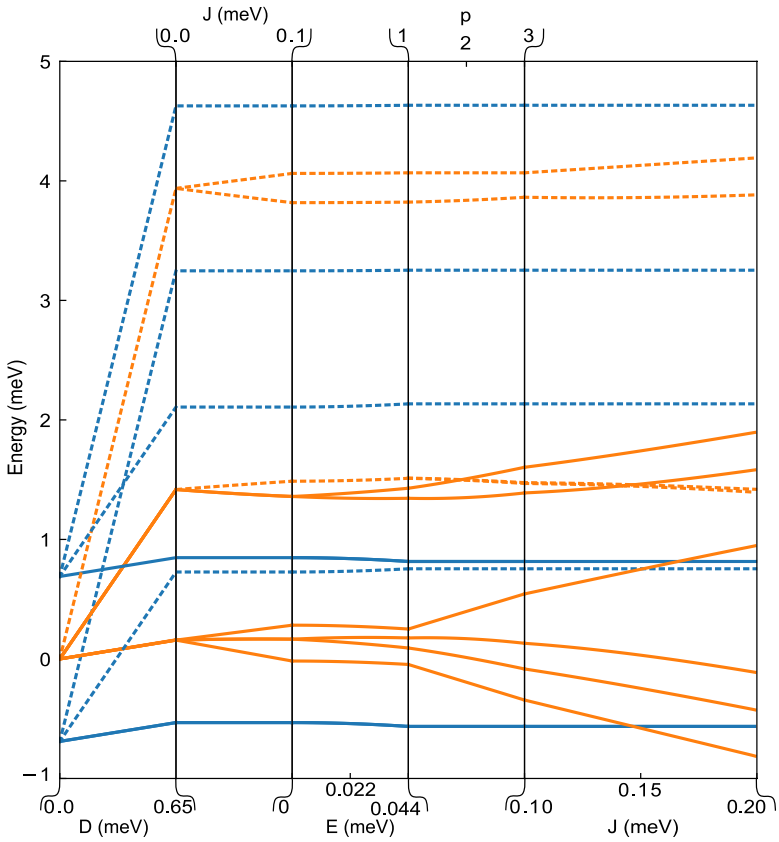

Figure 4.13: Full evolution of even and odd parity eigenvalues of the Hamiltonian. The evolution of the energy levels is plotted as a function of the model parameters: the magnetic anisotropy D, the exchange coupling J, transverse anisotropy E and the ratio of the transverse and longitudinal exchange p couplings. The solid lines are the states reachable by tunneling one electron, while the dotted are prohibited by spin selection rules.

solid lines are the levels reachable by tunneling electron (at 0th order in E) resulting in the terms of order $|T_0|^2$ and $|T_1|^2$ in the tunneling current.

Consistent with the existence of large axial magnetic anisotropy D in the molecular spin, we have assumed an anisotropic exchange coupling where $J_z \neq J_\perp$. We find an optimal value for the ratio $p = J_\perp/J_z = 3$. This value is close to the one obtained by projecting a $S = 5/2$ spin onto the $S = 1/2$ pseudo-spin describing the lowest energy doublet for a quantum impurity with $D > 0$ [149]. However, generally. the anisotropic exchange may result from several different mechanisms [149].

	Symmetries of the system	states # $J < J_C$	states # $J > J_C$
$D = E = J = 0$	TRS, Z_2, FSR$_{sub}$, FSR$_{mol}$	2	1
$D > 0, E = J = 0$	TRS, Z_2, FSR$_{sub}$	6	3
$D, J > 0, E = 0$	TRS, Z_2	6	7
$D, J, E > 0$	TRS	6	12

Table 4.1: Symmetries of the model in various limiting cases. The acronyms and symbols stand for TRS = time reversal symmetry, FSR$_{sub}$ = full spin rotation symmetry for substrate electrons, FSR$_{mol}$ = full spin rotation symmetry for molecular spin, Z_2= 180° rotation around the y-axis followed by a 90° rotation around the z-axis, .

Finally, we briefly discuss the effect of the transverse magnetic anisotropy e). In contrast to the anisotropic exchange, which does not break the Z_2 symmetry, the transverse anisotropy does. This has no effect on even parity states, where, due to the Kramers degeneracy, states with opposite total spin z-projection are degenerate. On the other hand, the breaking of Z_2-symmetry leads to splittings of the energy of odd parity states whose degeneracy is not protected by TRS. This effect accounts for the splitting seen in the γ and β peaks discussed in the main text. As the value of E used is rather small (0.044 meV), we expect a small splitting. A first order perturbation theory calculation for the degenerate states $|\frac{1}{2},\uparrow\rangle - |\frac{3}{2},\downarrow\rangle$ and $|-\frac{1}{2},\downarrow\rangle - |-\frac{3}{2},\uparrow\rangle$ yields a splitting of $\Delta E \sim 3\sqrt{2}E$. Thus, we see that this small E can account for a $\Delta E \sim 0.2$ meV separation between the two peaks.

An alternative explanation of the observed in-gap splitting can be proposed with a two-channel model. This approach increases the number of fitting parameters and complicates the description, justifying our adoption of the simpler one-channel model. The splitting of the remaining states is not substantial and can be ignored in a first approximation. Furthermore, the admixture of the states with different $S_{z,T}$ introduced by E is very small and is not expected to introduce substantial changes to the discussion provided above.

Phenomenology of the pair excitation

Starting from the even-parity BCS ground state (weak coupling) in the zero-bandwidth model:

$$|\text{BCS}\rangle = (u + vc^\dagger_\downarrow c^\dagger_\uparrow)\,|\text{vac}\rangle\,. \tag{4.15}$$

From [152] creation and annihilation operators of quasiparticles excitations are:

$$\begin{aligned}
\gamma^\dagger_\uparrow &= uc^\dagger_\uparrow + vc_\downarrow \\
\gamma^\dagger_\downarrow &= uc^\dagger_\downarrow - vc_\uparrow \\
\gamma_\uparrow &= uc_\uparrow + vc^\dagger_\downarrow \\
\gamma_\downarrow &= uc_\downarrow - vc^\dagger_\uparrow,
\end{aligned} \tag{4.16}$$

The odd parity excited state is obtained by adding a quasiparticle to the BCS state:

$$\begin{aligned} |\text{odd}\rangle &= \gamma_\uparrow^\dagger |\text{BCS}\rangle \\ &= (u^2 c_\uparrow^\dagger + uvc_\uparrow^\dagger c_\downarrow^\dagger c_\uparrow^\dagger - vuc_\downarrow - v^2 c_\downarrow c_\downarrow^\dagger c_\uparrow^\dagger) |\text{vac}\rangle \\ &= (u^2 + v^2) c_\uparrow^\dagger |\text{vac}\rangle \\ &= c_\uparrow^\dagger |\text{vac}\rangle \end{aligned} \tag{4.17}$$

Where we simplified using commutation relations for fermions.

From this state, by single electron tunneling, the system can return to the $|\text{BCS}\rangle$ state annihilating the quasiparticle (YSR excitation):

$$\gamma_\uparrow c_\uparrow^\dagger |\text{vac}\rangle = (u + vc_\downarrow^\dagger c_\uparrow^\dagger) |\text{vac}\rangle = |\text{BCS}\rangle \tag{4.18}$$

or exciting another quasiparticle and reaching the pair excited state:

$$\gamma_\downarrow^\dagger c_\uparrow^\dagger |\text{vac}\rangle = (v - uc_\downarrow^\dagger c_\uparrow^\dagger) |\text{vac}\rangle = |\overline{\text{BCS}}\rangle \tag{4.19}$$

Being $|\text{BCS}\rangle$ the vacuum of quasiparticles, it is annihilated by destruction operator, while $|\overline{\text{BCS}}\rangle$ is not since contains two quasiparticles:

$$\begin{aligned} \gamma_\downarrow |\text{BCS}\rangle &= \gamma_\uparrow |\text{BCS}\rangle = 0 \\ \gamma_\downarrow |\overline{\text{BCS}}\rangle &= c_\uparrow^\dagger |\text{vac}\rangle \\ \gamma_\uparrow |\overline{\text{BCS}}\rangle &= c_\downarrow^\dagger |\text{vac}\rangle \end{aligned} \tag{4.20}$$

5 Tuning the superconducting proximity effect in graphene via Pb islands manipulation

5.1 Introduction

The proximity effect plays an important role in many devices and can be most helpful in the design of novel superconducting quantum systems. At a superconductor (S)-normal metal (N) interface, electrons with energy below the energy gap at the N side are Andreev reflected, generating electron-hole correlated pairs [29] that induce superconductivity in the normal metal. This triggers the appearance of numerous novel effects, such as bound states caused by the coupling of superconductivity and ferromagnetism [153–155], topological states [32, 156, 157] and charge density waves [158–160]. While proximitized systems have been studied mainly through electrical transport measurements [161–165], STM enables the local mapping of the induced superconducting pairing as a function of the lateral distance, facilitating the study of length dependence of pairing, among other properties [166].

Shortly after graphene discovery [167, 168] superconducting correlations in graphene were induced by proximity effect coupling it to a Ti-Al superconductor [169, 170] or by Li-ion intercalation [171]. This encouraged numerous predictions about the interplay between superconductivity and the peculiar electronic structure of graphene [34, 172, 173]. After the first promising results on superconductor-graphene hybrids, progress has been relatively scarce, probably due to a lack of precise control on graphene-superconductor control or local probe that would give access to more direct evidence [35, 174, 175].

In this chapter, we use STM to study the superconducting proximity effect induced by crystalline Pb islands on graphene supported by silicon carbide (SiC). The Pb-graphene interface is optimal since it enables electron transmission to/from graphene, resulting in the proximity effect, as well as the movement of islands on the surface. This allows the construction of Pb-graphene junctions with nm precision and the study of how graphene doping affects the induced superconductivity. The substrate SiC is a polar crystal and graphene is grown either on the Si-terminated face (Gr/SiC0001) or the C-terminate face (Gr/SiC000$\bar{1}$) [176]. Since the graphene of each side has a different effective doping level, the chosen face has a strong influence on the induced proximity effect.

Sections 5.2, 5.3, and 5.4 will cover the study and manipulation of the prox-

imity effect on the C side of SiC, where the Fermi level is at the charge neutrality point. Using the island manipulation technique we study how grain boundaries and Moirè patterns affect the proximity effect and we confine superconductivity in SNS junction-like structures. Then, in section 5.5, we focus on the sub-gap structure arising when approaching the tip very close to graphene, this allows mapping of the Josephson current in a proximitized system and correlates it with the quasiparticle excitation maps. In section 5.6 we study how magnetic field induces in-gap states in confined graphene regions. Finally in section 5.7, we show how the proximity effect on the Si-side of SiC, which is n-doped, is significantly different from that on the C side. The Si side graphene presents a nearly homogeneous gap all over the sample that points to a 2D superconductor due to a collective proximity effect of the phase-coupled array of Pb islands.

5.2 Proximity effect in Gr/SiC000$\bar{1}$ (C-side)

High-temperature annealing of SiC results in multilayer graphene where the mutual twisting angle between the last two or three layers defines a Moirè pattern [177]. The graphene Gr/SiC single crystal was prepared by V.Cherkez, P. Mallet and J-Y. Veuillen in Grenoble following the procedure in [178]. This consists in heating the SiC at 1600°C in an RF furnace in vacuum, and then inducing the graphitization in Ar/H_2 (95%-5%) atmosphere. The samples were then transferred to our STM chamber and cleaned with a 600°C annealing.

A topography map of the bare graphene surface in Fig.s 5.1a shows grain boundaries as bright lines where the orientation of the last graphene layer changes. This results in a change of the Moirè pattern generated from the twisting angle between the first and second layers. The twisting angle θ can be calculated from the Moirè

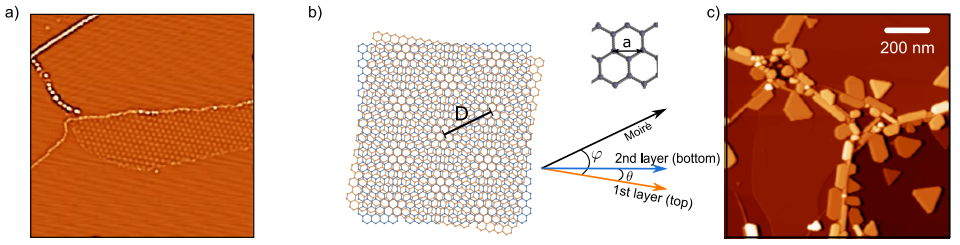

Figure 5.1: Gr/SiC000$\bar{1}$ (C-face) topography and Pb deposition. a) Gr/SiC000$\bar{1}$ topography image with different Moirè pattern domains (V = 1V, I = 100pA). **b)** Moirè pattern raising in twisted bilayer graphene. The Moirè periodicity D depends on the angle θ between the uppermost and second layers. **c)** Gr/SiC000$\bar{1}$ after Pb deposition, Pb islands with 3-fold symmetry are distributed on the surface (V = 1V, I = 100pA).

periodicity D with the formula:

$$\theta = 2\arcsin\left(\frac{a}{2D}\right), \tag{5.1}$$

being $a = 0.246$ nm the lattice constant [Fig. 5.1b]. In the Moirè picture, the main axis of the Moirè superstructure is rotated by φ with respect to the graphene lattice axis, retrieved from the zig-zag graphene direction visible in atomic resolution images. The relationship between θ and φ is:

$$\varphi = 30° - (\theta/2). \tag{5.2}$$

Comparing the zig-zag direction with the Moirè high symmetry direction one can check if the Moirè pattern is created from the overlap of the 1st and 2nd layer or the overlap of the 2nd and 3rd layer. The presence of a Moirè that does not respect eq. 5.2 means that is formed between the 2nd and 3rd graphene layers, with the possible coexistence of two Moirè patterns.

Graphene has different electronic properties depending on the twisting angle, from the semi-metallic, free-like monolayer graphene for a high twisting angle, to an insulating phase showing van Hove singularities for graphene bilayers with small twist angles and flat bands for angles close to the magic angle [179]. The presence of these features around the Fermi level indicates very low doping, with the Fermi level located at the Dirac point. It was demonstrated that in multilayer graphene on SiC, the last graphene layer behaves as free-standing graphene when the twist angle is greater than $\sim 20°$[180].

The Pb evaporation is done with the substrate at room temperature with a rate of $\sim$0.1 A/s, for t = 1-3 min depending on the wanted coverage. In Fig. 5.1c we show an STM image of a Pb-covered graphene region. The islands are 6-fold symmetric with thicknesses ranging from 3.5 to 7.5 nm and lateral sizes from 50 to 300 nm. The dI/dV spectroscopy of islands of these dimensions shows an absolute superconducting gap of $\Delta/e \sim 1.35$ mV that is the same as the bulk one, with the only difference that the double gap structure due to Pb multi-band character [94] is not visible in this case. All the measured spectra are taken with a superconducting tip to enhance the energy resolution. In this chapter, we will frequently show deconvoluted dI/dV data, which retrieve the real density of states of the sample, as explained in section 2.5.

Estimation of the coherence length of proximitized graphene in an SN junction

The coherence length (ξ) of a superconductor is the distance from the SN interface in which the Andreev pairs are coherent. To estimate it we chose the Pb island in Fig. 5.2a, limiting a graphene region without a Moirè pattern of more than 300 nm free of other Pb islands. From the edge of the island, we measured a dI/dV spectra along the dashed line in Fig. 5.2a and show the corresponding spectral map in

Fig. 5.2b and Fig. 5.2c. The proximity-induced gap is characterized by three main features: the position of the coherence peak, the intensity of the coherence peak, and the size of the minigap (or zero energy conductance when an absolute minigap is not present). The zero conductance region between the dashed lines is due to the superconducting tip that shifts the Fermi level of the sample at $\pm\Delta_t$. The dI/dV of Fig. 5.2c shows a non-zero conductance at the sample Fermi level (dashed lines) that indicates the absence of an absolute minigap (finite zero energy conductance) in graphene. This zero-bias conductance [Fig. 5.2d] increases gradually while increasing the distance from the island, reaching the normal metal conductance. At the same

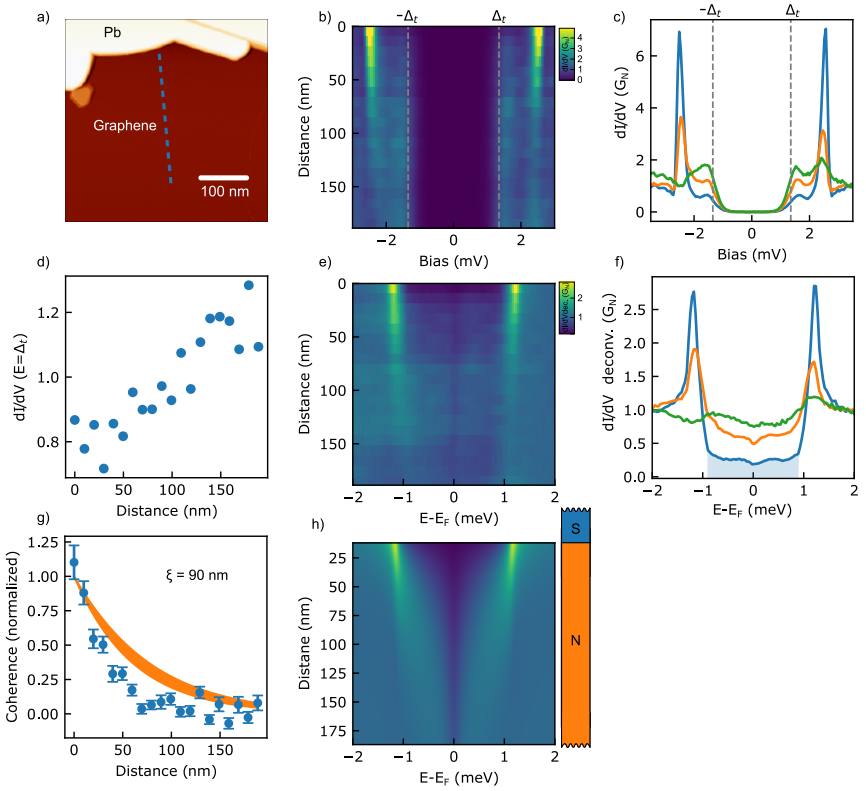

Figure 5.2: Superconducting coherence length in C-side graphene. a) Pb islands that proximitize a graphene region with no additional islands and without a Moirè pattern (V = 1V, I = 100pA). **b)** Line of spectra along the line in a), Δ_t is marked with dashed lines (V = 5 mV, I = 1 nA). **c)** Three selected spectra from b) at 0,50 and 200 nm from the Pb island, where we see the gap fading out. **d)** Coherence extracted from the coherence peak intensity and fitted with an exponential to extract the coherence length of $\xi = 90$ nm. **e)**Deconvolution of b) that shows a flat metallic density of states away from the Pb island. **f)** Extracted spectra from e). **g)** Simulation with Usadel equation by J.C. Cuevas (UAM) of an SN junction with an infinite N part ($\xi = 90$ nm, $\Delta_p = 1.15$ meV).

time the coherence peaks decay in intensity, which we fit with an exponential function [Fig. 5.2g] to estimate a coherence length $\xi \sim 90$ nm. Later in this chapter, the coherence length will be compared with the distance between Pb islands observing modifications of the proximity effect when this is comparable with ξ.

This situation can be described as an SN junction where the normal part extends to infinity. We collaborate with by J.C. Cuevas (Universidad Autónoma de Madrid, UAM) who models this configuration with the Usadel approach (eq. 2.28) to simulate the data. When the N part (d) extends much more than the coherence, the Thouless energy $E_{\mathrm{Th}} = \xi^2\Delta/d^2$ is negligible and, even very close to the Pb island, we do not observe an absolute minigap. This is particularly clear in the deconvoluted data of Figs. 5.2e-f where the shaded region indicates the non-zero in gap conductance. The Usadel simulation assuming the estimated ξ and the proposed SN geometry is reported in Fig. 5.2h, note the nice agreement with the data. In particular, it reproduces both the absence of a minigap and the decay of the quasiparticle peaks.

5.3 Effect of the twist angle in the proximity effect in graphene

As it has been recently observed, twisted layers of graphene induce electron-electron correlations that lead to exotic correlated phases such as superconductivity [181]. A natural question raises, namely if a Moirè pattern can affect the e-e correlations induced by the proximity effect [182, 183]. The investigation of the effect of the Moirè pattern in the proximity effect can give insight into superconductivity in twisted bilayer systems. No theory can currently describe this effect, but it is known that a Moirè pattern can induce spontaneous orbital magnetization in graphene [184, 185], where pseudo-magnetic fields localize electrons in circular orbits [186]. The possibility of moving the Pb islands on the surface allows testing of how superconductivity is induced in different graphene domains, and relating it to the twisting angle of the two uppermost layers, identified by measuring the Moirè pattern periodicity.

In Fig. 5.3a we show the topography of a Pb island that was moved inside a graphene domain with a 6.6° twisting angle between the two upper-most layers (inset). The same island was then moved to an adjacent domain [Fig. 5.3b], where it spontaneously aligns itself with the zig-zag direction of the upper-most graphene layer. In this case, since no Moirè pattern is present, we preclude a high twisting angle between the two upper-most layers, and thus as quasi-free standing top-most graphene layer [179, 180, 187]. The proximity effect induced in these two domains shows a striking difference. We quantify it by taking spectra around the perimeter of the islands as close as possible to the edge. In Fig. 5.3 the average of these spectra is reported and compared for the two regions. In the domain with the Moirè pattern superconductivity is absent, indicating a probably very short coherence length. This is deduced from the weak coherence peak and the absence of an induced gap, with zero-bias conductance of the same magnitude as the normal conductance [Fig. 5.3d].

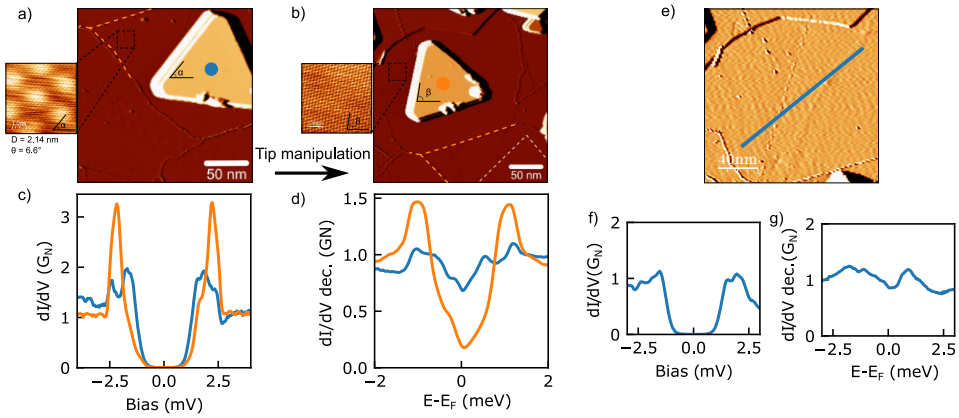

Figure 5.3: Moirè dependence of the proximity effect. a) STM topography of a Pb island on a graphene domain with Moirè pattern (V = 1 V, I = 100 pA), on the left a zoom of the Moirè-atomic resolution (V = 100 mV, I = 100 mA). **b)** The island of **a)** was manipulated with the STM tip to a different graphene domain with no visible moirè pattern (constant I at V = 5 mV). **c-d)** dI/dV spectra (convoluted and de-convoluted) of graphene averaged along the perimeter of the island before and after moving it, showing the opening of the gap (V = 5 mV, I = 500 pA). **e)** Graphene area of a-b) after removal of the Pb island (V = 1 V, I = 100 pA). **f)** Average of the line of spectra along the line in e). **g)** Deconvolution of f) showing that no proximity gap, excluding proximity effect coming from secondary Pb islands (V = 5 mV, I = 500 pA).

After manipulating the islands in the Moirè free area the average intensity of the coherence peaks close to the islands increases drastically and the zero-bias conductance is reduced by the proximity effect. Is important to check that the induced gap is indeed due to the Pb island introduced in the domain and not induced by neighboring islands. This is proved by measuring STS in the same area after the removal of the Pb island [Figs. 5.3e-g]: spectra on the bare graphene domain show indeed neither gap nor coherence peaks.

Summarizing, we find that the proximity effect is strongly dependent on the presence of a Moirè in graphene. Moirè patterns create corrugations in graphene that leads to electron localization, ultimately generating flat bands ($v_F \sim 0$) at the magic angle [188]. Electron localization can enhance the Coulomb repulsion [189] inducing an insulating state that can potentially compete with superconducting correlations suppressing the superconducting proximity effect as observed in this experiment. This experiment calls for a systematic Moirè dependence study, comparing the coherence length with the twist angle on different domains.

Proximity effect across a graphene domain boundary

It is known that the grain boundaries are detrimental to the transport properties [190, 191] being critical for high-temperature superconductors [192, 193]. A proposed

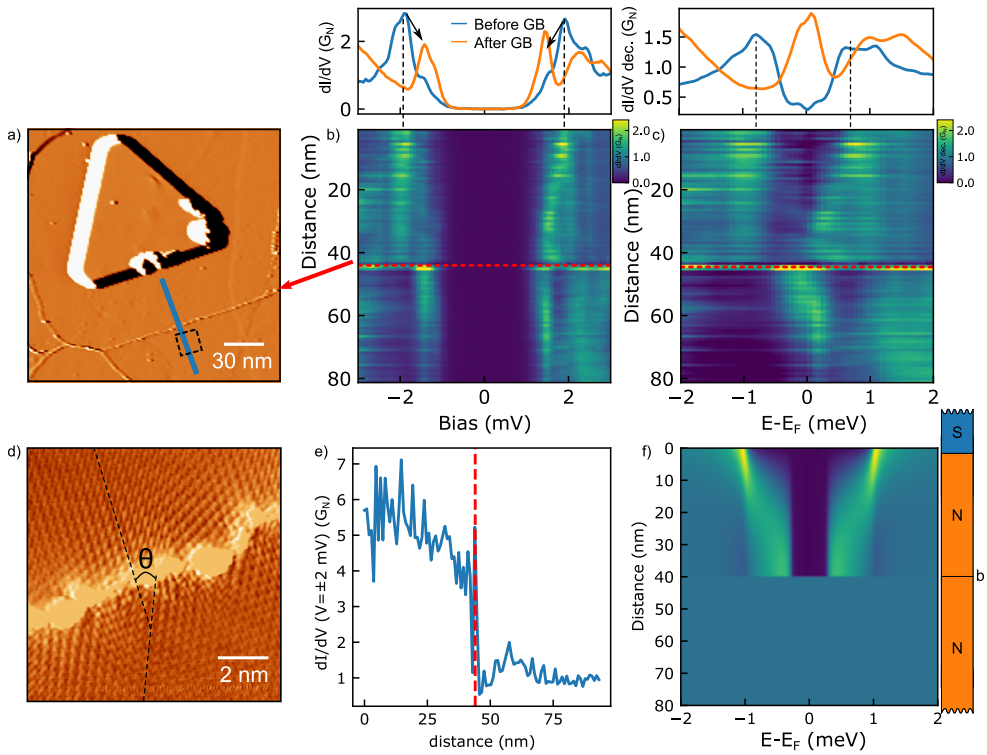

Figure 5.4: Proximitized superconductivity across a grain bounday. **a)** Pb island close to a graphene grain boundary that separates two areas with different twisting angles (see Fig. 5.1 (V = 1 V, I = 100 pA, differentiate filter to visualize both island and grain boundary). **b)** The spectra on top are taken close to the island and after the GB. Below, we report a line of spectra along the blue line in a), where the position of the grain boundary is highlighted (V = 4 mV, I = 400 pA). **c)** Deconvoluted data from b). **d)** Constant current map showing the lattice mismatch of $\theta = 25$ at the grain boundary (constant I at V = 5 mV). **e)** Height of the quasiparticle peak (coherence) going across the grain boundary (red dashed line). **f)** Diffusive Usadel calculation by J.C. Cuevas (UAM) for a superconductor-normal-barrier-normal system (normal probe) where the barrier is perfectly reflective.

microscopic theory treats the GB as regions of a crystal where the current flow has closed loops or flows backward [194] and successfully described experimental data [195]. Local measurements using STM can provide valuable insight into the effect of GB on electronic properties. The C side of Gr/SiC presents areas with different carbon lattice orientations separated by GBs, which can also present different Moirè patterns. Here, we test locally how the superconducting proximity is affected across GB, thus giving information on the variation of electronic properties across the GB. These measurements are done by placing a Pb island close to a GBs separating two

domains (same as presented in the preceding section) with a ≈25° mismatch [Fig. 5.4d] between the graphene lattices, which appears reflected in a change of a Moirè pattern.

Both island and GB are mapped in Fig. 5.4a. STS is recorded along the line that crosses the GB, in Fig. 5.4b the corresponding dI/dV line profile reveals a strong discontinuity of the superconducting gap at the grain boundary. The spectrum before the GB, shows well-defined coherence peaks, marked by dashed lines in the blue spectrum of 5.4b. The intensity of the coherence peaks slightly decays in intensity with the distance from the island and proximity gap closes slightly, visualized in the deconvoluted dI/dV in Fig. 5.4c. These changes are negligible when compared to the crossing of the GB. The coherence peaks are suddenly suppressed, as shown by the line cut of the line profile at the coherence peak energy in Fig. 5.4e where we observe a sharp decrease of coherence at the GB. In the same position the minigap completely closes leaving a peak feature at Δ_t, which in the deconvolution appears as a peak at zero energy.

We describe the experiment with by J.C. Cuevas (UAM) making the limit assumption of the GB acting ideally as a perfect reflective potential barrier. This is obtained by considering an effective SNbN (superconductor-normal-barrier-normal) junction. The calculated density of states at increasing distance from the superconductor [Fig. 5.4f] shows the presence of a minigap that is interrupted abruptly at the boundary. We note that the presence of such a barrier not only naturally impedes the diffusion of correlated Andreev pairs, but acts as a confinement barrier that opens further the minigap in the proximitized region. The microscopic reason for this reflection can be related to a mismatch between k-vectors due to the different graphene orientations. Another possible explanation would be correlated to the presence of the Moirè pattern since in the previous section we saw how this suppresses the coherence.

This approach could be extended for studying electronic scattering across grain boundaries between various kinds of domains, opening for systematic studies of different matching angles and comparison with theory [196]. The coherence drop suggests a high reflectivity of the GB for electrons-hole pairs that are Andreev reflected from the Pb island. The GB interface acting as a mirror could lead to the formation of Andreev-bound states in the case of ballistic transport. In this case, the energy of the bound states inside the superconducting gap in which energy should depend on the island-GB distance.

5.4 Confinement of superconductivity by means of a tunable SNS junction

We studied how a single Pb island induces superconductivity in graphene. The controlled manipulation of Pb islands opens the possibility of building structures

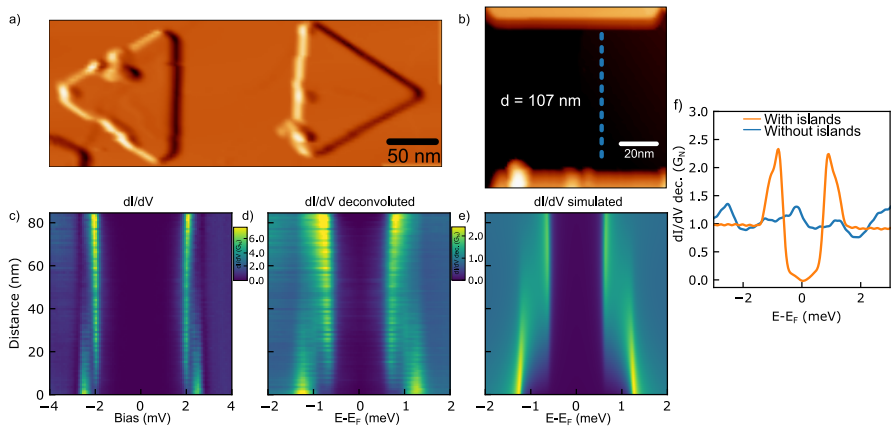

Figure 5.5: Asymmetric gap SNS junction conductance. a) SNS junction made of 2 Pb islands (V = 1V, I = 100pA, differentiate filter). **b)** Zoom in the junction between the two islands, d is the gap between the Pb edges. **c)** Line of spectra along the blue dotted line in b) showing a 2 peaks structure (V = 6 mV, I = 600pA). **d)** Deconvolution of c) **e)** Simulation using Usadel equation by J.C. Cuevas (UAM) considering $\Delta_{G1} = 1.17 \pm 0.02$ mV, $\Delta_{G2} = 0.77 \pm 0.02$ mV, $\xi = 76.4$ nm. **f)** deconvoluted dI/dV spectra with and without the Pb island to show the absence of spurious superconductivity from additional islands (subsequent stage of manipulation Fig. 5.21c).

with more than one island and investigating S-graphene-S hybrid structures, with tunable size. The simplest structure is when two triangular islands are brought close with parallel edges that we will refer to as a resonator. In this case, the proximitized graphene is limited by two superconductors in one direction and modeling an SNS junction. We fabricated this geometry using two islands of similar size [Fig. 5.5a], creating what we refer to as a resonator. In Fig. 5.5c we show the measured dI/dV spectral line profile measured in the region enclosed by the two islands, along a line perpendicular to both islands for the initial separation of 107 nm. The spectrum is characterized by two sets of coherence peaks that decay from each respective island. The dI/dV shows that the induced gap is different close to each island and, therefore, the system is an asymmetric S_1NS_2 junction. In Fig. 5.5f we compare the dI/dV in the resonator region before and after the complete removal of the Pb islands. This is an important check to ensure that the observed signals are indeed caused by the analyzed Pb islands.

To describe this asymmetric junction we do a simple assumption, that the two islands are inducing a different gap in the graphene. This could be explained by a different interface configuration. In-fact the reflection coefficient of the island-graphene interface can reduce the gap continuously down to zero energy for perfect reflectivity (no Andreev reflection) [64]. Therefore the labels 1 and 2 in S_1NS_2 refer to the proximitized region below the islands. With the help of by J.C. Cuevas (UAM) the behavior in a linear SNS junction model with the Usadel equations, i.e. assuming diffusive promiximity effect. We use as input parameter $d = 107$ nm and the values

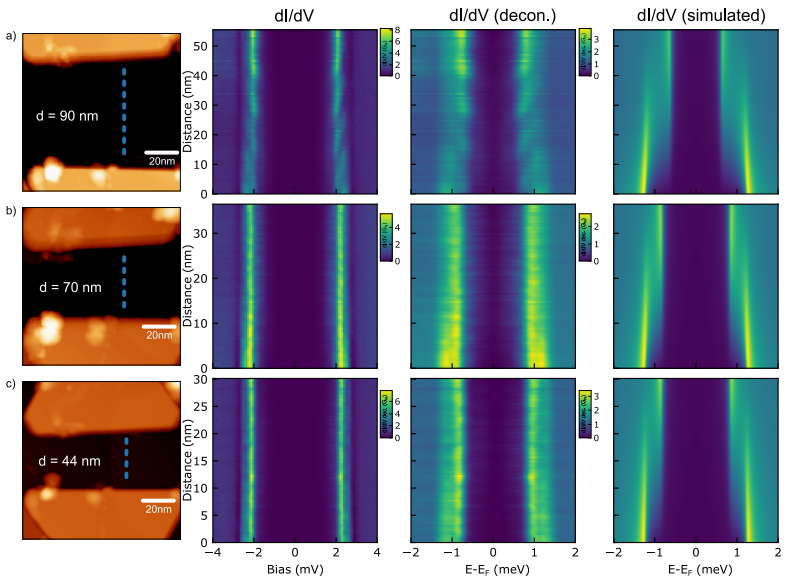

Figure 5.6: Tuning of the SNS junction moving lower island. a-b) The graphs from left to right; STM topography of two Pb islands that enclose a graphene region (V = 1 V, I = 100 pA), the bottom island is moved to tune the spatial gap. STS line of spectra along the lines in the topography maps, note the oscillations and the homogeneity of the d=44 nm configuration (V = 6 mV, I = 600 pA). Deconvoluted dI/dV. dI/dV simulations of the SNS junctions using Usadel equations by J.C. Cuevas (UAM) with $\Delta_{G1} = 1.17 \pm 0.02$ meV, $\Delta_{G2} = 0.77 \pm 0.02$ meV, $\xi = 76.4$ nm and using the experimental junction lengths.

of the gaps $\Delta_1 = 1.17 \pm 0.02$ meV and $\Delta_2 = 0.77 \pm 0.02$ meV, adjusted in the simulation changing the island-substrate reflection coefficients. The simulation in Fig. 5.5e reproduces the two coherence peaks at different energy, that decay closing partially the gap towards the center of the structure. This behavior reproduces quantitatively the experimental data and so demonstrate that the coherence length estimated previously plays a fundamental role. Moreover, this suggests that the resonator is in a diffusive limit, in this case, probably because the separation between the islands is bigger than the coherence length.

To explore the dependence of the LDOS in the SNS resonator with the island separation, we studied the evolution of dI/dV line spectra in the proximitized graphene between the islands as we reduced their separation using the island manipulation technique. We pushed one Pb island towards the other [Figs. 5.21a-c] to reduce the length of the normal region d of the SNS junction. The spectral line profiles in the junction show, first, the appearance of oscillations at $d \sim \xi$. When the junction is closed further the two distinct gaps disappear from the spectral maps and, instead,

we observe one single excitation with energy $\Delta_{G3} = 0.84 \pm 0.02$ meV , i.e. between the two previous gap values. This single gap configuration persist for smaller separations $d \sim 44$ nm [Fig. 5.21c] giving a single gap spectrum along the junction.

In Fig. 5.21 we report diffusive model calculations for d = 90,70 and 44 nm. The diffusive framework does not predict dI/dV oscillations and fails describe quantitatively the line-profiles. When the dimensions of the SNS junction become comparable with the mean-free path a transition to a more ballistic-like type of transport is expected, where the confinement geometry of the system plays an important role. We can calculate the diffusive mean free path with:

$$l = \frac{2\Delta\xi^2}{\hbar v_F}, \tag{5.3}$$

where ξ is the diffusive coherence length, $v_F = 1 \cdot 10^6$ m/s is the Fermi velocity and $\Delta = 1.35$ meV is the superconducting gap of Pb. With ξ = 76.5 nm we estimate a mean free path $l = 24$ nm that starts to be comparable with the small resonator size.

Ballistic transport in the long junction regime is theoretically characterized by the presence of multiple Andreev-bound states. In the small junction regime, ballistic and diffusive transport give very similar spectral features, making it hard to discern between the two regimes. In our experiment, we observe a homogenization of the SNS density of state when the junction size is reduced. This, together with the deviation from the diffusive Usadel simulation, could be the onset of a transition to a ballistic system.

5.5 Sub-harmonic excitations structure in proximitized graphene

The coherence peaks at the border of the absolute gap are the main spectroscopic features of a superconductor-insulator-superconductor (SIS) junction. These consist of the creation of a quasiparticle on both sides of the junction with a total charge transfer of $1e$ [135]. When the tunneling conductance increases, as the tip approach, a well-established sub-structure of in-gap states emerges due to multiple Andreev reflections processes (MARs) [197, 198] and Josephson tunneling [65, 134]. The Josephson tunneling consists of the tunneling of Cooper pairs at zero voltage between two superconductors [65]. This is characterized by a zero net current at zero bias, with a negative current peak followed by a positive current peak near zero bias conductance [134, 199]. This appears as a zero energy peak in the dI/dV spectrum [200, 201].

The MARs sub-harmonic structure appears in the gap with peaks at energy $2\Delta/n$ (n=2,3,...) in the case of a tunnel junction that connects two superconductors with the same gap. These processes are multiple reflections of order $n-1$, involving an increasing number of Andreev reflections (AR). The situation is more complex when the two superconducting leads have a different gap as studied by Ternes et al.

[202]. The excitation mechanisms of such an asymmetric junction is reproduced in Fig. 5.7 from ref. [202], and involves processes where one AR (first order) or two ARs (second order) occurs. We label the different gaps of the leads as Δ_t, the tip gap, and Δ_p the proximity induced gap, that is always lower than the Pb tip gap. The onset for first-order MARs is when either Δ_t or Δ_p gap onsets are aligned with the respective Fermi levels. Based on the Δ_p/Δ_t ratio, two different regimes are distinguished. When $\Delta_p/\Delta_t > 0.5$ the dominant second order process is $(\Delta_t + \Delta_p)/3$. When $\Delta_p/\Delta_t < 0.5$ the second order process $\Delta_t - \Delta_p$ dominates. This latter process is peculiar since can only be visualized in a very asymmetric SNS junction, condition realized in the next subsection for a Pb island corral.

In a proximity system, the gap of the sample is naturally different from the tip gap, since it is usually lower than the bulk superconducting gap. The AR involved in MARs processes occurs between the superconducting tip and the normal sample, which in our experiment is proximitized graphene. Phenomenologically, the potential drop occurs in the vacuum between the tip and the sample thanks to electron-hole mixing, needed to convert an electron into a hole (AR). To our knowledge, no existing theory describes the MARs in a proximitized metal away from the SN interface. The first possible scenario is that the reflection does not occur at the normal interface but at the island-graphene one, instead. This, though, would result in a symmetric Pb-Pb junction with peaks at $2\Delta/n$. A second scenario is the reflection occurring at the graphene-vacuum-tip interface, here we would have the MARs structure of an asymmetric junction as shown in Fig. 5.7. This would imply that the proximity-induced correlations can favor electron-hole mixing far away from the SN interface.

In this section, we present two experiments where we measure proximitized graphene in high conductance regimes with a superconducting tip. In the two systems, graphene has different induced gap values leading to different second-order MARs signals. In the first part, we investigate the sub-harmonic structure in proximitized graphene, identifying the MARs processes through the change of the proximity gap induced by tip-approach. In the second part, we study a triangular region of graphene enclosed by three Pb islands, where the quasiparticle spatial structure influences the Josephson current distribution.

Josephson current and multiple Andreev reflections in proximitized graphene

We perform point-spectroscopy decreasing the tip-sample distance to visualize MARs processes. We do this on a free-standing-like graphene (no Moirè) area, in a point 15 nm away from the Pb island on the right side of the topography in Fig. 5.8a. In the dI/dV spectrum of Fig. 5.8b, we observe the proximity-induced gap at V_p^R (where R stands for right island) and we see three in-gap features: the MAR V_{ar1}^R, V_{ar2}^R, and the Josephson peak at zero energy. To rationalize the origin of the sub gap peaks, we model this system as an asymmetric junction, where we expect the processes depicted in Fig. 5.7. The superconducting tip has a gap parameter $\Delta_t \sim 1.35$ meV and the proximity gap, obtained by subtracting the tip gap from the

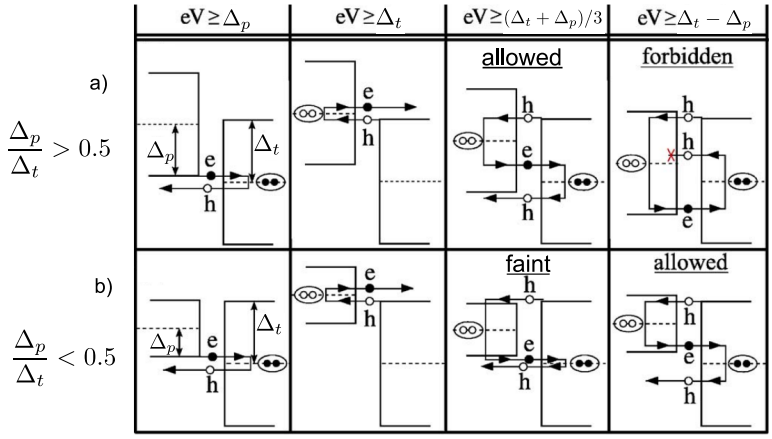

Figure 5.7: Multiple Andreev reflections in asymmetric junctions. We adapt from [202] the 1st and 2nd-order MARs processes scheme in an asymmetric SIS' tunnel junction. We adopt the notation Δ_t for the tip gap and Δ_p for the proximity gap, with always $\Delta_t > \Delta_p$. **a)** Three MARs processes are expected in the regime $\Delta_t/\Delta_p > 0.5$. **b)** Four MARs processes are expected in the regime $\Delta_t/\Delta_p < 0.5$, with the gap sum $(\Delta_t + \Delta_p)/3$ process expected to be faint [202].

position of the proximity gap in graphene, amounts to $\Delta_p = 0.8 \pm 0.02$ meV. The peak V_{ar1}^R lies at the energy of Δ_t, thus being the 1st order MAR related to the tip gap. The peak V_{ar2}^R appears at 0.8 ± 0.02 mV coinciding with the other 1st order MAR at Δ_p. From this deduce that in this experiment we are in the regime $\Delta_t/\Delta_p > 0.5$, resulting in the MAR $(\Delta_t + \Delta_p)/3$ as the dominant 2nd order process.

To study the tip height dependence of the sub gap structure we report a series of spectra approaching the tip [Fig. 5.8b], where the resistance of the tunnel junction decreases from 60 kΩ to 12 kΩ. In Fig. 5.8d we report the relative energy positions of the coherence and sub-gap peaks obtained from a Gaussian fit. The energies of the peaks V_p^R and V_{ar1}^R are not dependent on the tip-sample distance. Differently, the inner V_{ar2}^R peak shifts at lower energy while approaching the tip, this is not expected since this process should scale with Δ_p, that is independent from the tip height (constant V_p^R). Instead, we consider that the shift is caused by the gradual appearance of the mentioned second order MAR which is expected to appear at $(\Delta_t + \Delta_p)/3$. In the experiment we do not see the appearance of an additional peak, but instead a shift in the total contribution that can be caused by the gradual appearance second-order process. To illustrate this we simulate the MAR at Δ_p and a growing contribution of $(\Delta_t + \Delta_p)/3$, each represented by a Gaussian function with center and width extracted by fitting the experimental signals. The sum of the two contributions indeed results in a broader peak which maximum shifts in energy as observed in the exper-

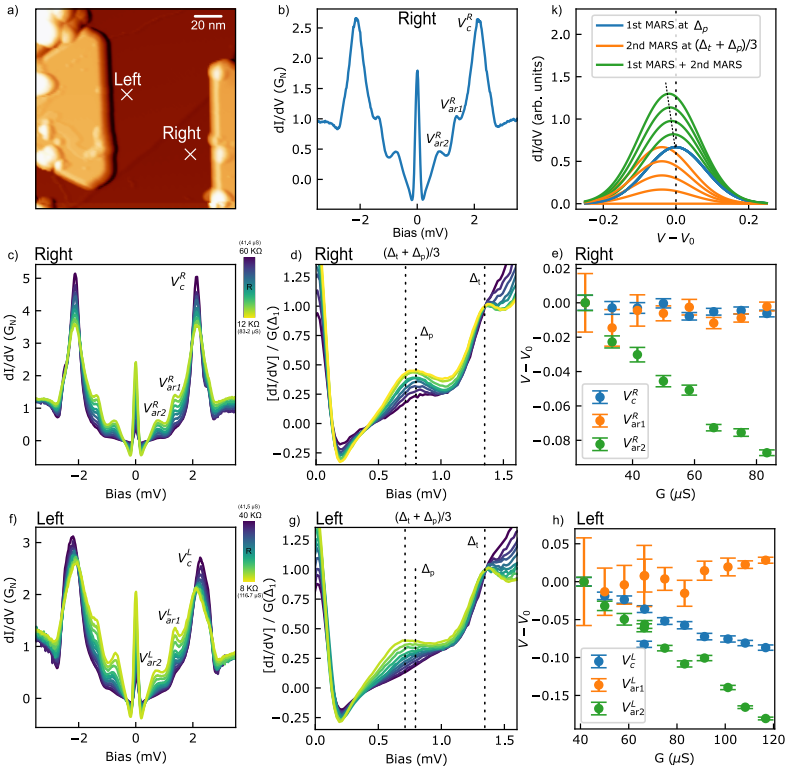

Figure 5.8: Height dependent spectroscopy on proximitized graphene. a) Topography map of two Pb islands, named Left and Right islands in the text (V = 1 V, I = 100 pA). **b)** dI/dV spectroscopy at high conductance close to the Right island of a) where we see three main features: that we label V_p^R, V_{ar1}^R, V_{ar2}^R (V = 6 mV, I = 700 nA). **c)** Point spectroscopy approaching the tip to graphene close to Right island in a) (V = 6 mV, I = 150-500 nA). **d)** Zoom of the V_{ar1}^R, V_{ar2}^R features in c) where the expected MARs processes are highlighted with by the dashed lines. The dI/dV is normalized to the Δ_t value to show the evolution of Δ_p. **e)** Energy position of V_p^R, V_{ar1}^R, V_{ar2}^R increasing the conductance G=1/R with respect to their initial energy values, extracted with a Gaussian fit. **f)** Analogous set as in c) but close to the Left island in a) (V = 6 mV, I = 250-700 nA).**g)** Zoom of f) on the MARs processes (analogous to panel d), **h)** Energy positions of V_p^L, V_{ar1}^L, V_{ar2}^L increasing the conductance, extracted with a Gaussian fit. **k)** Simulation of the two processes at Δ_p and $(\Delta_t + \Delta_p)/3$, showing the energy shift to the total contribution due to the appearance of the 2nd order MAR.

iment. At the lowest resistance the final maximum lies between the energies of the two MARs processes [Fig. 5.8c], confirming the assignation.

In Figs. 5.8f-h we show an analogous dataset presented before, collected close to the island on the left of Fig. 5.8a. Here, we also observe similar MARs signals V_{ar1}^L

Peak	Right ($\mu V/\mu S$)	Left ($\mu V/\mu S$)
V_p	0.09 ± 0.08	1.15 ± 0.14
V_{ar1}	0.007 ± 0.2	-0.45 ± 0.28
V_{ar2}	1.43 ± 0.18	2.28 ± 0.2

Table 5.1: Shift ratio of the states reported in Figs. 5.8e-h for the right and left islands calculated with a linear fit.

and V^L_{ar2} but now, we detect a notable shift of the proximity gap (V^L_p). It is interesting to correlate the shift of V^L_p with the MARs. The peak V^L_p shifts with a rate of 1.15 μV/μS and the V^L_{ar2} peak with a greater rate of 2.28μV/μS [Fig. 5.8g]. This suggests that the shift observed in Fig. 5.8d, due to the appearance of the 2nd order MAR is still present. The higher shifting rate of this second measurement is due to the shift of V^L_p, which affects both MARs processes Δ_p and $(\Delta_t + \Delta_p)/3$. These shifts confirm the nature of the V^L_{ar2} sub-gap resonance as an AR process involving the proximity gap and, therefore, the existence of correlated pairs. Finally, the fact that peak V^L_{ar1} does not shift confirms its assignment to the MARs scaling with Δ_t, since the tip gap does not depend on the junction resistance.

In conclusion, we observed MARs processes in proximitized graphene. We assign each signal to MARs processes occurring in an asymmetric junction by studying how the coherence peak shift affects their energy. The presence of MARs in the graphene-vacuum-tip interface shows that the proximity effect in graphene not only consists of leaking correlated pairs but additionally provides the finite pairing potential needed to mix electron and hole states far from the Pb-graphene interface. This stimulates the study of how Andreev-bound states can interplay with the MARs processes, in the case of a ballistic junction.

Mapping quasiparticle excitation and Josephson current in a superconducting corral

In the previous section, we presented the point spectroscopy properties of proximitized graphene where we found the presence of multiple Andreev reflections and a supercurrent. In this section, we study the same phenomena in a more defined proximitized region where we confine superconductivity in a corral-like structure. In the confined region we find a rich spectrum of quasiparticle excitations, Andreev, and Josephson processes.

The transport properties of an SNS junction [Fig. 5.9a] can be diffusive or ballistic depending on the mean-free path and junction dimensions. In the small SNS junction limit, it is not easy to disentangle between the two behaviors. In fact, both a diffusive Usadel approach and a ballistic Bogoliubov de Genens (BDG) approach can describe the density of states. In Fig. 5.9b we show the calculated density of states along the normal region of a diffusive SNS junction done by J.C. Cuevas. The

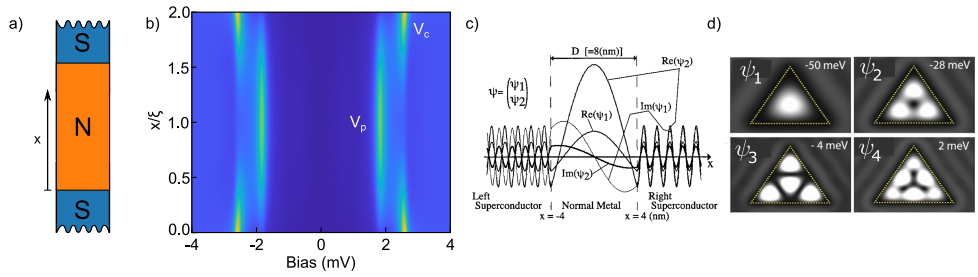

Figure 5.9: Local DOS in an SNS junction in the diffusive and ballistic regimes. a) Scheme of an SNS junction with infinite S leads. **b)** Density of states obtained with the diffusive Usadel model along the N part of an SNS junction, calculated by J.C. Cuevas [205]. **c)** Wavefunction of the Andreev bound states in a ballistic SNS junction, calculated with a Green function approach, adapted from [203]. **d)** Electronic Andreev eigenmodes of a triangular normal region embedded in a superconductor, calculated with Green functions, adapted from [204].

LDOS map shows the minigap onset as a peak in the center of the junction, while the bulk superconductor quasiparticle peak penetrates in the normal region for a distance in the order of the coherence length. In a ballistic case, as shown in section 2.3, the sub-gap structure is discretized and the wavefunction is expected to show multiple eigenmodes that reflect quasiparticle interference in the structure [68, 70]. This regime has been simulated by Nakayama who solved the BDG equations for the 1D problem. He obtained the spatial distribution of wave function amplitude for the discrete set of confined Andreev bound states and found that, for example, the first eigenmode has a maximum in the center reproduced in Fig. 5.9c from [203]. The geometry of the confinement determines the spatial distribution of the eigenmodes. For example, for the case of a confining triangular structure of a normal metal embedded inside a superconductor, Stavropoulos et al. obtained the distribution of the Andreev states shown in Fig. 5.9d, which resembles states of a triangular quantum box [204].

A conventional LT-STM can be used to map the Josephson current (or Josephson conductance) mapping spectroscopy at zero energy. The mapping of the Josephson current is related to the Cooper pair density in a superconductor and mapping the spatial distribution of its amplitude with STM has provided insight into the field of unconventional superconductors [206–209]. In conventional superconductors like Pb, the very high phase stiffness and the high coherence length results in a spatially homogeneous pairing density [210]. Instead, Cho et. al. in [210] observed a strong spatial modulation of the Josephson peak in Iron-based superconductors and they found a strong correlation with the height of the coherence peak. The Josephson maps show spatial modulations with characteristic lengths comparable with the coherence length (size of Cooper pairs), which is interpreted as an intrinsic superfluid inhomogeneity.

Here, we study a confined Pb island system on graphene mapping the coherence peaks and the multiple Andreev reflections (MARs). We find that the confinement induces a spatially modulated quasiparticle excitation that is strongly correlated with the Cooper pair density visualized through Josephson peak mapping.

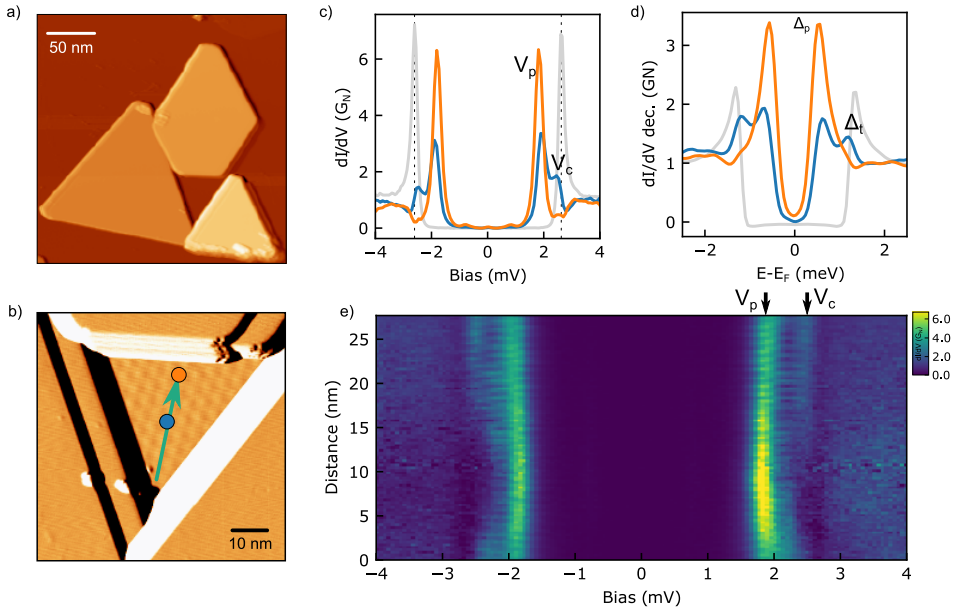

Figure 5.10: Proximitized graphene in a triangular Pb corral. a) Topography image of three Pb islands forming a corral that encloses a triangular graphene region (V = 1V, I = 100 pA). **b)** Zoom in on the enclosed region, Moirè pattern explained in the text. **c)** Spectra in the border (blue) and in the center (orange) of the region in b), we label the two signals V_p and V_c (V = 5 mV, I = 500 pA). **d)** Deconvolution of the spectrum in c). **e)** Line of spectra along the green line in b) showing the distribution of the two signals highlighted with the arrows.

Through the manipulation of the Pb islands, we can form closed structures that we refer to in the following as corrals. In Fig. 5.10a we show a corral enclosing a triangular region of graphene. The zoom-in of Fig. 5.10b shows a Moirè pattern formed between the second and third graphene layers. The topmost layer is thus free-standing like graphene. The spectrum inside the corral in Fig. 5.10c and the deconvolution in Fig. 5.10d shows a double peak structure which component we will refer to as peaks V_c and V_p. The first lies close to the Pb bulk coherence peak and has a larger amplitude close to the islands, the latter is more prominent in the center of the corral. This is shown in the line of spectra of Fig. 5.10e, where V_p dominates over the center of the corral, while V_c extends from the edge of the Pb islands, disappearing in the center.

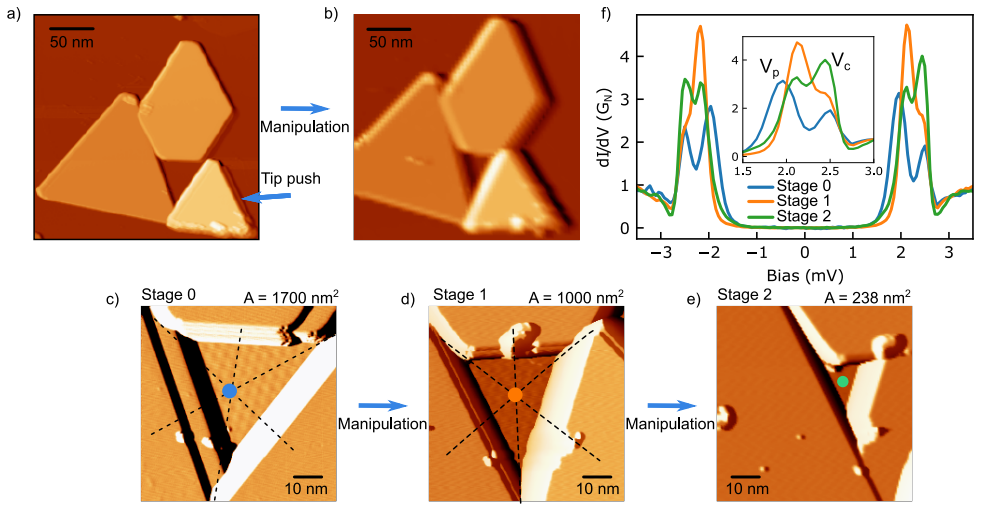

Figure 5.11: Formation of a triangular corral. a) Corral formed by bringing in proximity three Pb islands of different size. The triangular region between them is not fully enclosed by Pb islands. **b)** Corral closed after manipulation of the island in a) as indicated with an arrow. This process closed completely the corral. **c-e)** Three manipulation stages of the corral. Three area of the three corrals amounts to where the average triangle heights of the regions are h = 60,45,20 nm. **f)** Spectra in the center of the corral in the various stages show a shift of the inner component V_p (V = 4 mV, I = 400 pA, the tip gap does not change between the manipulation stages).

To investigate the nature of the two peaks we modified the corral size by moving one of the islands towards the corral center as shown in Figs. 5.11a-b. In this manner, we manipulate the corral in three stages shown in Figs. 5.12c-d-e and measure dI/dV spectroscopy in the center. In Fig. 5.11f we show as the peak at V_c remains at the same bias and increases in intensity upon closing the corral. This is in line with the identification of V_c as related to Andreev processes to the bulk Pb gap. The peak V_p interestingly shifts at higher energy when the size of the corral reduces. This behavior is expected in proximitized systems because the Thouless energy depends on the inverse of the junction dimension $E_{\mathrm{Th}} = \hbar D/d^2$. The last manipulation step does not produce any change in V_p since most probably the corral size is already below the coherence length.

Focusing on the largest stage of the corral, we spatially map the dI/dV inside the enclosed graphene region by measuring a squared 64x64 grid of spectra. This grid cannot cover the whole graphene region [red dashed line Fig. 5.12a] due to the tip-shading effect, however importantly includes the center of the corral. The reference spectra for the outer and inner parts are in Fig. 5.12b, the significant energies are the inner quasiparticle peak V_p that ranges from 1.90 ± 0.05 mV (center) to 2.00 ± 0.05 mV

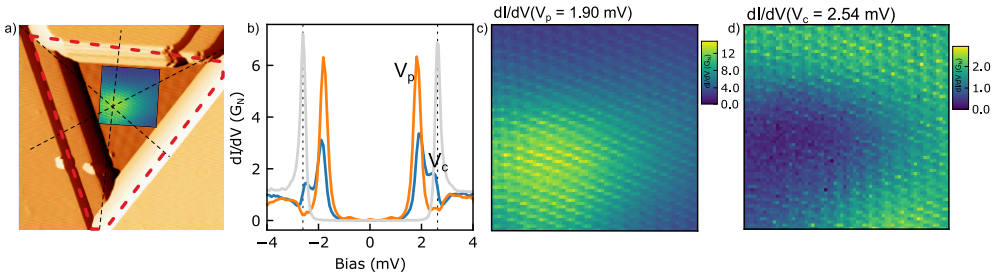

Figure 5.12: Spatial distribution of the two corral resonances. **a)** The enclosed graphene region of the corral. We mark in red the real corral size, and indicate with black dashed lines the center of the corral.**b)** dI/dV spectra in the center and in the edge of the corral, showing the minigap V_p and the coherence peaks V_c. **c)** dI/dV map extracted from a spectral grid at 1.90 mV showing the spatial distribution of the minigap edge peak V_p (V = 6 mV, I = 1.15 nA). **d)** Another grid cut at 2.54 mV showing the coherence peak V_c spatial distribution.

(side) and $V_c = 2.54 \pm 0.05$ mV. We report the corresponding dI/dV maps extracted from the grids in Fig. 5.12c-d and we see that the V_p intensity maximum is located in the center of the corral, while the coherence component V_c is located in the outer part of the corral. If we compare this scenario to the theoretical picture of Fig. 5.9, it matches both the diffusive and ballistic regimes. In the diffusive regime, the V peak corresponds with the minigap edge and V_c with the coherence peak. In the ballistic regime, V_p and V_c correspond to confinement-induced Andreev bound states in the corral, having inverse spatial distributions [Fig. 5.9d].

The Josephson peak and the MARs processes can be seen when the tip is brought closer to graphene. In Figs. 5.13a-c, we show dI/dV point spectroscopy in the corral center, where the tip is approached at resistance (R) from 1.27 MΩ to 0.23 MΩ. In Fig. 5.13c we report a zoom on the sub-harmonic conductance, where we see three prominent features: the Josephson tunneling peak at zero bias and an Andreev reflection signature at $\pm V_{ar} \sim 0.8 \pm 0.05$ mV. In Fig. 5.13d we report the energy position in the function of the conductance, where we see that V_{ar} shifts at lower energies while approaching the tip while the V_p signal shifts at higher energies, with the same rate.

Like in the previous section, we can rationalize the observed signals using the asymmetric SNS junction model described in [202]. This describes the sub-gap harmonic structure of a junction between superconducting leads with different gaps Δ_t (tip gap) and Δ_p (proximity-induced gap). Differently from the previous section, here we are in the regime of $\Delta_p/\Delta_t < 0.5$. Therefore the expected processes are 1st order MAR at Δ_t, Δ_p, observed in the last section, only a faint contribution of $(\Delta_t + \Delta_p)/3$ and the peculiar 2nd order MAR at $\Delta_t - \Delta_p$, that was forbidden in the previous section experiment.

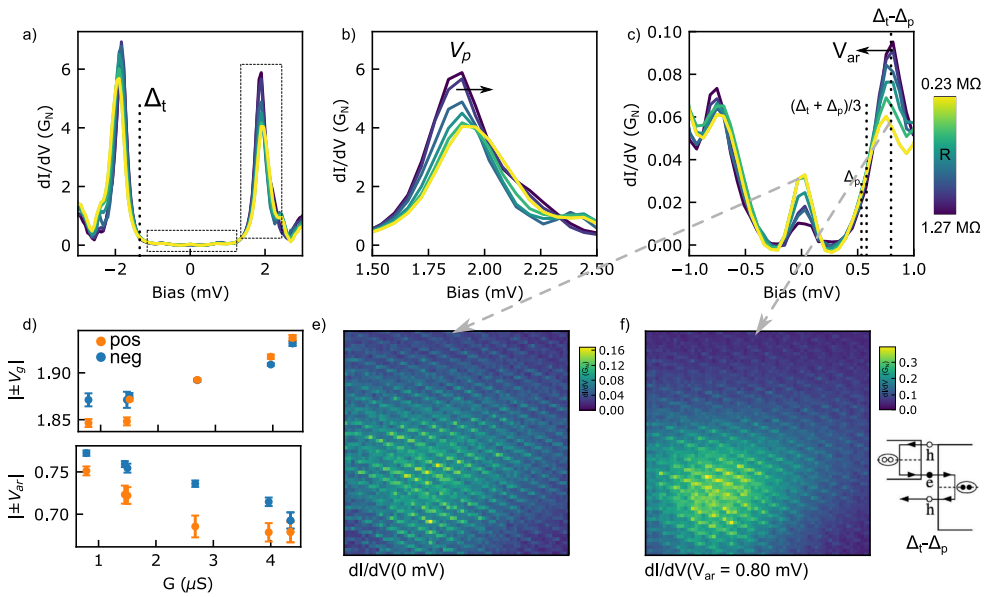

Figure 5.13: Height dependent spectroscopy and Josephson mapping of the corral. a) Set of spectra at different tip heights in the center of the enclosed triangular corral region (V = 6 mV, I from 0.47 nA to 2.6 nA, R decreasing linearly from 1.27 MΩ to 0.23 MΩ). **b)** Zoom of the spectra centered around the positive V_p peak in a), which shifts to higher energy. **c)** Zoom in on the area centered around 0 V in a). The Josephson peak increases while the Andreev reflection V_{ar} peak decreases and shifts to lower energies. **d)** Distance dependence of the peak position of V_{ar} and V_p as the tip approaches. **e)** Map at zero energy of the Josephson peak showing a maximum in the center of the corral. **f)** Spatial distribution of the V_{ar} peak, obtained by mapping the amplitude of the dI/dV spectra at 0.8 mV. On the right, the scheme of the $\Delta_t - \Delta_p$ MAR process from [202].

All the expected MARs are highlighted by dashed lines in the dI/dV of Figs. 5.13a-b, calculated starting from $\Delta_t = 1.35$ meV and $\Delta_p/e = V_p - \Delta_t/e = 0.55$ mV. The MAR process at Δ_t is located at similar energy of the minigap V_p, therefore is hidden by the quasiparticle resonance that prevails on the low Andreev signal in Fig. 5.13a. The $(\Delta_t + \Delta_p)/3$ process is expected to be weak in the $\Delta_p/\Delta_t < 0.5$ regime [202], explaining why is not observed here. The most prominent Andreev reflection signature we at $V_{ar} \sim 0.80 \pm 0.05$ mV coincides with the $\Delta_t - \Delta_p$ process. This is in line with the observed shift of V_{ar} to lower energy, correlated with the opposite shift of V_p [Fig. 5.13d]. The $\Delta_t - \Delta_p$ process consists in a double Andreev reflection where the quasiparticle tunnels relatively deep into the Δ_p continuum. Differently in the process Δ_p the quasiparticle tunnels at energy right above the quasiparticle peak V_p, where in our experiment we observe a conductance dip. This probably suppress the process Δ_p, expected at ~ 0.55 meV [Fig. 5.13c].

In the same 64x64 grid presented in Fig. 5.12, we extract spatial dependence of V_{ar} and the Josephson current in the corral. The spatial dependence of V_{ar} shows a maximum in the center, consistent with its assignation with the MARs process $\Delta_t - \Delta_p$ that follows the distribution of $\Delta_p = V_p - \Delta_t$ reported in Fig. 5.12b. In Fig. 5.13f we show the energy cut at E=0, showing that the Josephson tunneling amplitude has also a maximum centered inside the corral. We have strong evidence that the quasiparticle peak at V_p is caused by confinement since its energy scales with the size of the structure and the intensity map agrees with reported calculations [203, 204]. The modulation of the intensity of the quasiparticle peak V_p reflects in the pairing density, modulating the Josephson tunneling peak, which acquires the same spatial distribution.

In the picture where the Cooper pairs are leaking from the superconductor to the normal metal, the highest paring density, namely Josephson tunneling, is expected close to the S-N interface. In our Pb superconducting corral on graphene, we see that the Josephson tunneling is strongly modulated by the quasiparticle intensity distribution, leading to a maximal pairing density in the middle of the corral. This phenomenology still has no existing theory and is of high interest for unconventional superconductivity [210], where an inhomogeneous superfluid density is correlated with thermal phase fluctuations and glassy superconductivity [211, 212]. The correlation of the Josephson peak with the quasiparticle peak establishes a confinement-engineered Cooper pair density. This is of fundamental interest since it opens up the study of how a different density of Cooper pairs can affect magnetic impurities eventually increasing the impurity-superconductor coupling.

5.6 Magnetic field induced in-gap states in a closed Pb corral on graphene

Quantum corrals are one of the most beautiful experiments done in STM giving access to the quantum coherent nature of electrons [213, 214]. These experiments were successful thanks to the atomic manipulation capability of an STM. Previously we have shown that we can induce a strong proximity effect by confining graphene in the closed corral. Superconducting loops, which are analogous to our Pb corrals, are at the basis of superconducting quantum interference devices (SQUIDs), that found extensive application as magnetic field sensors [215, 216]. These are superconducting loops interrupted by weak links, usually a proximitized normal part or a small barrier [217]. With an external magnetic field, a phase gradient along the loop gives rise to a monotonic closing of the gap in the weak link [Fig. 2.6b]. This effect has been observed by STM, where the phase-dependent density of states is probed in the weak link along the superconducting ring [36]. Another effect of the magnetic field is the formation of vortices. Vortices induced in material with non-trivial topology can induce topological states [218, 219]. It is known that Pb islands behave as type-II superconductors [220, 221], showing the presence of vortices like the one shown in Fig. 5.14. When a magnetic flux of at least ϕ_0 penetrates a proximitized normal metal, a vortex feature can develop in the normal part [64, 222]. To describe vortex

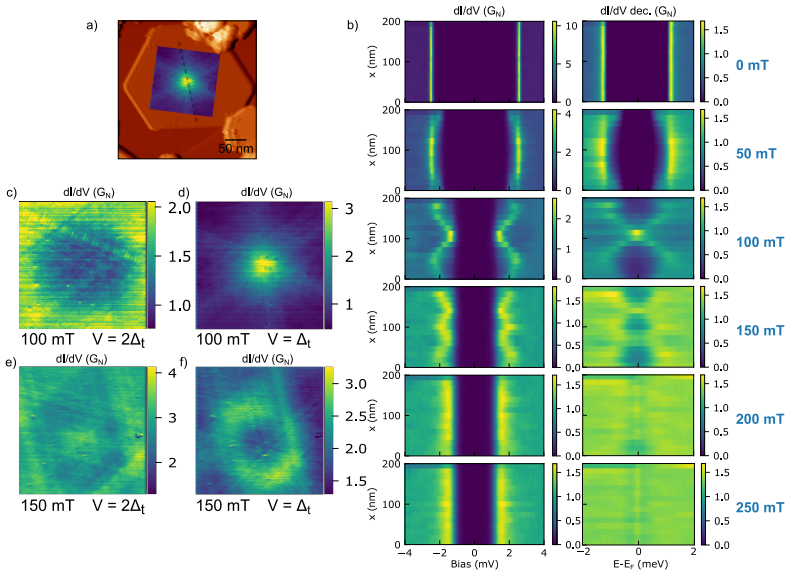

Figure 5.14: Abrikosov vortex on a Pb island on graphene. a) Topography of a Pb island on C-side graphene (V = 1 V, I = 100 pA). We impose a dI/dV map of the vortex as a guide to localize it on the island. **b)** Series of line profiles at different magnetic fields (0-250 mT) along the dashed line in a), with respective deconvolutions ($\Delta_t = 1.35$ meV). At 100 mT a vortex is generated in the island, at 150 mT two vortices are present. At 250 mT only the tip gap is visible. **c)** dI/dV map of the vortex at energy $2\Delta_{Pb}$ and magnetic field 100 mT imaging the suppression of the coherence peaks (V = 4mV, I = 400 pA). **d)** dI/dV map of the vortex at V = Δ_{Pb} and 100 mT, the hexagonal shape of the vortex is due to the Fermi surface anisotropy. **e-f)** dI/dV maps at 150 mT showing a ring-like structure, probably composed of multiple vortices (dI/dV maps at V_1 = 1.3 mV and V_2 = 2.5 mV, stabilization at V = 4 mV, I = 400 pA).

states in normal metals, the term *Josephson vortices* was coined, which is defined as a region enclosing a magnetic flux quantum, without a net current circulating through it. Although progress has been made in the identification of vortexes in proximitized normal metals [223–225], their possible presence in proximitized graphene remains an open question.

Here, we study the magnetic field dependence of the LDOS inside a corral made of Pb islands, constituting a superconducting ring, lying on a normal metal (graphene). This is a very peculiar geometry since the ring itself induces superconductivity in the inner metallic part, thanks to the efficient contact and reduced dimensions. This is a nice platform to investigate flux penetration in proximitized graphene, where no evidence of superconducting vortices has been reported to date. To address this we map the sub-gap structure inside the corral with an applied magnetic field out of the plane. This shows the presence of two regimes, depending on

the magnetic flux penetrating the ring, where we observe either in-gap induced resonances or vortex-like signatures.

We build the closed corral structure in Fig. 5.15a joining 5 Pb islands with the manipulation technique. A zoom in the corral is shown in Fig. 5.15b resolving multiple domains in the enclosed graphene area. We restrict our analysis to the lower domain because this is free-standing like graphene, i.e. there is no Moirè pattern. The spectrum in the corral [Fig. 5.15c] presents one quasiparticle peak resonance V_p at similar energy than the bulk Pb gap. The deconvoluted spectrum in Fig. 5.22d shows a well-developed proximity mini gap, very similar to the Pb bulk. Its spatial distribution, plot in the line profile of Figs. 5.22e-d, shows a homogeneous induced gap along the corral at zero magnetic field.

We estimate the amount of magnetic field that can penetrate inside the corral. In superconductors the magnetic flux is quantized in multiples of $\phi_0 = h/2e$, the quantum of magnetic flux. The magnetic field flux in the corral is $\phi = B \cdot A$, where $A \sim 9000$ nm^2 is the area of the corral and B is the magnetic field value. From this estimation, to have 1 flux quantum penetrating the corral the magnetic field has to go higher than $\sim$ 200 mT. This is the theoretical minimum value to observe flux penetration inside the structure.

The magnetic field dependence data were collected for B ranging from 0 to 300 mT. We start by comparing in Fig. 5.16a a set of dI/dV spectra measured at the center

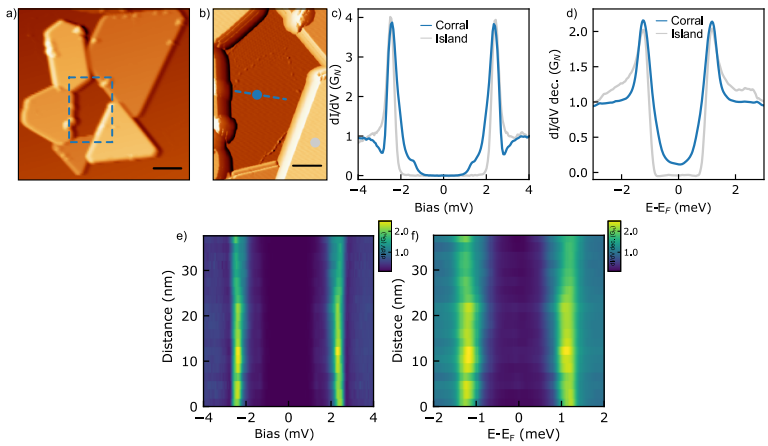

Figure 5.15: Five islands Pb corral DOS. a) Closed corral composed of 5 Pb islands (V = 1 V, I = 100pA). **b)** Zoom of the enclosed graphene region, the lower part without a Moirè pattern was studied (V = 1 V, I = 100 pA). **c)** Spectra of the Pb islands compared with the proximitized region (V = 5 mV, I = 500 mV). **d)** Deconvolution showing the graphene proximity gap. **e)** dI/dV line profile in the corral along the dashed line in b) (V = 5 mV, I = 500 mV). **f)** Deconvolution of the data in e).

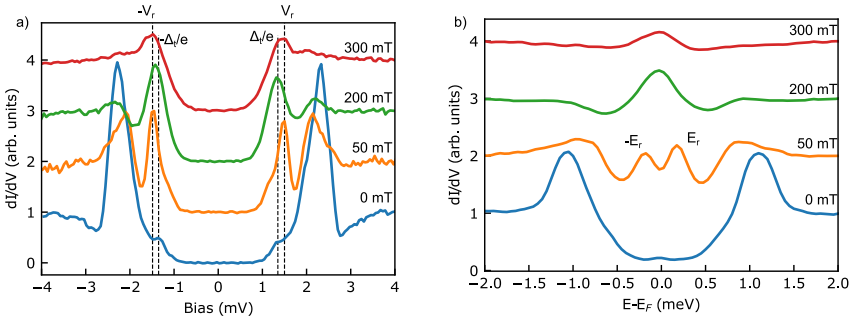

Figure 5.16: B field dependence measured in the center of the corral. a) Spectra in the corral center for 0, 50, 200, 300 mT magnetic fields (V = 5 mV, I = 500 mV). A vertical offset is applied for clarity and the dashed lines serve as guides for Δ_t and V_r **b)** Deconvoluted data from b), visible the in-gap state $E_r \sim 0.25$ meV and the proximity gap $E_p \sim 1.1$meV. To deconvolute we use the bulk Pb superconducting gap $\Delta_t/e = 1.35$ mV, considering it constant for the small range of magnetic fields [226].

of the at 0, 50 mT, 200 mT, and 300 mT magnetic field values, respectively. Remarkably, at 50 mT we observe the appearance of a sharp resonance V_r, with an energy maximum located at 1.54 mV. This value lies between Δ_t and $\Delta_t + \Delta_p$, meaning that V_r lies in the proximitized gap. As shown in the deconvoluted spectrum in Fig. 5.16b, the resonance is well evident after the deconvolution process.

With a 50 mT applied magnetic field, the applied flux is below the value of one quantum of magnetic flux, and theoretically, no magnetic flux is penetrating inside the structure. To induce flux penetration we raise the B field to 200 mT, at $\sim$1 quantum flux value. In the dI/dV at 200 mT Fig. 5.16, we observe that the spectral feature appears now at $V = \Delta_t$, which in the deconvolution corresponds to a peak located at Fermi energy of the sample. This is a signature of magnetic flux penetrating the corral and possibly generating a vortex. Increasing the magnetic field at 300 mT we observe a flattening of the density of states. This indicates that graphene almost recovered a normal metal density of states, although a 300 mT magnetic field still does not quench completely superconductivity.

The evolution of the deconvoluted LDOS in the center of the corral is shown in Fig. 5.17b for magnetic fields between 0 and 300 mT. This remarkably shows three regimes. First, at zero fields, the proximity gap in graphene is fully developed. Second, we observe the appearance of subgap resonances at V_r whose intensity decreases until disappearing. At last, we observe the appearance of a peak at zero energy attributed to the onset of flux penetration in the corral. This signature fades away when increasing the field, a consequence of the gradual quenching of superconductivity by the magnetic field.

We studied the spatial distribution of the LDOS across the graphene in the corral

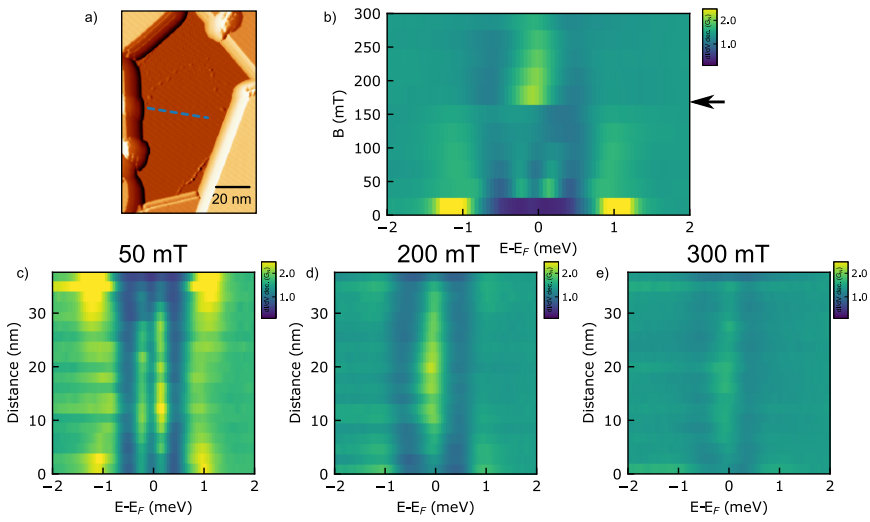

Figure 5.17: Spatial dependence of the dI/dV inside the corral under magnetic field. a) Topography of the inner area of the corral with the line-profile dashed line. **b)** Magnetic field dependence of the dI/dV in the corral center for the extended magnetic field range. Marked by the arrow the point where $\phi \sim \phi_0$. **c-e)** Line profiles of dI/dV spectra along the line in a) for B=50, 200 and 300 mT. (V = 2 mV, I = 200 pA)

by deconvoluting the superconducting tip from dI/dV spectra measured along the dashed line of Fig. 5.17a for various applied magnetic fields. At 50 mT we observe [Fig. 5.17c] that the in-gap state V_r has small spatial dependence, fading slightly close to the Pb islands. For 200 mT, the 0 energy state [Fig. 5.17d] shows a modulated intensity along the corral length. This has a maximum in the center of the corral, where the penetrating magnetic flux is concentrated. Finally, at 300 mT the intensity of the 0 energy state is drastically reduced [Fig. 5.17e], although some density of states is still visible, indicating that superconductivity is not completely destroyed.

We rationalize the experimental finding with two different phenomenologies. The first involves a phase gradient developed along the corral when magnetic flux $\phi < \phi_0$. The second considers flux penetration that leads to Josephson vortex formation in graphene at $\phi > \phi_0$.

We start with the regime $\phi < \phi_0$, where we observe an in-gap resonance at energy $E_r/e = V_r - \Delta_t/e = 0.23$ mV. When a B field is applied on a ring, a phase gradient is developed along the ring to expel the magnetic flux [227–229]. Since our corral is made of separate islands, we approximate it as a superconducting ring made of different sections connected by weak links as sketched in [Fig. 5.18a]. In this configuration, the major phase change occurs in the weak links, which we consider similar to each other, thus giving all the same phase changes. The phase change in a single island is negligible with respect to the weak links. In this approximation the

five islands have respectively 0, $\frac{2\pi}{5}$, $\frac{4\pi}{5}$, $\frac{6\pi}{5}$, $\frac{8\pi}{5}$, closing in a loop of 2π due to the flux quantization of a ring [230].

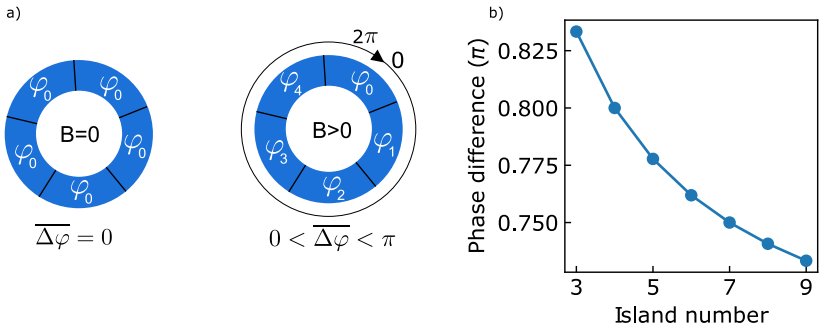

Figure 5.18: Phenomenological model based on phase gradient. a) Scheme of the corral divided into 5 sections (islands), with B>0 a phase gradient develops along the structure closing at 2π. The average phase difference between all islands of the corral for different islands numbers. For a $\Delta = 1$ meV the induced minigap is $V_r = \Delta/e - \Delta\varphi/e$.

Let's recall that in an SNS junction, the gap size depends on the phase difference between the superconductors. In a diffusive system, the electron pathways lose information about the geometry and the minigap depends only on the Thouless energy. We suppose that once the phase is locked in a loop, the Thouless energy is given by the average phase difference between all the island sections. The minigap associated with the Thouless energy closes when the phase difference is π as visualized in Fig. 2.6b. We perform the calculation of the average islands phase difference for corrals with an increasing number of sections. We plot the resulting average of the phase differences between the islands $\overline{\Delta\varphi}/\pi$ in Fig. 5.18b. For 5 islands the result is $\overline{\Delta\varphi_5}/\pi \sim 0.77$, which decreases approaching a saturation value for increasing islands number. Considering a minigap completely open at $\overline{\Delta\varphi} = 0$ and completely closed at $\overline{\Delta\varphi} = \pi$, the theoretical expected minigap value is $E_r^T = \Delta(1 - \overline{\Delta\varphi_5}/\pi)$. In our deconvoluted data in Fig. 5.16b, the deconvoluted position of the proximity gap V_p in the corral is ~1.1 mV, this results in an expected theoretical minigap of $E_r^T \sim 0.25$. The in-gap state is at $E_r = eV_r - \Delta_t$ ~0.25 meV, indeed matching with the resulting minigap extracted from the simple model.

In the regime where $\phi > \phi_0$ we observe the sudden appearance of 0 energy conductance. The Josephson vortices are an analogy with the more conventional Abrikosov vortices of type-II superconductors [231]. These are characterized by zero energy bound states for electrons in the vortex core, described by Caroli deGennes and Matricon (CdGM) [232]. The CdGM states can be imaged by STM and present a characteristic energy splitting that increases with the distance from the vortex core until the CdGM states merge with the gap in superconductor outside the vortex [233–235]. The sudden appearance of 0 bias dI/dV signal at $\phi = \phi_0$ suggests the formation of a vortex due to the penetration of flux in the corral. In the line profile of Fig. 5.17d

we see that the maximum of the 0 energy signal is in the center of the coral, but the characteristic splitting of the CdGM peak going away from the vortex center is not visualized [e.g. see Fig. 5.14b at 100 mT]. We attribute this to two observations. First, since the measurement is done entirely in the proximitized graphene part, we are not imagining the transition between the inner vortex normal core and the superconductor, that is where the zero energy state dispersion is usually observed. Second, the radius of a vortex developed on the Pb islands is ~ 200 nm, larger than the confined area of measurement in the corral. The observed vortex is different than conventional Abrikosov vortices, motivating further research and theoretical modeling.

In conclusion, we realized and probe locally for the first time a superconducting corral on graphene, that shows an intriguing magnetic field response. Below the flux penetration onset, the dI/dV is dominated by an in-gap resonance, for which we propose an explanation based on the phase gradient developed along the ring. Sweeping up the magnetic field, we observed a sharp transition that is a hallmark of flux penetration. The prominent 0 energy peak in the deconvoluted DOS and the spatial distribution consist in a piece of evidence of a Josephson-like vortex in graphene. However, the observation of a well-defined vortex core remains elusive. This platform opens for further investigations, e.g. the possible interplay of the in-gap features with Yu-Shiba-Rusinov states generated by magnetic impurities.

5.7 Collective proximity effect in Gr/SiC0001 (Si-side)

The proximity effect induced by flat superconducting islands on thin conductors has been studied in several substrates, from 200 nm Al islands on Gr/SiC0001 [35], or monolayer Nb_2Se on HOPG [236]. All these studies have in common that the superconducting coherence length is smaller than the inter-island distance. This caused a relatively inhomogeneous proximity effect depending on the amount of area covered. It has been predicted that when superconducting islands are uniformly distributed on a fraction of the surface area at distances comparable with ξ, superconductivity can be induced uniformly [237] giving rise to a metal-to-superconductor transition [238]. The theoretical pre-requisites for having this transition in graphene are summarized in [237]:

- large gate potential, Fermi level away from charge neutrality point (Dirac point);
- low electron density with respect to metals, to avoid inverse proximity effect and suppression of Pb island superconductivity;
- regular island array, irregularities smear and reduce the gap.

Such a transition was observed in granular superconductors [239] or in patterned superconducting arrays [39] in transport configuration, where the gate voltage can be easily tuned. It was shown that at the charge neutrality point the resistance of

the substrate increases and the superconducting state collapses [39]. The conditions to have a 2D superconductor are very well met on the Si side of Gr/SiC0001 graphene because its strong n-doping shifts the Dirac point 200 meV below the Fermi level. On the C-side, which is at charge neutrality, we are on the metallic side [237]. The Pb proximity in Gr/SiC0001 substrate without graphene was studied and showed strong variations of induced gap [166], this supports that the superconductivity is confined in 2D in the graphene layer.

In this section, we present a signature of the collective proximity effect induced by dispersed Pb islands graphene. This system shows uniform superconducting properties at a large scale that only weakly depend on the local arrangement of Pb islands. To corroborate our analysis we show how changing the island's density affects the induced superconductivity. Finally, we compare the proximity effect induced on the C-side (presented in the last sections) and the Si-side of Gr/SiC.

In Fig. 5.19a we show a topography map of bare Gr/SiC0001 where the terraces are very large with no grain boundaries, in contrast to the C side. The main difference between this side and the C-side resides in the position of the Fermi level in graphene (doping), that the C side is at the charge neutrality point and the Si side is above the Dirac point (n-doped). This is shown in Fig. 5.19b, where the spectrum recorded on pristine Gr/SiC0001 graphene shows the Dirac point as a depression of density of states at -200 mV, while flat bands singularities are frequently seen on the C-side [179, 180]. As a reference for superconductivity, we report in Fig. 5.19c a spectrum in Gr/SiC0001 bare surface measured with the same Pb superconducting tip used for the following measurements. In the same graph, the spectrum obtained by deconvolution from the dI/dV plot the DOS of a superconducting tip with $\Delta_t/e = 1.35$ mV shows a flat, metallic density of states.

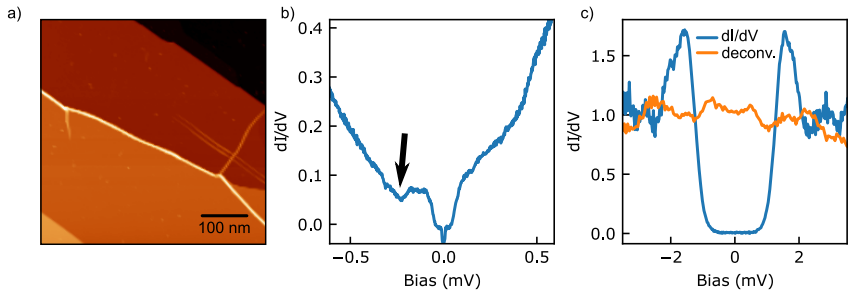

Figure 5.19: Topography and spectroscopy of bare Gr/SiC0001 (Si-face). a) Topography map of the bare Si0001 (Si side) surface (V = 1V, I = 100 pA). **b)** Long-range dI/dV spectrum of the bare Si0001 surface showing the Dirac point depression at $V = -220$ mV, indicating n-doping (V = 1V, I = 1 nA). **c)** Spectra of the bare surface measured with a Pb superconducting tip and imposed deconvolution showing no sign of superconducting gap.

Non-decaying minigap in Si-face graphene/SiC

The Pb growth works on Si-side Gr/SiC in a similar way as explained for C-Side, resulting in 10-15 ML thick islands. In Fig. 5.20a we show an overview topography of SiC0001 after Pb deposition. The substrate is covered with crystalline Pb islands distributed on the surface forming a random array. To simulate ideal conditions of one island proximitizing the graphene we chose the area of Fig. 5.20b and removed the Pb islands around it by pushing them away with the STM tip, to measure the proximity effect resulting from the island left in the area [Fig. 5.20c]. The spectrum in the emptied region [in Fig. 5.20d] shows pronounced peaks at $V_p = 1.60$ mV, and in the deconvolution of Fig. 5.20f we observe a clear gap at $\Delta_p = 0.16$ meV induced in graphene [see Fig. 5.20 for details on the minigap estimation]. The dI/dV spectra were mapped going away from the Pb islands, following the line in figure Fig. 5.20c. In Fig. 5.20d the line of spectra is plotted in a color-map and, remarkably, no visible decay neither of the minigap nor of the intensity of the coherent peaks is observed. In the deconvoluted data of Figs. 5.20f-g we see that the remanent minigap for the deconvolution is indeed extending with no substantial modification.

The fact that the observed features are independent of the distance hinders the estimation of the coherence length with the method used for the C-face Gr/SiC. We will discuss in this chapter that this absent minigap decay is explained by the presence of a distributed array of islands analogous theory used to explain Tin superconducting arrays on graphene [39]. We will see that this minigap depends on the global

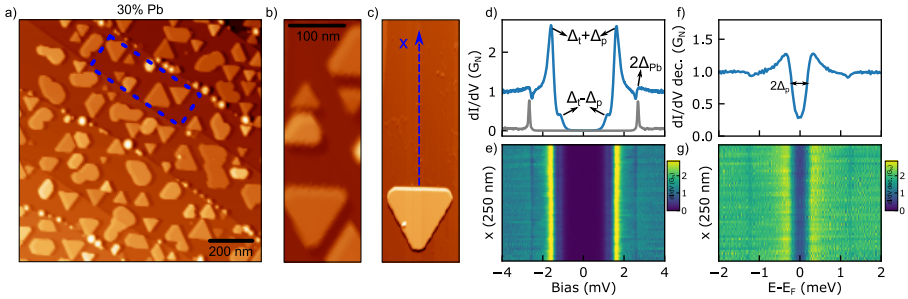

Figure 5.20: Virtually homogeneous proximity gap in Si-face Gr/SiC. a) STM topography of the Si side of SiC graphene after Pb deposition (V = 1 V, I = 30 pA). **b-c)** Zoom of the region highlighted in blue in a), where all Pb islands except one were moved away. **c)** dI/dV spectroscopy of the proximitized region showing a minigap edge at $\pm(\Delta_s + \Delta_t)$ and the thermal excitation at $\pm(\Delta_s - \Delta_t)$ (V = 4 mV, I = 400 pA). **d)** Line of dI/dV spectra recorded moving away from the island in b), showing that the induced minigap stays constant for 250nm. **f-g)** Deconvolutions of d) and e) that shows the graphene minigap of $\Delta_p^{30\%} \sim 0.15$ meV. We estimate the minigap as the spectral energy value at $0.8\,G_N$ value of conductance after normalization to the normal conductance G_N. We will use always this method to compare different minigap sizes.

properties of the sample, such as the island coverage, while the $2\Delta_{Pb}$ onset depends more on the local details of the system, appearing when graphene is confined by Pb islands.

Confinement dependence of minigap and coherence peak

Here, we study the effect of confining the proximitized graphene between two islands, thus forming an SNS junction. A good approximation of an SNS junction in our system is the resonator in Fig. 5.21a. Using the island manipulation technique we tune the mutual distance between two islands. In Fig. 5.21a we report the STM topography maps of the different manipulation stages for spatial gaps between the islands of 115, 102, 69, and 52 nm. In Fig. 5.21b we show the size-dependent spectroscopy, where each spectrum was measured at a point close to the right island. The peak at the bulk Pb onset ($2\Delta_{Pb}$) increases substantially when closing the resonator, this affects the spectral shape of the gap going from the single peak at the minigap onset to a double peak structure. This detail is clear in the deconvolution in Fig. 5.21c where we see that the width of the minigap is also slightly affected by opening from $\Delta_p^{115nm} = 0.18$ meV to $\Delta_p^{52nm} = 0.25$ meV. The spectral shape changes significantly, with the quasiparticle peak weight transferring from the inner peak to the outer peak.

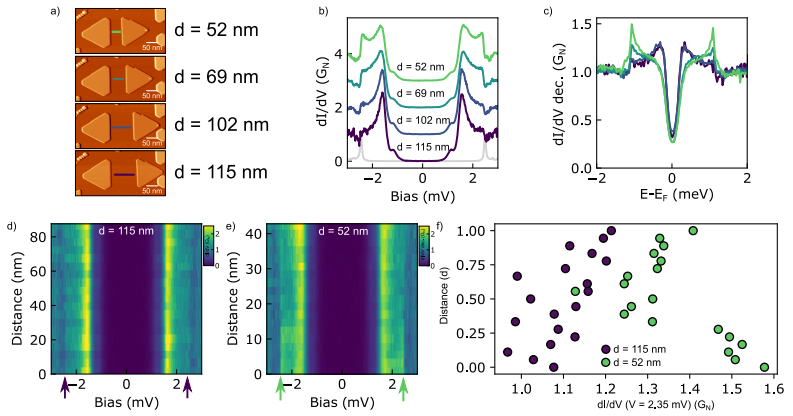

Figure 5.21: Tunable resonators on Si side of SiC graphene. a) STM topography images of the different manipulation stages, where the Pb island on the left was pushed to close the resonator. **b)** dI/dV spectroscopy in the resonators close to the right island, the dI/dV is constant in the direction perpendicular to the edges (V = 4 mV, I = 400 pA). Closing the resonator the direct proximity peaks at $2\Delta_{Pb}$ are enhanced. **c)** Deconvoluted data from b) that shows a slight variation of the minigap from $\Delta_p^{115nm} \sim 0.18$ meV to $\Delta_p^{52nm} \sim 0.25$ meV and change of the spectral shape. **d-e)** Line profiles of dI/dV spectra along the lines in a) for the d = 115 nm and the d = 52 nm. The arrow indicates the onset of the bulk $2\Delta_{Pb}$ peaks. **f)** Density of states at energy $2\Delta_{Pb}$ compared for the small and large island. we performed a summation of around $2\Delta_{Pb} \pm 0.05$meV, averaging for positive and negative bias.

To study the spatial dependence of these features along the resonator we plot in Figs. 5.21d-e two lines of spectra along the topography maps for the largest and the smallest resonator sizes. The arrow indicates the position of $2\Delta_{Pb}$, that in the large resonator shows no peak feature, but only a faint dip, also visible for the isolated island case presented before. In the narrow SNS junction configuration, instead, we observe an overall increase in the intensity of the peak $2\Delta_{Pb}$, with a higher intensity close to the right island (0 nm). If we plot a line cut along $2\Delta_{Pb}$ energy (averaged for positive and negative) we obtain the points in Fig. 5.21f. Here we see that the intensity of the peak at 2 Δ_{Pb} is fairly constant within the noise level for the case of a wide resonator. The peak grows in intensity, being more intense close to the Pb islands. This data points to the different origins of the minigap and the $2\Delta_{Pb}$ peak.

Magnetic field dependence of the minigap and the coherence peaks in an SNS junction

In the previous section, we saw how the minigap edge is only slightly affected by the confinement. In contrast, we se a trend of the $2\Delta_{Pb}$ peak being enhanced in the confined regions like Fig. 5.23b and not present close to isolated islands like Fig. 5.20d. In this section, we study the magnetic field dependence of the same resonator presented before [Fig. 5.22a], where additional islands were coupled to the sides to equal the phase of the two islands. This enhances the signal at Δ_{Pb} and enhances the minigap from 0.24 meV to 0.35 meV.

We compare spectra on two sites. Inside and outside the resonator to see the effect of the magnetic field on the minigap and the $2\Delta_{Pb}$ onset, separately. As shown

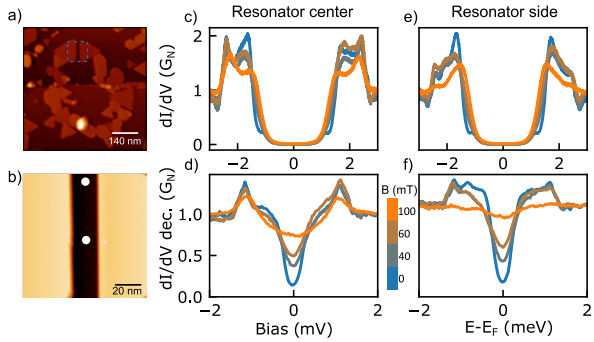

Figure 5.22: Magnetic field dependence outside and inside the resonator. a) SNS junction where the two leads are connected by Pb. **b)** Zoom of the dashed line box in a). **c-d)** dI/dV and deconvoluted dI/dV spectra from 0 mT to 100 mT inside the resonator (V = 4 mV, I = 400 pA). The minigap is fully quenched while the bulk-induced peaks are still visible at $\pm 2\Delta_{Pb}$. **e-f)** At 100 mT magnetic field, at the resonator side, the minigap is fully quenched together with the direct SNS junction proximity.

in Figs. 5.22c-e the onset at $2\Delta_{Pb}$ is more intense in the middle of the resonator, in the absence of a magnetic field. The B-dependent spectra are superimposed on the plots and follow the indicated color scale. The effect of the magnetic field can be clearly observed in the corresponding deconvolution, in Figs. 5.22d-f. We observe that the minigap closes gradually with the magnetic field, in the same way, both inside and outside the resonator. On the contrary, $2\Delta_{Pb}$ onset is still visible inside the resonator, and outside is completely suppressed, confirming again its correlation with the confinement.

Inside the resonator, the bulk $2\Delta_{Pb}$ signature shows only a slight change in response to the 100 mT field, a B value that is well below the island's critical field (200-300 mT). On the other hand, outside of the resonator, the much weaker $2\Delta_{Pb}$ peak is completely suppressed by the field. Notably, the minigap disappears completely both inside and outside the resonator, providing further evidence of its different origin. Feigelman et al. have proposed a model in [237] that predicts that the magnetic field exponentially weakens the inter-island Josephson coupling. This model provides an explanation for the observed suppression of the collective proximity effect minigap in graphene, which reduces the system to weakly coupled Josephson junctions (SNS) that show proximity effect only in confined regions.

Double peak structure of the superconducting proximity gap in a Si-side Gr/SiC confined region

The dI/dV spectrum in a region of graphene enclosed between Pb islands [Fig. 5.23a] shows a very peculiar double-peak structure [Fig. 5.23b]. The presence of a double peak structure was already described first by McMillan [69] and then by

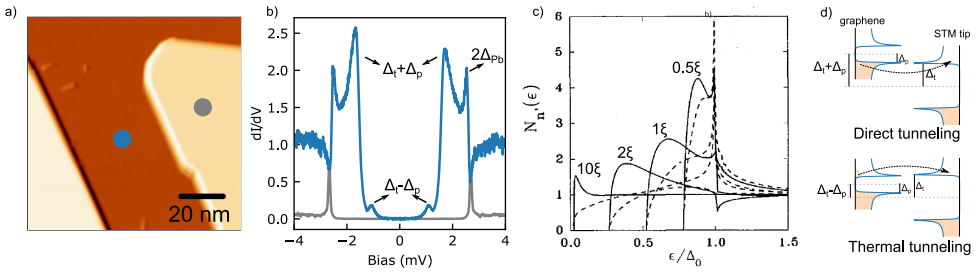

Figure 5.23: Double peak structure in Pb confined Si-face Gr/SiC **a)** Topography map of a Si000$\bar{1}$ graphene region enclosed within Pb islands (V = 1 V, I = 100 pA). **b)** Spectrum of Pb Islands and proximitized graphene (V = 4 mV, I = 400 pA). The in-gap features are thermally activated tunneling processes caused by the tip-sample gap difference. **c)** The calculated density of states for a diffusive SNtNS junction varying the thickness with respect to the coherence length ξ reproduced from [161], where the double peak structure is visible. **d)** Scheme of direct and thermally activated tunneling, to interpret the multiple in-gap peaks of b).

Golubov [161]. In Fig. 5.23c the calculated spectra for a diffusive SNtNS junction (t=tunnel coupling) are reproduced from [161]. Note that increasing the thickness d of the normal metal, the peak at $2\Delta_{Pb}$ is suppressed, but a dip-like feature survives for large d. The peak at $2\Delta_{Pb}$ is due to Andreev reflections at the energy of the bulk Pb superconductor and is enhanced by increasing the confinement as shown previously. While the second peak corresponds to the onset of Andreev conductance in the graphene and is the proximity-induced minigap edge of graphene. Is also remarkable the presence of the thermal excitation at $\pm(\Delta_p - \Delta_t)$ that occurs when the coherent peak of the tip is aligned with the graphene gap [scheme in Fig. 5.23d]. The presence of this excitation is a strong confirmation of the presence of a proximity gap in graphene.

Minigap dependence on Pb island density

According to the model in Ref. [90], the minigap size Δ_p for the collective proximity effect depends both on the average distance between the islands and their size [237]:

$$\Delta_p \approx \frac{2.65 E_{\mathrm{Th}}}{\ln b/4a}, \tag{5.4}$$

in the limit of $b >> a$, where b is the distance between the islands, a is the island radius [Fig1 of [237]], and E_{Th} is the Thouless energy. It is intuitive that Δ_p decreases with increasing islands distance and increases with the size of the islands, thus for a sample with a smaller islands density we expect a smaller induced minigap.

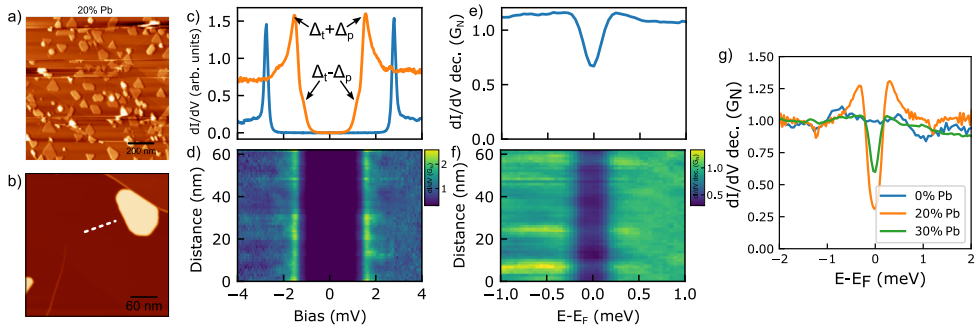

Figure 5.24: Lower Pb amount preparation and comparison. a) Overview topography map of a new preparation with less Pb coverage than the one presented in Fig. 5.20 (V = 500 mV, I = 20 pA). **b)** Isolated Pb island. where additional islands were removed (V = 500 mV, I = 20 pA). **c)** dI/dV spectra of the islands for reference and in graphene. The thermal component $\Delta_t - \Delta_p$ is indicated. **c)** Spectrum along the dashed line in b) showing again no substantial decay of the gap. **e-f)** Deconvolution of c-d) showing the remanent minigap. **g)** Comparison of the deconvoluted minigap for different preparations: $\Delta_p^{0\%} \sim 0$ meV, $\Delta_p^{20\%} \sim 0.08$ meV, $\Delta_p^{30\%} \sim 0.15$ meV.

To test this hypothesis, we repeated a Pb evaporation on graphene with less coverage, using the same evaporation rate but evaporating 2/3rd of the time. From the topographic overview in Fig. 5.24a, we can extract a coverage of ∼20%. That corresponds to about 2/3 of the coverage of the first preparation presented. In Fig. 5.24b, we show an area where all the islands were removed except one. The average graphene spectrum in Fig. 5.24c shows the thermal feature at $\Delta_t - \Delta_p$ and the minigap coherent peak at $\Delta_t + \Delta_p$. The presence of these two processes sketched in Fig. 5.23d ascertains the existence of a proximitized graphene gap. A dI/dV line spectral map in Fig. 5.24d measured along the dashed line of Fig. 5.24b reproduces the constant gap of the previous preparation. Deconvoluting with a $\Delta_t/e = 1.35$ mV tip shows a constant minigap feature [Figs. 5.24e-f]. The comparison of the minigap obtained with %20 and with %30 Pb coverage is reported in Fig. 5.24g. The estimated minigaps for the different preparations are $\Delta_p^{0\%} \sim 0$ meV, $\Delta_p^{20\%} \sim 0.08$ meV, $\Delta_p^{30\%} \sim 0.15$ meV, showing that the minigap increases with the coverage, as expected from equation (4).

The opening of the minigap Δ_p is the result of the Josephson coupling of the array of islands, that scales with the Josephson energy E_J. This quantity is associated with the transfer of Cooper pairs between two superconducting electrodes and must overcome the thermal energy ($E_J > E_t$) to induce the opening of a minigap. In a triangular array of Josephson coupled islands E_J is [39, 237]:

$$E_J(T=0) = \frac{\pi h D}{8 R_\square b^2 \ln^2(b/a)}, \tag{5.5}$$

where D is the graphene diffusion coefficient, $R_\square$ is the graphene sheet resistance in units of the resistance quantum $h/2e$, b is the island distance and a is the island radius. For our case, we give a rough estimation of E_J considering $D \sim 40$ cm^2/s from [240] and a sheet resistance $R_\square$ of 0.2-0.3 $\Omega/\square$ [241, 242]. The parameters a and b [Fig1 of [237]], are estimated by analysis of the 1.15um topographic images [Fig. 5.20a, Fig. 5.24a] using WSxM software [126], where we calculate the average island area and the average next nearest neighbor distance. For the 20% and 30% preparations we estimate $a_{20\%} \sim 25$ nm, $b_{20\%} \sim 100$ nm, $a_{30\%} \sim 45$ nm, $b_{30\%} \sim 120$ nm. The result is $E_J^{20\%} \sim 1.27$ meV and $E_J^{30\%} \sim 1.79$ meV, in both cases greater by one order of magnitude with respect to $E_t(1.3K) = 0.112$ meV.

Discussion and comparison with C-side graphene

It is interesting to compare how the collective proximity changes from C-side to Si-side graphene. In Si-side graphene, the islands behave as an array of Josephson junctions, sharing a global phase thanks to the Josephson currents connecting the islands [237]. Ideally, with a perfect array and a phase equal to zero for all the islands, the induced gap would be equal to the bulk Pb gap. Clearly, we are not in this ideal regime, and the induced gap is only slightly affected by moving islands locally, as in the resonator case. This reduced gap can be viewed as similar to magnetic frustration, where a collection of islands stabilize the phase at an intermediate value, in

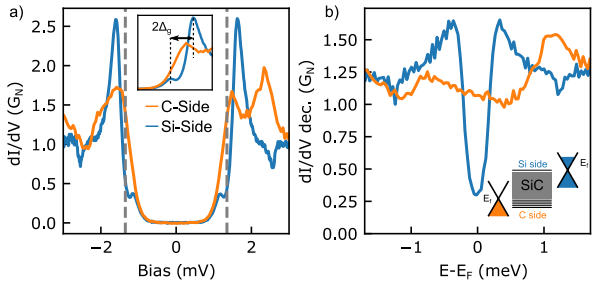

Figure 5.25: Proximity comparison between C-face and Si-face Gr/SiC. a) Spectra 200 nm away from islands extracted from Fig. 5.2b and Fig. 5.20e, blue on Si side and orange on C side (V = 5 mV, I = 500 pA). **b)** Deconvolution showing metallicity (absence of gap) on the C-side and superconductivity on the Si-side, which have different doping (scheme in the inset).

a similar manner compared to a spin ensemble [243, 244]. A major role of the gap smearing is played by phase fluctuations, which can be thermally generated, or due to limited supercurrent channels that connect the islands. What limits the inter-island supercurrent can also be a partial Coulomb blockade due to the weak link between the islands and the substrate [38, 245] and see Chapter 6. The doping of graphene is crucial in determining the metallic or superconducting phase. It was demonstrated that when proximitized graphene is tuned to the charge neutrality point, the collective superconducting state collapse resulting in a superconductor-to-metal transition [39, 239, 246].

In the C-side Gr/SiC, the Fermi level is close to the charge neutrality point [179], thus the proximitized graphene is well into the metal side of the superconductor-to-metal transition. This is indeed the case since on C-side we observe how the coherence decays exponentially from the island to graphene [Fig. 5.2b]. Differently, on the Si side, the superconducting gap does not close away from the islands. In Fig. 5.25, we compare the spectra of C- side and Si-side graphene 200 nm away from Pb islands. On the C-side Gr/SiC we observe the metallic density of states, while on the Si-Side a developed minigap.

Also, the behavior in confined structures is fundamentally different. In the C-side the sub-gap structure and the zero energy conductance are dependent on the confinement [Fig. 5.21] going from a double-gap structure to a homogeneous gap. In Si-side the confinement affects only slightly the gap size, that in the smallest configuration increases the width of the proximitized gap by a small fraction of the bulk gap. The minigap size is defined by the Josephson array phase, and for the wider configuration, the gap saturates at the one measured away from the islands.

In conclusion, we created a Josephson junction array without using patterning or masking techniques. The dependence of the effect with the doping (C-Si side) and

the density of the island confirms the predictions made in [237] and the transport measurements in [39] that demonstrate the presence of a 2D superconducting state confined in graphene with a very homogeneous gap. Apart from a fundamental advance in the understanding of 2D superconductivity and proximity, the substrate could function as a novel platform to study superconductivity and magnetism at the atomic scale.

6 Interplay of Coulomb blockade and superconductivity in Pb islands on graphene

6.1 Introduction

Size confinement, Coulomb repulsion, and weak electric contact in metallic islands induce the formation of energy gaps between states with different electron numbers [40–42, 247]. In 1959, Anderson proposed a size limit below which an island ceases to be superconducting [248]. Below the Anderson limit, the minimum energy level spacing, called Kubo gap [249], is larger than the superconducting pairing energy, thus there are no superconducting correlations. This occurs when reducing in size the superconductor, being a quantum dot the extreme limit, where the level spacing can be in the order of eVs [250]. The size reduction enhances electron-electron Coulomb repulsion, which competes with the attractive electron-phonon coupling responsible for superconductivity. The Coulomb interaction can prevail below a critical size, inducing a superconductor-Coulomb insulator transition with the reduction of the dimensions [236].

If superconducting correlations can survive in the presence of Coulomb repulsion and how this affects the excitation spectra is still an open question. This coexistence can be especially interesting in superconductors, whose electron parity (electron number) is a conserved quantity. The Coulomb repulsion can force the number of electrons in the system to be even or odd [251–254], inducing quantum phase transition analogous to the YSR case [255], phenomena at the basis of Majorana q-bits based on small superconducting islands [30].

Superconducting gaps larger than the bulk value are not always related to the destruction of superconductivity. For example, a superconducting gap twice the one of bulk Pb was observed in small Pb islands on STO. This was interpreted as a substrate-mediated electron-phonon coupling enhancement [256]. Another cause of gap opening can be the weak electric contact between the nanosized superconductor and the sample. This is described by Coulomb blockade physics, a successful framework, adopted to describe many experiments [38, 41, 43, 44, 74, 257]. The main aspect is a depression of the density of states near zero energy, visible in dI/dV spectroscopy at voltages below the charging energy $E_C = 2e/C$, and at sufficiently low temperature ($E_C \leq k_b T$).

Here, we study the interplay of Coulomb blockade with superconductivity in

small Pb islands grown on C-side Graphene/SiC. We found that, for islands with lateral size below ∼50 nm, the charging energy E_C has a similar magnitude compared to the Pb superconducting gap. When the lateral size of our Pb island is below a critical value (~20 nm) we observe the appearance of a Coulomb blockade gap, as reported by Brun et. al. for Pb islands on HOPG [Fig. 6.1a] [38]. For intermediate-sized islands, between 20 nm and 50 nm, we observe a strong asymmetry of the coherence peaks. This asymmetry can be switched by moving the Pb islands on the surface with the island manipulation technique. The presence of bias and conductance asymmetries of the Coulomb blockade gap are usually connected to the excess charge trapped in the island, which can depend on local variations of in the substrate work function [41, 74, 258]. For example the spectrum of a metallic island in Fig. 6.1b, reproduced from [43], was interpreted as caused by the sign change of the excess charge trapped in the island.

Following these observations, we developed a simple model to describe asymmetric BCS features caused by the change of excess charge in the island. The latter shifts the Coulomb blockade gap with respect to zero energy and translates into the suppression of either particle or hole character of the quasiparticle excitation spectrum.

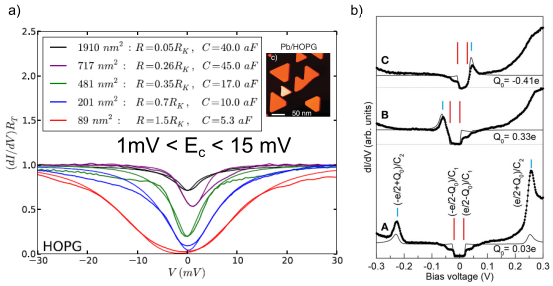

Figure 6.1: Coulomb blockade gap and excess charge. a) a) Volume-dependent Coulomb blockade gap observed on Pb islands on HOPG, reproduced from [38]. **b)** Asymmetric dI/dV on Pb islands on NaCl/Ag111. The asymmetry is tuned is tuned by bias pulsing, which changes the excess charge trapped on the island, data reproduced from [43].

6.2 Coulomb blockade gap in small Pb islands on graphene

Pb islands with thickness 3-7 nm and lateral size $l > 100$ nm can be easily grown on graphene, as shown in chapter 5. These Pb islands present a superconducting gap of the same size as the bulk Pb crystal gap and a BCS line shape. In Gr/SiC samples with a higher density of defects, we observe more poly-disperse growth of clusters, as shown in Fig. 6.2a, with the presence of small crystalline islands ($l < 10$ nm). Remarkably, in these small Pb islands we measure a larger absolute gap, for example as in Fig. 6.2b for an island of $l \sim 18$ nm, compared with a large island of $l \sim> 50$

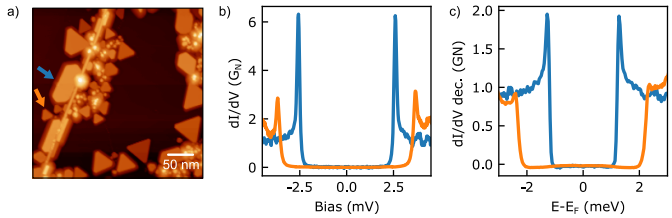

Figure 6.2: Large and small Pb islands limits. a) Topography image of Pb islands on Gr/SiC C-face, highlighting a large and a small Pb island (V = 1 V, I = 100 pA). **b)** dI/dV spectroscopy on the two islands in a) (V = 5 mV, I = 500 pA). **c)** Deconvolution of the spectra in b) showing BCS-like coherence peaks for the big island and steps for the small island.

nm. Note that the gap lineshape in the former case is different than a BCS line shape, as one can check by exploring the deconvolution spectra in Fig. 6.2c. In fact, in the deconvoluted spectrum, the gap edges are visible as bare step features with no coherence peaks. This gap shape is analogous to the one reported by Brun et. al [38] [Fig. 6.1a], interpreted as a Coulomb blockade gap. In our case, the particularly sharp and absolute gap feature is caused by the superconducting tip, which at T = 1.3K is unaffected by Fermi-Dirac broadening (see section 2.5).

To test the nature of the observed gap, we apply a magnetic field out of the plane, comparing the behavior of the small and large islands of Fig. 6.2a. Coulomb blockade coexisting with superconductivity results in the shift of coherence peaks at $E = E_C + 2\Delta$. Since the superconductivity is suppressed by the magnetic field, the 2Δ contribution to the gap is expected to vanish [73, 257]. In Fig. 6.3a we plot a stacked color plot with an increasing magnetic field on the large reference island. Both tip and sample gap close completely at 1.2 T, leaving a depression typical of dynamical

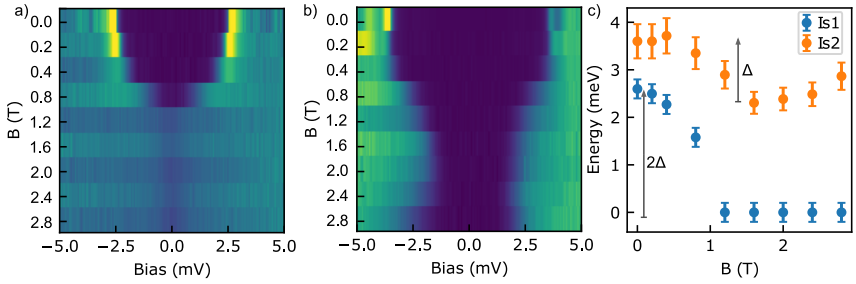

Figure 6.3: Magnetic field dependence of small and large Pb islands. a-b) Stacked dI/dV spectra at increasing out-of-plane magnetic field for the large and small Pb island of Fig. 6.2 (V = 5 mV, I = 500 pA). **c)** Energy gap plotted in function of the magnetic field showing the closing of the gap: Δ for the small island and 2Δ for the big island.

Coulomb blockade effects [74, 199]. Sweeping the magnetic field and measuring on the small island in 6.3a, we also observe an initial gap closing, that saturates at 1.2 T. In Fig. 6.3c we quantify the gap closing, resulting $2\Delta_{Pb}$ for the large island and only Δ_{Pb} for the small island. For the measurements, we used the same superconducting tip, and in the small island, only the tip gap is contributing to the gap closing while the sample gap remains unchanged. This suggests that the observed gap in this small island has pure Coulomb origin, and, thus, Coulomb blockade competes in these with superconducting pairing.

To probe the presence of superconducting correlations in the islands we perform point spectroscopy approaching the superconducting tip to each island of Fig. 6.2a. When the tunneling resistance between two superconductors, tip, and island, is below 1MΩ, a dissipation-less Josephson current flows between the two leads. To have this effect both the tip and the sample must be superconducting. For the two islands of Fig. 6.2a we approached the tip reaching the Josephson tunneling regime up to 600 kΩ. In Fig. 6.4 we compare two z-approach experiments with the same resistance ranges. On the large island, used as a reference, we have a supercurrent while on the small one, we do not observe any. A possible explanation is that the Josephson current is Coulomb blocked since it is a 2-electron transfer process for which E_C has to be paid. In contrast to this, Averin et. al [73] predicted that charge fluctuations can induce Cooper pair tunneling without changing the net charge of the central electrode only if the system is fully particle-hole symmetric. Nevertheless, the absence of Josephson current in the small islands suggests that at these very small sizes, no superconductivity survives to Coulomb repulsion.

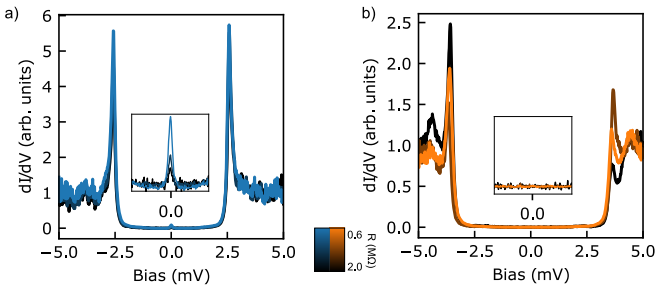

Figure 6.4: Josephson spectroscopy on big and small Pb islands. a) dI/dV spectroscopy approaching the STM tip from 2 to 0.6 MΩ on the small where the Josephson peak is visible. **b)** At the same tunneling resistance no Josephson tunneling is observed for the small island (V = 5 mV).

6.3 Energy gap size dependence and gap asymmetry for intermediate sizes Pb islands

The large and small island limits are well understood in the framework of BCS and Coulomb blockade regimes, respectively. Regarding the islands with intermediate sizes between 20 and 50 nm, the behavior is strikingly different. Here, we explore the regime of $E_C \sim \Delta$ by measuring the energy gap of many islands and studying how it scales with the size of the island. In Fig. 6.5a we plot the measured gap against the lateral size of the islands for around 30 islands. We see that below the *critical size* $l < 20$ nm, the gap opens, as described in the previous section. In Fig. 6.5a we also see a trend of gap suppression with respect to the Δ_{Pb} line. This is explained by finite mean energy level spacing, which can be estimated using random matrix theory [259]:

$$E_{spac} = \frac{\pi^2 \hbar^3}{e(1.2m_e)^2 v_F V}, \tag{6.1}$$

where $v_F(Pb) \sim 1.83 \cdot 10^6$ m/s. In Fig. 6.5b we plot eq. 6.1 against the volume and see that $E_{spac}(eV) \ll \Delta_{Pb}$ for our smallest island ($\sim$ 400 nm). This allows us to assume a level spacing (Kubo gap) smaller than the superconducting gap. This means that in the size regime of the islands studied, we are still well above the Anderson limit ($E_{spac} < \Delta$), and the presence of a finite level spacing results in a slight weakening of Δ. This phenomenon was studied for Pb islands in silicon [44, 260, 261] and is understood within the BCS framework incorporating the minimum level spacing [260].

In this intermediate-size regime, we also observe a recurring strong asymmetry in the coherence peaks. The recurrent line shape of the asymmetric gaps in Fig. 6.5c show a pronounced coherence peak and broadened conductance step on opposite

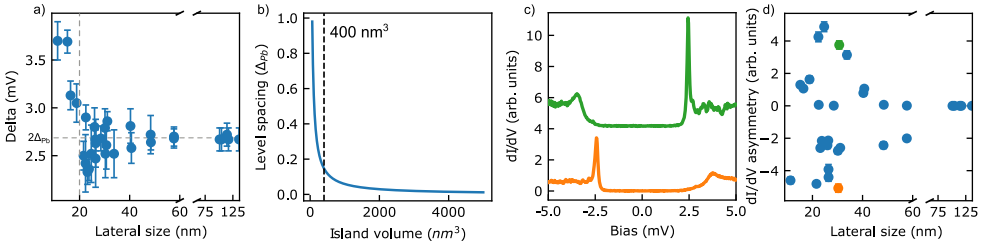

Figure 6.5: Statistics of gap size and gap asymmetry. a) Superconducting gap for different size islands showing a decreasing trend and a sudden opening at the critical size value when $E_C \sim \Delta$. **b)** Energy level spacing in a metal estimated from eq. 6.1, the dashed line indicates our smallest island. **c)** Asymmetry of positive and negative gap edge conductance shifted vertically (V = 5mV, I = 500 pA). **d)** Two examples of asymmetric dI/dV with opposite asymmetry.

bias values. In Fig. 6.5d we show that this asymmetry reaches the maximum close to the critical size, with both large positive or negative asymmetries.

The spectral asymmetry does not depend on the thickness of the islands or a particular shape, but only on the size. To test if it is dependent on the island's position on the substrate, we perform an island manipulation experiment. We selected the island in Fig. 6.6a. Which shows an asymmetric spectrum in Fig. 6.6c, and laterally moved it with the STM tip to another position on the same graphene [Fig. 6.6b]. Upon the manipulation process the dI/dV spectrum on the island, Fig. 6.6d, remarkably inverts its asymmetry, showing reversed features. Removing the effect of the tip with a deconvolution [Fig. 6.6e], we obtain spectra that show a coherence peak a BCS coherence peak only on one bias polarity, and a step feature on the other side. It has been predicted that the presence of an excess charge can induce a bias asymmetry between the coherence peaks at different polarities [251, 255]. Together with the asymmetry switch, we observe also a slight asymmetry in the bias position of the positive and negative coherence peak, which also switches upon island manipulation. This type of switching of spectral asymmetry was also observed in Coulomb-gapped metallic islands and interpreted as local work function difference on several positions of the substrate [258] or charging of the islands induced by bias pulsing [43]. In the same way, we interpret this effect as resulting from an excess charge located on the island, that act as a local potential gating. This can shift the Coulomb blockade gap that suppresses one quasiparticle excitation peak depending on the sign of the excess charge and produces bias asymmetries.

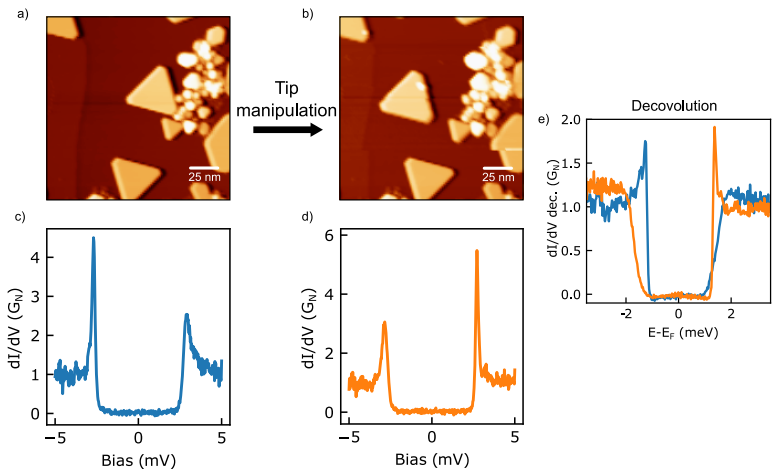

Figure 6.6: Asymmetry switch upon island manipulation. a-b) A Pb island is manipulated on the surface of graphene using the island manipulation technique. **c-d)** The dI/dV spectrum inverts its asymmetry upon manipulation (V = 5 mV, I = 500 pA). **e)** Deconvolution shows the presence of a BCS-like coherence peak and a step typical of the Coulomb blockade gap.

6.4 Discussion and conclusions

One approach for treating weakly coupled metallic grains like the Pb islands on graphene is the double barrier tunnel junction (DBTJ) model. This formalism describes a series of two tunnel junctions: tip-island (1), characterized by resistance R_T and capacitance C_T and island-substrate (2) with resistance R and capacitance C, as sketched in Fig. 6.7a. As introduced in chapter 2.4, the rich phenomenology that this framework can describe comprehends the Coulomb blockade and the Coulomb staircase. A didactic limit considered in [41] is when $R << R_T$, here the position of the Coulomb gap is $E_C = e/2C$ and the first Coulomb staircase step is at $E_s = e/2C_T$. In the limit of small C_T, the DBTJ reproduces the Coulomb blockade gap [Fig. 6.7a] which can be shifted by the presence of an excess charge in the island Q_0. As explained in chapter 2.4, the same result can be obtained in the dynamical Coulomb blockade (DCB) framework where the capacitance effect enters the P(E) function through the circuit impedance [38, 74, 262]. Also, a dissipative component of the P(E) function is present in tunneling experiments, resulting in a gap only visible at millikelvin temperatures [76]. It was recently demonstrated that tuning the tip-sample distance can lead to a transition from a double junction to a system where one single junction dominates [39, 258]. While the island-graphene resistance is probably in the order of the quantum of resistance (12 kΩ), we estimate the typical values of island-substrate capacitance by fitting the Coulomb gap in the absence of superconductivity in Fig. 6.7b. This results in a Coulomb gap onset at 1.78 mV bias and a capacitance $C = 350$ aF, two orders of magnitudes larger than the typical tunnel capacitances $C_T \leq 1$ aF [38, 74], justifying the choice of $C >> C_T$.

To describe the asymmetry raising in the spectroscopy, we consider supercon-

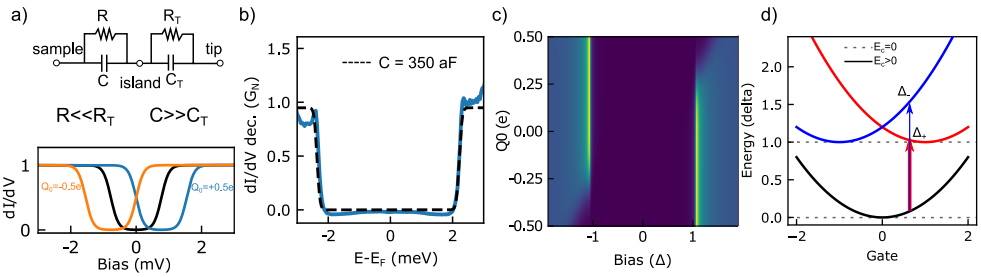

Figure 6.7: Double junction framework and charging energy. a) Scheme of a double tunneling junction between tip-island-sample. In the graph below, the Coulomb blockade gap (eq. 2.41 for different values of the excess charge Q_0. **b)** Fit of the Coulomb gap of the small Pb island of Fig. 6.2. **c)** BCS spectrum dependence on the excess charge Q_0 resulting from eq. 6.2. **d)** The dashed line are the excitation of a superconductor with $E_c = 0$, the solid parabolas for $E_c > 0$. In black the ground state, in blue the negative bias excitation (Δ_-/e), and in red the positive bias excitations (Δ_+/e) [73].

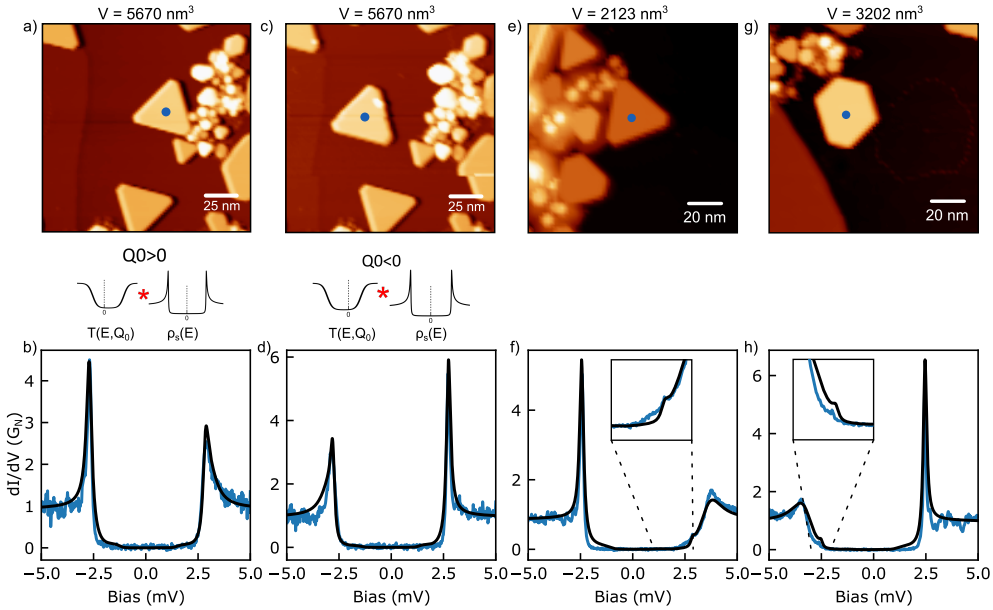

Figure 6.8: Fit of the asymmetric gap dI/dV and fit with eq. 6.2. a-b) Island in Fig. 6.6 before the manipulation ($V_{\text{shift}} = 50\ \mu$V, $\Delta_+/e = 2.86$ mV, $\Delta_-/e = 2.76$ mV, $(\Delta_+/e + \Delta_-/e)/2 = 2.81$ mV) **c-d)** Fit of the same island of a) after manipulation ($V_{\text{shift}} = 90\ \mu$V, $\Delta_+/e = 2.70$ mV, $\Delta_-/e = 2.88$ mV, $(\Delta_+/e + \Delta_-/e)/2 = 2.79$ mV). The inset shows the shift of the Coulomb gap caused by Q_0, where * stands for multiplication. **e-f)** Island with a volume of 2123 nm^3 shows a stronger asymmetry with a remanent peak that is reproduced by the fit ($V_{\text{shift}} = 170\ \mu$V, $\Delta_+/e = 2.83$ mV, $\Delta_-/e = 2.49$ mV, $(\Delta_+/e + \Delta_-/e)/2 = 2.66$ mV). **g-h)** dI/dV spectrum on a Pb island of 3202 nm^3 showing positive asymmetry ($V_{\text{shift}} = 160\ \mu$V, $\Delta_+/e = 2.41$ mV, $\Delta_-/e = 2.57$ mV, $(\Delta_+/e + \Delta_-/e)/2 = 2.49$ mV). (for all spectra V = 5 mV, I = 500 pA), (for all topography V = 1V, I = 100 pA)

ductivity and the Coulomb blockade gap as two parallel effects. The Coulomb blockade modifies the transmission function of the junction, $T(Q_0, E)$, giving a dip in the density of states even in the absence of superconductivity. This can be written in terms of a simple tunneling current as:

$$I(V) = \int_{-\infty}^{\infty} T(E, Q_0, E_C)\rho_s(E, \Delta_s, \Gamma_s, V_{\text{shift}})\rho_t(E - V, \Delta_t, \Gamma_t)[f(E - V) - f(E)]dE, \tag{6.2}$$

where ρ_s and ρ_t are the tip and sample density of states (described with Dynes functions eq. 2.1). We calculate the $T(E, Q_0, E_C)$ with the DBTJ model (eq. 2.41, and convolute it with Fermi-Dirac distribution to add thermal smearing (T = 1.3 K). In Fig. 6.7c, we plot dI/dv spectra simulated from eq. 6.2 for different excess charges Q_0 and we see that an asymmetry is induced for positive and negative excess charges,

with suppression of one of the quasiparticle excitation peaks. In this effective model, what produces the suppression is the position of the Coulomb gap edge with respect to the coherence peak, while the absolute value of E_C is not important since once the onset of the Coulomb gap is inside the BCS gap stops affecting the coherence lineshape (as is the case for the large Pb islands). Using this simple model, we fit in Fig. 6.8 the asymmetric spectra for three representative islands. Is interesting to prove that on the smaller island [Figs. 6.8e-g] the quasiparticle peak suppression is more pronounced, due to the larger Coulomb gap. We can see this effect comparing the gaps measured for the islands in Fig. 6.8. In Figs. 6.8a-b the same island is manipulated and the only change we observe is the asymmetry switch with no modification of the island gap. Instead, for the two islands in Figs. 6.8e-h we observe a lower bulk gap with a different value for the two islands, due to the different island volumes.

In islands like in Figs. 6.8e-h we observe a remanent peak, visible in the graphs insets. Comparing the energy of the remanent peak and the coherence peak we find a bias asymmetry where the intense peak is at lower energy compared to the faint peak. We interpret this asymmetry on the basis of a gating-dependent bias asymmetry. This phenomenology is described in Fig. 6.7d where the parabolas are the ground BCS ground state energy (black) and quasiparticle excited states for N+1 (positive) and N-1 (negative) excited states [73]. The presence of the charging energy results in a parabolic dependence on Q_0, introducing a gating-dependent bias asymmetry of the excitations. To account for this we introduce a phenomenological asymmetry parameter V_{shift}. The offset is $V_{\text{shift}} = 50\ \mu$V for the islands in Figs. 6.8a-d and, as expected, larger for the islands with smaller volume in Figs. 6.8e-h that shows $V_{\text{shift}} = 170\ \mu$V. In this framework, one of the coherence peaks is partially suppressed by the Coulomb blockade gap. In Fig. 6.9 we show that the negative bias coherence peak can be entirely suppressed in a smaller island. The remanent coherence peak at positive voltage is well described by a BCS lineshape, while the Coulomb edge is located at

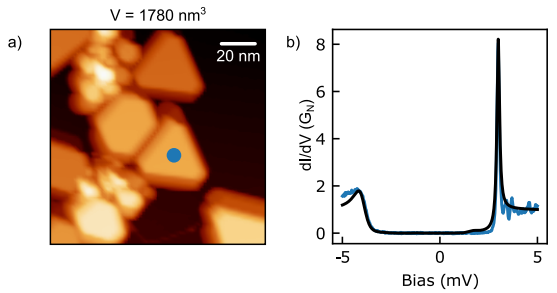

Figure 6.9: a) Topography of an island with volume 1780 nm^3, (V = 1 V, I = 100 pA). **b)** dI/dV spectrum on the island shows a pronounced asymmetry with the coherence peak at 2.98 mV, the bias offset cannot be estimated since there is no remanent coherence peak (V = 5mV, I = 500 pA).

high energy due to the large E_C. Remarkably the coherence peak at positive is at 3 mV, indicating an expected prominent gating-dependent position of the coherence peak.

In conclusion, we tune the ratio between the positive and negative quasiparticle excitations by laterally manipulating the island. This is achieved in islands with $E_C \sim \Delta$ where superconductivity coexists with Coulomb blockade effects. We interpret the asymmetry as induced by local work function modulations of graphene that induce an arbitrary excess charge (gating) on the island, where the island manipulation can remarkably allow switching between two asymmetry extremes. The control of the charge by external gating would allow tuning arbitrarily the particle-hole weight, which possibly can modulate the supercurrent through the junction. The understanding of how the charging energy affects superconductivity paves the way for exploring how other types of quasiparticle excitations e.g. Yu-Shiba-Rusinov states can interplay with charging effects.

7 Conclusions

In this Thesis, I use a set of experimental tools manipulating magnetic atoms, molecules, and superconducting islands to advance the understanding of superconducting excitations at the atomic scale. The controlled conditions achieved by STM allow the use of relatively simple theoretical frameworks that give insights into system phenomenology.

In chapter 3, we show how we can control and simulate the YSR states in atomically precise Mn lattices on β-Bi_2Pd . Although the system is not suitable for topological superconductivity, we can apply a simple model to describe the coupling in 2D extended structures. The anisotropic character of the Fermi surface and the symmetry breaking due to the rotation with respect to the β-Bi_2Pd lattice of the 5-Mn structure changes the splitting of the particle-hole asymmetry. This is captured by the multi-impurity Green function approach that incorporates the anisotropic Fermi surface. In a 25 Mn atom lattice, we observe the emergence of three YSR modes that arise due to the YSR coupling. Our multi-impurity model allows us to simulate the structure, and by comparing them with experimental results, we identify 3 YSR modes with different spatial distributions.

In chapter 4 we study the rich many-body excitation spectrum of magnetic impurities on a proximitized gold film, deposited on vanadium. The magnetic molecule FeTPPCl interacting with the substrate electrons hosts subgap YSR states and spin excitations outside the gap that are readily described by a superposition of Bogoliubov quasiparticles and impurity spin states using a zero-bandwidth model. Our research uncovered an interesting Cooper pair-breaking excitation on molecules in the Kondo-screened regime, which scales with the induced gap of the proximitized film. This is an excitation that remains hidden from tunneling electrons and becomes available for magnetic impurities that bind a quasi-particle, thus behaving as a detector of the parity of the ground state.

In the last study, we used a bulk superconductor to induce superconductivity in Au by the proximity effect. In the reversed configuration, superconducting correlation can be induced in a bulk material like graphene grown in SiC, in proximity of Pb islands deposited on the surface. We investigated locally this phenomenon using a technique that enables the smooth sliding of Pb islands on graphene. In this Thesis, we studied how graphene domain boundaries on graphene act as mirrors for corre-

lated quasiparticles and how the presence of a twisting angle strongly suppresses the coherence. Using the manipulation we built a tunable SNS junction where we can see a transition between an asymmetric diffusive junction to a homogeneous ballistic-like junction.

The confinement of superconductivity by Pb islands allows the creation of a robust superconducting state that calls for a fundamental study of Andreev reflections and Josephson currents in graphene. Measuring at high conductance we unravel Andreev reflection processes in proximitized graphene observing different processes depending on the size of the induced gap. In a confined Pb corral, we map the spatial dependence of the Andreev reflections and the Josephson supercurrent. We find that the confinement induces the formation of quantum-well states that influence the quasiparticle excitation. We correlate this with the Josephson current map, which is proportional to the Cooper pair density. In this measurement, we find that the Cooper pair density is modulated presenting a maximum in the center of the corral. This experiment paves the way for engineering the pair density texture by confinement of the proximity effect.

Until here the substrate employed is Gr/SiC grown on the C-side of SiC where the Fermi level is at charge neutrality. The graphene is grown on the Si-face of the SiC polar crystal and presents a strong n-doping that radically changes the proximity effect. With STM capabilities we map the induced proximity gap and find that it is extended homogeneously in graphene. The effect is emerging from the Josephson coupling of the dispersed array of Pb islands, which induces a macroscopic 2D superconducting state. This study brings fundamental advances in probing locally the induced collective superconductivity. Finally, the substrate constitutes a novel platform to study superconductivity and magnetism at the atomic scale with all the advantages of graphene.

The Pb islands on graphene of the precedent studies are large enough to show bulk BCS properties. For small islands $l < 50$ nm we observe Coulomb blockade phenomena and study their interplay with superconductivity. Below a critical size, the islands show no sign of coherence, Josephson tunneling, or magnetic field dependence. For intermediate sizes, we see strong modifications of the superconducting gap with remarkable coherence peak asymmetry that becomes more accentuated at lower sizes. With the island manipulation technique, we switch the asymmetry changing the island's position on graphene. This is modeled via a phenomenological model that describes how the observed asymmetry switch is due to a change in the local work function of graphene that modifies the excess charge on the island. This joint with the manipulation can be used as a probe for the local work function of graphene.

The results and analysis presented in this Thesis provide comprehensive research on superconducting excitations at the atomic scale using a variety of experimental tools and theoretical frameworks. The platforms employed offer powerful

insight toward a deeper understanding of superconductivity and its interactions with magnetism, proximity effects, and Coulomb blockade. This work contains meaningful steps forward in our understanding of superconductivity and related phenomena, and its insights will inform and inspire further research in this exciting and rapidly evolving area of condensed matter physics.

Bibliography

[1] G. Binnig and H. Rohrer. "Scanning Tunneling Microscopy". In: *Surface Science* 126 (1983), pp. 236–244. DOI: 10.1016/0039-6028(83)90716-1.

[2] I. Giaever. "Energy Gap in Superconductors Measured by Electron Tunneling". In: *Phys. Rev. Lett.* 5 (1960), pp. 147–148. DOI: 10.1103/PhysRevLett.5.147.

[3] J. Bardeen, L. N. Cooper, and J. R. Schrieffer. "Theory of Superconductivity". In: *Phys. Rev.* 108 (1957), pp. 1175–1204. DOI: 10.1103/PhysRev.108.1175.

[4] L. Yu. "Bound State in Superconductors with Paramagnetic Impurities". In: *Acta Physica Sinica* 21 (1965), p. 75. DOI: 10.7498/aps.21.75.

[5] H. Shiba. "Classical Spins in Superconductors". In: *Prog. Theor. Phys.* 40 (1968), pp. 435–451. DOI: 10.1143/PTP.40.435.

[6] A. I. Rusinov. "On the Theory of Gapless Superconductivity in Alloys Containing Paramagnetic Impurities". In: *JETP Lett.* 29 (1969), p. 6. DOI: http://www.jetp.ras.ru/cgi-bin/e/index/e/29/6/p1101?a=list.

[7] A. Yazdani et al. "Probing the Local Effects of Magnetic Impurities on Superconductivity". In: *Science* 275 (1997), pp. 1767–1770. DOI: 10.1126/science.275.5307.1767.

[8] E. Majorana. "Teoria Simmetrica Dell'elettrone e Del Positrone". In: *Il Nuovo Cimento* 14 (1937), pp. 171–184. DOI: 10.1007/BF02961314.

[9] J. Alicea et al. "Non-Abelian Statistics and Topological Quantum Information Processing in 1D Wire Networks". In: *Nat. Phys.* 7 (2011), pp. 412–417. DOI: 10.1038/nphys1915.

[10] S. Nadj-Perge et al. "Proposal for Realizing Majorana Fermions in Chains of Magnetic Atoms on a Superconductor". In: *Phys. Rev. B* 88 (2013), p. 020407. DOI: 10.1103/PhysRevB.88.020407.

[11] M. Ruby et al. "Orbital Picture of Yu-Shiba-Rusinov Multiplets". In: *Phys. Rev. Lett.* 117 (2016), p. 186801. DOI: 10.1103/PhysRevLett.117.186801.

[12] G. C. Ménard et al. "Coherent Long-Range Magnetic Bound States in a Superconductor". In: *Nat. Phys.* 11 (2015), pp. 1013–1016. DOI: 10.1038/nphys3508.

[13] M. E. Flatté and D. E. Reynolds. "Local Spectrum of a Superconductor as a Probe of Interactions between Magnetic Impurities". In: *Phys. Rev. B* 61 (2000), pp. 14810–14814. DOI: 10.1103/PhysRevB.61.14810.

[14] H. Kim et al. “Long-Range Focusing of Magnetic Bound States in Superconducting Lanthanum”. In: *Nat. Commun.* 11 (2020), p. 4573. DOI: 10.1038/s41467-020-18406-8.

[15] E. Cortés-del Río et al. “Observation of Yu–Shiba–Rusinov States in Superconducting Graphene”. In: *Adv. Mater.* 33 (2021), p. 2008113. DOI: 10.1002/adma.202008113.

[16] E. Liebhaber et al. “Quantum Spins and Hybridization in Artificially-Constructed Chains of Magnetic Adatoms on a Superconductor”. In: *Nat. Commun.* 13 (2022), p. 2160. DOI: 10.1038/s41467-022-29879-0.

[17] J. Röntynen and T. Ojanen. “Topological Superconductivity and High Chern Numbers in 2D Ferromagnetic Shiba Lattices”. In: *Phys. Rev. Lett.* 114 (2015), p. 236803. DOI: 10.1103/PhysRevLett.114.236803.

[18] J. Ortuzar et al. “Yu-Shiba-Rusinov States in Two-Dimensional Superconductors with Arbitrary Fermi Contours”. In: *Phys. Rev. B* 105 (2022), p. 245403. DOI: 10.1103/PhysRevB.105.245403.

[19] A. J. Heinrich et al. “Single-Atom Spin-Flip Spectroscopy”. In: *Science* 306 (2004), pp. 466–469. DOI: 10.1126/science.1101077.

[20] P. Berggren and J. Fransson. “Spin Inelastic Electron Tunneling Spectroscopy on Local Magnetic Moment Embedded in Josephson Junction”. In: *EPL* 108 (2014), p. 67009. DOI: 10.1209/0295-5075/108/67009.

[21] P. Berggren and J. Fransson. “Theory of Spin Inelastic Tunneling Spectroscopy for Superconductor-Superconductor and Superconductor-Metal Junctions”. In: *Phys. Rev. B* 91 (2015), p. 205438. DOI: 10.1103/PhysRevB.91.205438.

[22] S. Kezilebieke et al. “Observation of Coexistence of Yu-Shiba-Rusinov States and Spin-Flip Excitations”. In: *Nano Letters* 19 (2019), pp. 4614–4619. DOI: 10.1021/acs.nanolett.9b01583.

[23] B. W. Heinrich et al. “Protection of Excited Spin States by a Superconducting Energy Gap”. In: *Nat. Phys.* 9 (2013), pp. 765–768. DOI: 10.1038/nphys2794.

[24] F. von Oppen and K. J. Franke. “Yu-Shiba-Rusinov States in Real Metals”. In: *Phys. Rev. B* 103 (2021), p. 205424. DOI: 10.1103/PhysRevB.103.205424.

[25] M. Hays et al. “Coherent Manipulation of an Andreev Spin Qubit”. In: *Science* 373 (2021), pp. 430–433. DOI: 10.1126/science.abf0345.

[26] F. J. Matute-Cañadas et al. “Signatures of Interactions in the Andreev Spectrum of Nanowire Josephson Junctions”. In: *Phys. Rev. Lett.* 128 (2022), p. 197702. DOI: 10.1103/PhysRevLett.128.197702.

[27] A. Andreev. “The Thermal Conductivity of the Intermediate State in Superconductors”. In: *JETP Lett.* 19 (1964), p. 1823.1828. DOI: http://jetp.ras.ru/cgi-bin/e/index/e/19/5/p1228?a=list.

[28] G. E. Blonder, M. Tinkham, and T. M. Klapwijk. "Transition from Metallic to Tunneling Regimes in Superconducting Microconstrictions: Excess Current, Charge Imbalance, and Supercurrent Conversion". In: *Phys. Rev. B* 25 (1982), pp. 4515–4532. DOI: 10.1103/PhysRevB.25.4515.

[29] T. M. Klapwijk. "Proximity Effect From an Andreev Perspective". In: *J. Supercond.* 17 (2004), pp. 593–611. DOI: 10.1007/s10948-004-0773-0.

[30] S. M. Albrecht et al. "Exponential Protection of Zero Modes in Majorana Islands". In: *Nature* 531 (2016), pp. 206–209. DOI: 10.1038/nature17162.

[31] S. Kezilebieke et al. "Topological Superconductivity in a van Der Waals Heterostructure". In: *Nature* 588 (2020), pp. 424–428. DOI: 10.1038/s41586-020-2989-y.

[32] J. Martinez-Castro et al. *One-Dimensional Topological Superconductivity in a van Der Waals Heterostructure*. 2023. arXiv: 2304.08142 [cond-mat].

[33] J. Li et al. "Uncovering the Triplet Ground State of Triangular Graphene Nanoflakes Engineered with Atomic Precision on a Metal Surface". In: *Phys. Rev. Lett.* 124 (2020), p. 177201. DOI: 10.1103/PhysRevLett.124.177201.

[34] P. San-Jose et al. "Majorana Zero Modes in Graphene". In: *Phys. Rev. X* 5 (2015), p. 041042. DOI: 10.1103/PhysRevX.5.041042.

[35] F. D. Natterer et al. "Scanning Tunneling Spectroscopy of Proximity Superconductivity in Epitaxial Multilayer Graphene". In: *Phys. Rev. B* 93 (2016), p. 045406. DOI: 10.1103/PhysRevB.93.045406.

[36] H. le Sueur et al. "Phase Controlled Superconducting Proximity Effect Probed by Tunneling Spectroscopy". In: *Phys. Rev. Lett.* 100 (2008), p. 197002. DOI: 10.1103/PhysRevLett.100.197002.

[37] J. Cuevas and E. Scheer. *Molecular Electronics An Introduction to Theory and Experiment*. Vol. 21. World Scientific Series in Nanoscience and Nanotechnology. 2021.

[38] C. Brun et al. "Dynamical Coulomb Blockade Observed in Nanosized Electrical Contacts". In: *Phys. Rev. Lett.* 108 (2012), p. 126802. DOI: 10.1103/PhysRevLett.108.126802.

[39] Z. Han et al. "Collapse of Superconductivity in a Hybrid Tin–Graphene Josephson Junction Array". In: *Nat. Phys.* 10 (2014), pp. 380–386. DOI: 10.1038/nphys2929.

[40] A. L. Efros and B. I. Shklovskii. "Coulomb Gap and Low Temperature Conductivity of Disordered Systems". In: *J. Phys. C: Solid State Phys.* 8 (1975), p. L49. DOI: 10.1088/0022-3719/8/4/003.

[41] A. E. Hanna and M. Tinkham. "Variation of the Coulomb Staircase in a Two-Junction System by Fractional Electron Charge". In: *Phys. Rev. B* 44 (1991), pp. 5919–5922. DOI: 10.1103/PhysRevB.44.5919.

[42] M. Amman et al. "Analytic Solution for the Current-Voltage Characteristic of Two Mesoscopic Tunnel Junctions Coupled in Series". In: *Phys. Rev. B* 43 (1991), pp. 1146–1149. DOI: 10.1103/PhysRevB.43.1146.

[43] I.-P. Hong et al. "Coulomb Blockade Phenomena Observed in Supported Metallic Nanoislands". In: *Front. Physics* 1 (2013), 13 (1–8). DOI: 10.3389/fphy.2013.00013.

[44] Y. Wang et al. "Scanning Tunneling Microscopy Study of the Superconducting Properties of Three-Atomic-Layer Pb Films". In: *Appl. Phys. Lett.* 103 (2013), p. 242603. DOI: 10.1063/1.4848219.

[45] H. K. Onnes. "Further Experiments with Liquid Helium". In: *KNAW* (1911), pp. 1093–1113. DOI: 10.1007/978-94-009-2079-8_15.

[46] W. Meissner and R. Ochsenfeld. "Ein Neuer Effekt Bei Eintritt Der Supraleitfähigkeit". In: *Naturwissenschaften* 21 (1933), p. 787.

[47] F. London. "A New Conception of Supraconductivity". In: *Nature* 140 (1937), pp. 793–796. DOI: 10.1038/140793a0.

[48] J. Bardeen. "Theory of the Meissner Effect in Superconductors". In: *Phys. Rev.* 97 (1955), pp. 1724–1725. DOI: 10.1103/PhysRev.97.1724.

[49] L. N. Cooper. "Bound Electron Pairs in a Degenerate Fermi Gas". In: *Phys. Rev.* 104 (1956), pp. 1189–1190. DOI: 10.1103/PhysRev.104.1189.

[50] Y. Nambu. "Quasi-Particles and Gauge Invariance in the Theory of Superconductivity". In: *Phys. Rev.* 117 (1960), pp. 648–663. DOI: 10.1103/PhysRev.117.648.

[51] P. Coleman. *Introduction to Many-Body Physics*. First. Cambridge University Press, 2015. DOI: 10.1017/CBO9781139020916.

[52] R. C. Dynes, V. Narayanamurti, and J. P. Garno. "Direct Measurement of Quasiparticle-Lifetime Broadening in a Strong-Coupled Superconductor". In: *Phys. Rev. Lett.* 41 (1978), pp. 1509–1512. DOI: 10.1103/PhysRevLett.41.1509.

[53] F. Herman and R. Hlubina. "Microscopic Interpretation of the Dynes Formula for the Tunneling Density of States". In: *Phys. Rev. B* 94 (2016), p. 144508. DOI: 10.1103/PhysRevB.94.144508.

[54] I. Affleck, J.-S. Caux, and A. M. Zagoskin. "Andreev Scattering and Josephson Current in a One-Dimensional Electron Liquid". In: *Phys. Rev. B* 62 (2000), pp. 1433–1445. DOI: 10.1103/PhysRevB.62.1433.

[55] G. Kiršanskas et al. "Yu-Shiba-Rusinov States in Phase-Biased Superconductor–Quantum Dot–Superconductor Junctions". In: *Phys. Rev. B* 92 (2015), p. 235422. DOI: 10.1103/PhysRevB.92.235422.

[56] B. W. Heinrich, J. I. Pascual, and K. J. Franke. "Single Magnetic Adsorbates on s -Wave Superconductors". In: *Prog. Surf. Sci.* 93 (2018), pp. 1–19. DOI: 10.1016/j.progsurf.2018.01.001.

[57] C. Rubio-Verdú et al. “Coupled Yu-Shiba-Rusinov States Induced by a Many-Body Molecular Spin on a Superconductor”. In: *Phys. Rev. Lett.* 126 (2021), p. 017001. DOI: 10.1103/PhysRevLett.126.017001.

[58] H. Huang et al. “Quantum Phase Transitions and the Role of Impurity-Substrate Hybridization in Yu-Shiba-Rusinov States”. In: *Commun. Phys.* 3 (2020), p. 199. DOI: 10.1038/s42005-020-00469-0.

[59] L. Schneider et al. “Precursors of Majorana Modes and Their Length-Dependent Energy Oscillations Probed at Both Ends of Atomic Shiba Chains”. In: *Nat. Nanotechnol.* 17 (2022), pp. 384–389. DOI: 10.1038/s41565-022-01078-4.

[60] A. V. Balatsky, I. Vekhter, and J.-X. Zhu. “Impurity-Induced States in Conventional and Unconventional Superconductors”. In: *Rev. Mod. Phys.* 78 (2006), pp. 373–433. DOI: 10.1103/RevModPhys.78.373.

[61] M. Ruby et al. “End States and Subgap Structure in Proximity-Coupled Chains of Magnetic Adatoms”. In: *Phys. Rev. Lett.* 115 (2015), p. 197204. DOI: 10.1103/PhysRevLett.115.197204.

[62] H. Huang et al. “Spin-Dependent Tunneling between Individual Superconducting Bound States”. In: *Phys. Rev. Research* 3 (2021), p. L032008. DOI: 10.1103/PhysRevResearch.3.L032008.

[63] G. Deutscher and P. G. de Gennes. “Proximity Effects”. In: *pp 1005-34 of Superconductivity. Vols. 1 and 2. Parks, R. D. (ed.). New York, Marcel Dekker, Inc.* (1969).

[64] J. Cuevas et al. “Proximity Effect A New Insight from In Situ Fabricated Hybrid Nanostructures”. In: *The Oxford Handbook of Small Superconductors*. Oxford University Press, 2017.

[65] B. Josephson. “Possible New Effects in Superconductive Tunnelling”. In: *Phys. Let.* 1 (1962), pp. 251–253. DOI: 10.1016/0031-9163(62)91369-0.

[66] K. D. Usadel. “Generalized Diffusion Equation for Superconducting Alloys”. In: *Phys. Rev. Lett.* 25 (1970), pp. 507–509. DOI: 10.1103/PhysRevLett.25.507.

[67] C. W. J. Beenakker. “Andreev Billiards”. In: vol. 667. 2005, pp. 131–174. DOI: 10.1007/11358817_4. arXiv: cond-mat/0406018.

[68] G. B. Arnold. “Theory of Thin Proximity-Effect Sandwiches”. In: *Phys. Rev. B* 18 (1978), pp. 1076–1100. DOI: 10.1103/PhysRevB.18.1076.

[69] W. L. McMillan. “Theory of Superconductor—Normal-Metal Interfaces”. In: *Phys. Rev.* 175 (1968), pp. 559–568. DOI: 10.1103/PhysRev.175.559.

[70] I. 0. Kulik. “Macroscopic Quantization and the Proximity Effect in S-N-S”. In: *JETP* 30 (1970), p. 1745.

[71] N. M. Chtchelkatchev and Y. V. Nazarov. “Andreev Quantum Dots for Spin Manipulation”. In: *Phys. Rev. Lett.* 90 (2003), p. 226806. DOI: 10.1103/PhysRevLett.90.226806.

[72] J. Rollbühler and H. Grabert. "Coulomb Blockade of Tunneling between Disordered Conductors". In: *Phys. Rev. Lett.* 87 (2001), p. 126804. DOI: 10.1103/PhysRevLett.87.126804.

[73] D. V. Averin, A. N. Korotkov, and K. K. Likharev. "Theory of Single-Electron Charging of Quantum Wells and Dots". In: *Phys. Rev. B* 44 (1991), pp. 6199–6211. DOI: 10.1103/PhysRevB.44.6199.

[74] L. Serrier-Garcia et al. "Scanning Tunneling Spectroscopy Study of the Proximity Effect in a Disordered Two-Dimensional Metal". In: *Phys. Rev. Lett.* 110 (2013), p. 157003. DOI: 10.1103/PhysRevLett.110.157003.

[75] H. Grabert, M. H. Devoret, and M. Kastner. "*Single Charge Tunneling: Coulomb Blockade Phenomena in Nanostructures*". In: *Physics Today* 46 (1993), pp. 62–63. DOI: 10.1063/1.2808874.

[76] J. Senkpiel et al. "Dynamical Coulomb Blockade as a Local Probe for Quantum Transport". In: *Phys. Rev. Lett.* 124 (2020), p. 156803. DOI: 10.1103/PhysRevLett.124.156803.

[77] Y. J. Song et al. "Invited Review Article: A 10 mK Scanning Probe Microscopy Facility". In: *Rev. Sci. Inst.* 81 (2010), p. 121101. DOI: 10.1063/1.3520482.

[78] C. Chen. *Introduction to Scanning Tunneling Microscopy Third Edition*. Monographs on the Physics and Chemistry of Materials Series. Oxford University Press, 2021.

[79] M. Ruby et al. "Tunneling Processes into Localized Subgap States in Superconductors". In: *Phys. Rev. Lett.* 115 (2015), p. 087001. DOI: 10.1103/PhysRevLett.115.087001.

[80] J.-D. Pillet et al. "Andreev Bound States in Supercurrent-Carrying Carbon Nanotubes Revealed". In: *Nat. Phys.* 6 (2010), pp. 965–969. DOI: 10.1038/nphys1811.

[81] K. J. Franke, G. Schulze, and J. I. Pascual. "Competition of Superconducting Phenomena and Kondo Screening at the Nanoscale". In: *Science* 332 (2011), pp. 940–944. DOI: 10.1126/science.1202204.

[82] W.-V. van Gerven Oei, D. Tanasković, and R. Žitko. "Magnetic Impurities in Spin-Split Superconductors". In: *Phys. Rev. B* 95 (2017), p. 085115. DOI: 10.1103/PhysRevB.95.085115.

[83] L. Cornils et al. "Spin-Resolved Spectroscopy of the Yu-Shiba-Rusinov States of Individual Atoms". In: *Phys. Rev. Lett.* 119 (2017), p. 197002. DOI: 10.1103/PhysRevLett.119.197002.

[84] D. Wang et al. "Spin-Polarized Yu-Shiba-Rusinov States in an Iron-Based Superconductor". In: *Phys. Rev. Lett.* 126 (2021), p. 076802. DOI: 10.1103/PhysRevLett.126.076802.

[85] S.-H. Ji et al. “High-Resolution Scanning Tunneling Spectroscopy of Magnetic Impurity Induced Bound States in the Superconducting Gap of Pb Thin Films”. In: *Phys. Rev. Lett.* 100 (2008), p. 226801. DOI: 10.1103/PhysRevLett.100.226801.

[86] D.-J. Choi et al. “Mapping the Orbital Structure of Impurity Bound States in a Superconductor”. In: *Nat. Commun.* 8 (2017), p. 15175. DOI: 10.1038/ncomms15175.

[87] F. Küster et al. “Correlating Josephson Supercurrents and Shiba States in Quantum Spins Unconventionally Coupled to Superconductors”. In: *Nat. Commun.* 12 (2021), p. 1108. DOI: 10.1038/s41467-021-21347-5.

[88] C. Rubio-Verdú et al. “Orbital-Selective Spin Excitation of a Magnetic Porphyrin”. In: *Commun. Phys.* 1 (2018), 15 (1–7). DOI: 10.1038/s42005-018-0015-6.

[89] D. K. Morr and N. A. Stavropoulos. “Quantum Interference between Impurities: Creating Novel Many-Body States in *s* -Wave Superconductors”. In: *Phys. Rev. B* 67 (2003), p. 020502. DOI: 10.1103/PhysRevB.67.020502.

[90] M. Ruby et al. “Wave-Function Hybridization in Yu-Shiba-Rusinov Dimers”. In: *Phys. Rev. Lett.* 120 (2018), p. 156803. DOI: 10.1103/PhysRevLett.120.156803.

[91] H. Ding et al. “Tuning Interactions between Spins in a Superconductor”. In: *Proc. Natl. Acad. Sci. U.S.A.* 118 (2021), e2024837118. DOI: 10.1073/pnas.2024837118.

[92] P. Beck et al. “Spin-Orbit Coupling Induced Splitting of Yu-Shiba-Rusinov States in Antiferromagnetic Dimers”. In: *Nat Commun* 12 (2021), p. 2040. DOI: 10.1038/s41467-021-22261-6.

[93] S. Nadj-Perge et al. “Observation of Majorana Fermions in Ferromagnetic Atomic Chains on a Superconductor”. In: *Science* 346 (2014), pp. 602–607. DOI: 10.1126/science.1259327.

[94] M. Ruby et al. “Experimental Demonstration of a Two-Band Superconducting State for Lead Using Scanning Tunneling Spectroscopy”. In: *Physical Review Letters* 114 (2015), p. 157001. DOI: 10.1103/PhysRevLett.114.157001. arXiv: 1409.6638.

[95] M. Ruby et al. “Exploring a Proximity-Coupled Co Chain on Pb(110) as a Possible Majorana Platform”. In: *Nano Lett.* 17 (2017), pp. 4473–4477. DOI: 10.1021/acs.nanolett.7b01728.

[96] K. Pöyhönen et al. “Amorphous Topological Superconductivity in a Shiba Glass”. In: *Nat. Commun.* 9 (2018), p. 2103. DOI: 10.1038/s41467-018-04532-x.

[97] A. Palacio-Morales et al. “Atomic-Scale Interface Engineering of Majorana Edge Modes in a 2D Magnet-Superconductor Hybrid System”. In: *Sci. Adv.* 5 (2019), p. 26. DOI: 10.1126/sciadv.aav6600.

[98] S. Manna et al. "Signature of a Pair of Majorana Zero Modes in Superconducting Gold Surface States". In: *Proc. Natl. Acad. Sci. U.S.A.* 117 (2020), pp. 8775–8782. DOI: 10.1073/pnas.1919753117.

[99] A. Kitaev. "Anyons in an Exactly Solved Model and Beyond". In: *Annals of Physics* 321 (2006), pp. 2–111. DOI: 10.1016/j.aop.2005.10.005.

[100] J. Li et al. "Topological Superconductivity Induced by Ferromagnetic Metal Chains". In: *Phys. Rev. B* 90 (2014), p. 235433. DOI: 10.1103/PhysRevB.90.235433.

[101] Y. Kim et al. "Helical Order in One-Dimensional Magnetic Atom Chains and Possible Emergence of Majorana Bound States". In: *Phys. Rev. B* 90 (2014), p. 060401. DOI: 10.1103/PhysRevB.90.060401.

[102] N. Y. Yao et al. "Enhanced Antiferromagnetic Exchange between Magnetic Impurities in a Superconducting Host". In: *Phys. Rev. Lett.* 113 (2014), p. 087202. DOI: 10.1103/PhysRevLett.113.087202.

[103] J. Li et al. "Two-Dimensional Chiral Topological Superconductivity in Shiba Lattices". In: *Nat. Commun.* 7 (2016), p. 12297. DOI: 10.1038/ncomms12297.

[104] J. Zaldivar. "Magnetic-Impurity-Induced Bound States in β-Bi2Pd". PhD thesis. UPV-EHU, 2020.

[105] M. Sakano et al. "Topologically Protected Surface States in a Centrosymmetric Superconductor β-PdBi2". In: *Nat. Commun.* 6 (2015), p. 8595. DOI: 10.1038/ncomms9595.

[106] Y. Imai et al. "Superconductivity at 5.4 K in β-Bi2Pd". In: *Journal of the Physical Society of Japan* 81 (2012), p. 113708. DOI: 10.1143/JPSJ.81.113708.

[107] E. Herrera et al. "Magnetic Field Dependence of the Density of States in the Multiband Superconductor β - Bi 2 Pd". In: *Phys. Rev. B* 92 (2015), p. 054507. DOI: 10.1103/PhysRevB.92.054507.

[108] L. Che et al. "Absence of Andreev Bound States in β - PdBi 2 Probed by Point-Contact Andreev Reflection Spectroscopy". In: *Phys. Rev. B* 94 (2016), p. 024519. DOI: 10.1103/PhysRevB.94.024519.

[109] J. Kačmarčík et al. "Single-Gap Superconductivity in β - Bi2Pd". In: *Physical Review B* 93 (2016), p. 144502. DOI: 10.1103/PhysRevB.93.144502.

[110] K. Iwaya et al. "Full-Gap Superconductivity in Spin-Polarised Surface States of Topological Semimetal β-PdBi2". In: *Nat. Commun.* 8 (2017), p. 8988. DOI: 10.1038/s41467-017-01209-9.

[111] A. Weismann et al. "Seeing the Fermi Surface in Real Space by Nanoscale Electron Focusing". In: *Science* 323 (2009), pp. 1190–1193. DOI: 10.1126/science.1168738.

[112] L. Schneider et al. "Topological Shiba Bands in Artificial Spin Chains on Superconductors". In: *Nat. Phys.* 17 (2021), pp. 943–948. DOI: 10.1038/s41567-021-01234-y.

[113] J. R. Schrieffer and P. A. Wolff. "Relation between the Anderson and Kondo Hamiltonians". In: *Phys. Rev.* 149 (1966), pp. 491–492. DOI: 10.1103/PhysRev.149.491.

[114] M. Ternes. "Spin Excitations and Correlations in Scanning Tunneling Spectroscopy". In: *New J. Phys.* 17 (2015), p. 063016. DOI: 10.1088/1367-2630/17/6/063016.

[115] F. Friedrich et al. "Coupling of Yu-Shiba-Rusinov States in One-Dimensional Chains of Fe Atoms on Nb(110)". In: *Phys. Rev. B* 103 (2021), p. 235437. DOI: 10.1103/PhysRevB.103.235437.

[116] A. Kamlapure et al. "Correlation of Yu–Shiba–Rusinov States and Kondo Resonances in Artificial Spin Arrays on an s-Wave Superconductor". In: *Nano Lett.* 21 (2021), pp. 6748–6755. DOI: 10.1021/acs.nanolett.1c00387.

[117] N. Ashcroft and N. Mermin. *Solid State Physics*. HRW International Editions. Holt, Rinehart and Winston, 1976.

[118] L. Farinacci et al. "Tuning the Coupling of an Individual Magnetic Impurity to a Superconductor: Quantum Phase Transition and Transport". In: *Phys. Rev. Lett.* 121 (2018), p. 196803. DOI: 10.1103/PhysRevLett.121.196803.

[119] D. Chatzopoulos et al. "Spatially Dispersing Yu-Shiba-Rusinov States in the Unconventional Superconductor FeTe0.55Se0.45". In: *Nat Commun* 12 (2021), p. 298. DOI: 10.1038/s41467-020-20529-x.

[120] C. Janvier et al. "Coherent Manipulation of Andreev States in Superconducting Atomic Contacts". In: *Science* 349 (2015), pp. 1199–1202. DOI: 10.1126/science.aab2179.

[121] S. Park et al. "Steady Floquet–Andreev States in Graphene Josephson Junctions". In: *Nature* 603 (2022), pp. 421–426. DOI: 10.1038/s41586-021-04364-8.

[122] A. M. van den Brink, G. Schön, and L. J. Geerligs. "Combined Single-Electron and Coherent-Cooper-pair Tunneling in Voltage-Biased Josephson Junctions". In: *Phys. Rev. Lett.* 67 (1991), pp. 3030–3033. DOI: 10.1103/PhysRevLett.67.3030.

[123] L. Bretheau et al. "Exciting Andreev Pairs in a Superconducting Atomic Contact". In: *Nature* 499 (2013), pp. 312–315. DOI: 10.1038/nature12315. arXiv: 1305.4091.

[124] R. E. Glover and M. Tinkham. "Transmission of Superconducting Films at Millimeter-Microwave and Far Infrared Frequencies". In: *Phys. Rev.* 104 (1956), pp. 844–845. DOI: 10.1103/PhysRev.104.844.

[125] E. T. Mannila et al. "A Superconductor Free of Quasiparticles for Seconds". In: *Nat. Phys.* 18 (2022), pp. 145–148. DOI: 10.1038/s41567-021-01433-7.

[126] I. Horcas et al. "WSXM: A Software for Scanning Probe Microscopy and a Tool for Nanotechnology". In: *Rev. Sci. Inst.* 78 (2007), p. 013705.

[127] M. Ruby. "SpectraFox: A Free Open-Source Data Management and Analysis Tool for Scanning Probe Microscopy and Spectroscopy". In: *SoftwareX.* 5 (2016), pp. 31–36.

[128] T. Matsuura. "The Effects of Impurities on Superconductors with Kondo Effect". In: *Prog. Theor. Phys.* 57 (1977), pp. 1823–1835. DOI: 10.1143/PTP.57.1823.

[129] N. Hatter et al. "Magnetic Anisotropy in Shiba Bound States across a Quantum Phase Transition". In: *Nat. Commun.* 6 (2015), p. 8988. DOI: 10.1038/ncomms9988.

[130] L. Malavolti et al. "Tunable Spin-Superconductor Coupling of Spin 1/2 Vanadyl Phthalocyanine Molecules". In: *Nano Lett.* 18 (2018), pp. 7955–7961. DOI: 10.1021/acs.nanolett.8b03921.

[131] R. Koller et al. "The Structure of the Oxygen Induced (1×5) Reconstruction of V(100)". In: *Surf. Sci.* 480 (2001), pp. 11–24. DOI: 10.1016/S0039-6028(01)00978-5.

[132] F. Dulot et al. "(001) V Surface Structures Analysed by RHEED and STM". In: *Surf. Sci.* 473 (2001), pp. 172–182. DOI: 10.1016/S0039-6028(00)00972-9.

[133] M. Etzkorn et al. "Mapping of Yu-Shiba-Rusinov States from an Extended Scatterer". In: (2018). arXiv: 1807.00646.

[134] S. Karan et al. "Superconducting Quantum Interference at the Atomic Scale". In: *Nat. Phys.* 18 (2022), pp. 893–898. DOI: 10.1038/s41567-022-01644-6.

[135] H. Huang et al. "Tunnelling Dynamics between Superconducting Bound States at the Atomic Limit". In: *Nature Physics* 16 (2020), pp. 1227–1231. DOI: 10.1038/s41567-020-0971-0.

[136] R. Hammer et al. "Surface Reconstruction of Au(001): High-resolution Real-Space and Reciprocal-Space Inspection". In: *Phys. Rev. B* 90 (2014), p. 035446. DOI: 10.1103/PhysRevB.90.035446.

[137] Y.-F. Liew and G.-C. Wang. "High Resolution Low Energy Electron Diffraction Characterization of Reconstructed Au(001) Surfaces". In: *Surf. Sci.* 227 (1990), pp. 190–196. DOI: 10.1016/S0039-6028(05)80006-8.

[138] E. Hüger, H. Wormeester, and K. Osuch. "Subsurface Miscibility of Metal Overlayers with V, Nb and Ta Substrates". In: *Surf. Sci.* 580 (2005), pp. 173–194. DOI: 10.1016/j.susc.2005.01.055.

[139] J. O. Island et al. "Proximity-Induced Shiba States in a Molecular Junction". In: *Phys. Rev. Lett.* 118 (2017), p. 117001. DOI: 10.1103/PhysRevLett.118.117001.

[140] P. de Gennes and D. Saint-James. "Elementary Excitations in the Vicinity of a Normal Metal-Superconducting Metal Contact". In: *Phys. Let.* 4 (1963), pp. 151–152. DOI: 10.1016/0031-9163(63)90148-3.

[141] E. Wolf and G. Arnold. "Proximity Electron Tunneling Spectroscopy". In: *Physics Reports* 91 (1982), pp. 31–102. DOI: 10.1016/0370-1573(82)90061-8.

[142] G. Kieselmann. "Self-Consistent Calculations of the Pair Potential and the Tunneling Density of States in Proximity Contacts". In: *Phys. Rev. B* 35 (1987), p. 6762. DOI: 10.1103/PhysRevB.35.6762.

[143] A. D. Truscott, R. C. Dynes, and L. F. Schneemeyer. "Scanning Tunneling Spectroscopy of $NbSe_2$-Au Proximity Junctions". In: *Phys. Rev. Lett.* 83 (1999), pp. 1014–1017. DOI: 10.1103/PhysRevLett.83.1014.

[144] K. Vaxevani et al. "Extending the Spin Excitation Lifetime of a Magnetic Molecule on a Proximitized Superconductor". In: *Nano Lett.* 22 (2022), pp. 6075–6082. DOI: 10.1021/acs.nanolett.2c00924.

[145] B. W. Heinrich et al. "Tuning the Magnetic Anisotropy of Single Molecules". In: *Nano Letters* 15 (2015), pp. 4024–4028. DOI: 10.1021/acs.nanolett.5b00987.

[146] L. Farinacci et al. "Interfering Tunneling Paths through Magnetic Molecules on Superconductors: Asymmetries of Kondo and Yu-Shiba-Rusinov Resonances". In: *arXiv:2007.12092 [cond-mat]* (2020). arXiv: 2007.12092 [cond-mat].

[147] E. Vecino, A. Martín-Rodero, and A. L. Yeyati. "Josephson Current through a Correlated Quantum Level: Andreev States and π Junction Behavior". In: *Phys. Rev. B* 68 (2003), p. 035105. DOI: 10.1103/PhysRevB.68.035105.

[148] H. Schmid et al. "Quantum Yu-Shiba-Rusinov Dimers". In: *Phys. Rev. B* 105 (2022), p. 235406. DOI: 10.1103/PhysRevB.105.235406.

[149] R. Žitko, R. Peters, and T. Pruschke. "Properties of Anisotropic Magnetic Impurities on Surfaces". In: *Phys. Rev. B* 78 (2008), p. 224404. DOI: 10.1103/PhysRevB.78.224404.

[150] R. žitko, O. Bodensiek, and T. Pruschke. "Effects of Magnetic Anisotropy on the Subgap Excitations Induced by Quantum Impurities in a Superconducting Host". In: *Phys. Rev. B* 83 (2011), p. 054512. DOI: 10.1103/PhysRevB.83.054512.

[151] J. Homberg et al. "Resonance-Enhanced Vibrational Spectroscopy of Molecules on a Superconductor". In: *Phys. Rev. Lett.* 129 (2022), p. 116801. DOI: 10.1103/PhysRevLett.129.116801.

[152] M. Tinkham. *Introduction to Superconductivity*. Second. Dover Publications, 2004.

[153] S. Guéron et al. "Superconducting Proximity Effect Probed on a Mesoscopic Length Scale". In: *Phys. Rev. Lett.* 77 (1996), pp. 3025–3028. DOI: 10.1103/PhysRevLett.77.3025.

[154] A. I. Buzdin. "Proximity Effects in Superconductor-Ferromagnet Heterostructures". In: *Rev. Mod. Phys.* 77 (2005), p. 935. DOI: 10.1103/RevModPhys.77.935.

[155] A. Hijano et al. “Coexistence of Superconductivity and Spin-Splitting Fields in Superconductor/Ferromagnetic Insulator Bilayers of Arbitrary Thickness”. In: *Phys. Rev. Research* 3 (2021), p. 023131. DOI: 10.1103/PhysRevResearch.3.023131.

[156] L. Fu and C. L. Kane. “Superconducting Proximity Effect and Majorana Fermions at the Surface of a Topological Insulator”. In: *Phys. Rev. Lett.* 100 (2008), p. 096407. DOI: 10.1103/PhysRevLett.100.096407.

[157] V. S. Stolyarov et al. “Superconducting Long-Range Proximity Effect through the Atomically Flat Interface of a Bi $_2$ Te $_3$ Topological Insulator”. In: *J. Phys. Chem. Lett.* 12 (2021), pp. 9068–9075. DOI: 10.1021/acs.jpclett.1c02257.

[158] P. Dreher et al. “Proximity Effects on the Charge Density Wave Order and Superconductivity in Single-Layer NbSe $_2$”. In: *ACS Nano* 15 (2021), pp. 19430–19438. DOI: 10.1021/acsnano.1c06012.

[159] S. Kezilebieke et al. “Moiré-Enabled Topological Superconductivity”. In: *Nano Lett.* 22 (2022), pp. 328–333. DOI: 10.1021/acs.nanolett.1c03856.

[160] W. Wan et al. “Observation of Superconducting Collective Modes from Competing Pairing Instabilities in Single-Layer NbSe $_2$”. In: *Adv. Mater.* 34 (2022), p. 2206078. DOI: 10.1002/adma.202206078.

[161] A. Golubov and M. Kupriyanov. “Quasiparticle Current in Ballistic NcN′S Junctions”. In: *Physica C: Superconductivity and its Applications* 259 (1996), pp. 27–35. DOI: 10.1016/0921-4534(96)00013-5.

[162] J. M. Martinis et al. “Rabi Oscillations in a Large Josephson-Junction Qubit”. In: *Phys. Rev. Lett.* 89 (2002), p. 117901. DOI: 10.1103/PhysRevLett.89.117901.

[163] X. Du, I. Skachko, and E. Y. Andrei. “Josephson Current and Multiple Andreev Reflections in Graphene SNS Junctions”. In: *Phys. Rev. B* 77 (2008), p. 184507. DOI: 10.1103/PhysRevB.77.184507.

[164] T. Dirks et al. “Transport through Andreev Bound States in a Graphene Quantum Dot”. In: *Nat. Phys.* 7 (2011), pp. 386–390. DOI: 10.1038/nphys1911.

[165] B. Dassonneville et al. “Coherence-Enhanced Phase-Dependent Dissipation in Long SNS Josephson Junctions: Revealing Andreev Bound State Dynamics”. In: *Phys. Rev. B* 97 (2018), p. 184505. DOI: 10.1103/PhysRevB.97.184505.

[166] J. Kim et al. “Visualization of Geometric Influences on Proximity Effects in Heterogeneous Superconductor Thin Films”. In: *Nat. Phys.* 8 (2012), pp. 464–469. DOI: 10.1038/nphys2287.

[167] K. S. Novoselov et al. “Electric Field Effect in Atomically Thin Carbon Films”. In: *Science* 306 (2004), pp. 666–669. DOI: 10.1126/science.1102896.

[168] A. K. Geim and K. S. Novoselov. “The Rise of Graphene”. In: *Nat. Mater.* 6 (2007), pp. 183–191. DOI: 10.1038/nmat1849.

[169] H. B. Heersche et al. “Induced Superconductivity in Graphene”. In: *Solid State Commun.* 143 (2007), pp. 72–76. DOI: 10.1016/j.ssc.2007.02.044.

[170] F. Miao et al. “Phase-Coherent Transport in Graphene Quantum Billiards”. In: *Science* 317 (2007), pp. 1530–1533. DOI: 10.1126/science.1144359.

[171] G. Profeta, M. Calandra, and F. Mauri. “Phonon-Mediated Superconductivity in Graphene by Lithium Deposition”. In: *Nat. Phys.* 8 (2012), pp. 131–134. DOI: 10.1038/nphys2181.

[172] C. W. J. Beenakker. “*Colloquium* : Andreev Reflection and Klein Tunneling in Graphene”. In: *Rev. Mod. Phys.* 80 (2008), pp. 1337–1354. DOI: 10.1103/RevModPhys.80.1337.

[173] C. W. J. Beenakker et al. “Correspondence between Andreev Reflection and Klein Tunneling in Bipolar Graphene”. In: *Phys. Rev. B* 77 (2008), p. 075409. DOI: 10.1103/PhysRevB.77.075409.

[174] L. Bretheau et al. “Tunnelling Spectroscopy of Andreev States in Graphene”. In: *Nat. Phys.* 13 (2017), pp. 756–760. DOI: 10.1038/nphys4110.

[175] G.-H. Lee and H.-J. Lee. “Proximity Coupling in Superconductor-Graphene Heterostructures”. In: *Rep. Prog. Phys.* 81 (2018), p. 056502. DOI: 10.1088/1361-6633/aaafe1.

[176] W. Norimatsu and M. Kusunoki. “Epitaxial Graphene on SiC{0001}: Advances and Perspectives”. In: *Phys. Chem. Chem. Phys.* 16 (2014), p. 3501. DOI: 10.1039/c3cp54523g.

[177] F. Varchon et al. “Rotational Disorder in Few-Layer Graphene Films on 6 H - Si C (000 - 1) : A Scanning Tunneling Microscopy Study”. In: *Phys. Rev. B* 77 (2008), p. 165415. DOI: 10.1103/PhysRevB.77.165415.

[178] T. Quang. “Low-Temperature Scanning Tunneling Spectroscopy of Epitaxial Graphene Grown on SiC”. PhD thesis. Université Grenoble Alpes, 2016.

[179] I. Brihuega et al. “Unraveling the Intrinsic and Robust Nature of van Hove Singularities in Twisted Bilayer Graphene by Scanning Tunneling Microscopy and Theoretical Analysis”. In: *Phys. Rev. Lett.* 109 (2012), p. 196802. DOI: 10.1103/PhysRevLett.109.196802.

[180] J. Hass et al. “Why Multilayer Graphene on 4 H - SiC (000 1 $^{-}$) Behaves Like a Single Sheet of Graphene”. In: *Phys. Rev. Lett.* 100 (2008), p. 125504. DOI: 10.1103/PhysRevLett.100.125504.

[181] Y. Cao et al. “Unconventional Superconductivity in Magic-Angle Graphene Superlattices”. In: *Nature* 556 (2018), pp. 43–50. DOI: 10.1038/nature26160.

[182] S. Kezilebieke et al. “Moiré-Enabled Topological Superconductivity”. In: *Nano Lett.* 22 (2022), pp. 328–333. DOI: 10.1021/acs.nanolett.1c03856.

[183] X. Fei et al. “Tuning the Proximity Effect through Interface Engineering in a Pb/Graphene/Pt Trilayer System”. In: *ACS Nano* 10 (2016), pp. 4520–4524. DOI: 10.1021/acsnano.6b00298.

[184] L. A. Gonzalez-Arraga et al. “Electrically Controllable Magnetism in Twisted Bilayer Graphene”. In: *Phys. Rev. Lett.* 119 (2017), p. 107201. DOI: 10.1103/PhysRevLett.119.107201.

[185] J. Liu and X. Dai. “Orbital Magnetic States in Moiré Graphene Systems”. In: *Nat. Rev. Phys.* 3 (2021), pp. 367–382. DOI: 10.1038/s42254-021-00297-3.

[186] H. Shi et al. “Large-Area, Periodic, and Tunable Intrinsic Pseudo-Magnetic Fields in Low-Angle Twisted Bilayer Graphene”. In: *Nat. Commun.* 11 (2020), p. 371. DOI: 10.1038/s41467-019-14207-w.

[187] S. Latil, V. Meunier, and L. Henrard. “Massless Fermions in Multilayer Graphitic Systems with Misoriented Layers: *Ab Initio* Calculations and Experimental Fingerprints”. In: *Phys. Rev. B* 76 (2007), p. 201402. DOI: 10.1103/PhysRevB.76.201402.

[188] K. Uchida et al. “Atomic Corrugation and Electron Localization Due to Moiré Patterns in Twisted Bilayer Graphenes”. In: *Phys. Rev. B* 90 (2014), p. 155451. DOI: 10.1103/PhysRevB.90.155451.

[189] F. Wu, A. H. MacDonald, and I. Martin. “Theory of Phonon-Mediated Superconductivity in Twisted Bilayer Graphene”. In: *Phys. Rev. Lett.* 121 (2018), p. 257001. DOI: 10.1103/PhysRevLett.121.257001.

[190] J. H. Durrell et al. “The Behavior of Grain Boundaries in the Fe-based Superconductors”. In: *Rep. Prog. Phys.* 74 (2011), p. 124511. DOI: 10.1088/0034-4885/74/12/124511.

[191] J. Sun et al. “Electronic and Transport Properties of Graphene with Grain Boundaries”. In: *RSC Adv.* 6 (2016), pp. 1090–1097. DOI: 10.1039/C5RA16323D.

[192] D. Dimos et al. “Orientation Dependence of Grain-Boundary Critical Currents in Y Ba 2 Cu 3 O 7 - δ Bicrystals”. In: *Phys. Rev. Lett.* 61 (1988), pp. 219–222. DOI: 10.1103/PhysRevLett.61.219.

[193] T. Katase et al. “Advantageous Grain Boundaries in Iron Pnictide Superconductors”. In: *Nat. Commun.* 2 (2011), p. 409. DOI: 10.1038/ncomms1419.

[194] S. Graser et al. “How Grain Boundaries Limit Supercurrents in High-Temperature Superconductors”. In: *Nat. Phys.* 6 (2010), pp. 609–614. DOI: 10.1038/nphys1687.

[195] S. Lee et al. “Weak-Link Behavior of Grain Boundaries in Superconducting Ba(Fe1-xCox)2As2 Bicrystals”. In: *Appl. Phys. Lett.* 95 (2009), p. 212505. DOI: 10.1063/1.3262953.

[196] A. H. Castro Neto et al. “The Electronic Properties of Graphene”. In: *Rev. Mod. Phys.* 81 (2009), pp. 109–162. DOI: 10.1103/RevModPhys.81.109.

[197] O. Naaman and R. Dynes. “Subharmonic Gap Structure in Superconducting Scanning Tunneling Microscope Junctions”. In: *Solid State Commun.* 129 (2004), pp. 299–303. DOI: 10.1016/j.ssc.2003.10.022.

[198] A. Villas et al. “Interplay Between Yu-Shiba-Rusinov States and Multiple Andreev Reflections”. In: *Phys. Rev. B* 101 (2020), p. 235445. DOI: 10.1103/PhysRevB.101.235445. arXiv: 2005.06491.

[199] C. R. Ast et al. “Sensing the Quantum Limit in Scanning Tunnelling Spectroscopy”. In: *Nat. Commun.* 7 (2016), p. 13009. DOI: 10.1038/ncomms13009.

[200] X. Liu et al. “Atomic-Scale Visualization of Electronic Fluid Flow”. In: *Nat. Mater.* 20 (2021), pp. 1480–1484. DOI: 10.1038/s41563-021-01077-1.

[201] M. Trahms et al. “Diode Effect in Josephson Junctions with a Single Magnetic Atom”. In: *Nature* (2023). DOI: 10.1038/s41586-023-05743-z.

[202] M. Ternes et al. “Subgap Structure in Asymmetric Superconducting Tunnel Junctions”. In: *Phys. Rev. B* 74 (2006), p. 132501. DOI: 10.1103/PhysRevB.74.132501.

[203] A. Nakayama. “Wave Functions of Andreev Bound States in Superconductor/Normal-Metal/Superconductor Junctions”. In: *J. Appl. Phys.* 91 (2002), p. 7119. DOI: 10.1063/1.1448784.

[204] N. A. Stavropoulos and D. K. Morr. “Quantum Imaging and Selection Rules in Triangular Quantum Corrals”. In: *Phys. Rev. B* 71 (2005), p. 140501. DOI: 10.1103/PhysRevB.71.140501.

[205] J. C. Cuevas and A. L. Yeyati. “Subharmonic Gap Structure in Short Ballistic Graphene Junctions”. In: *Phys. Rev. B* 74 (2006), p. 180501. DOI: 10.1103/PhysRevB.74.180501.

[206] A. Gabovich, A. Voitenko, and M. Ausloos. “Charge- and Spin-Density Waves in Existing Superconductors: Competition between Cooper Pairing and Peierls or Excitonic Instabilities”. In: *Physics Reports* 367 (2002), pp. 583–709. DOI: 10.1016/S0370-1573(02)00029-7.

[207] M. H. Hamidian et al. “Detection of a Cooper-pair Density Wave in Bi2Sr2CaCu2O8+x”. In: *Nature* 532 (2016), pp. 343–347. DOI: 10.1038/nature17411.

[208] W. Ruan et al. “Visualization of the Periodic Modulation of Cooper Pairing in a Cuprate Superconductor”. In: *Nat. Phys.* 14 (2018), pp. 1178–1182. DOI: 10.1038/s41567-018-0276-8.

[209] X. Liu et al. “Discovery of a Cooper-pair Density Wave State in a Transition-Metal Dichalcogenide”. In: *Science* 372 (2021), pp. 1447–1452. DOI: 10.1126/science.abd4607. eprint: https://www.science.org/doi/pdf/10.1126/science.abd4607.

[210] D. Cho et al. “A Strongly Inhomogeneous Superfluid in an Iron-Based Superconductor”. In: *Nature* 571 (2019), pp. 541–545. DOI: 10.1038/s41586-019-1408-8.

[211] V. J. Emery and S. A. Kivelson. “Importance of Phase Fluctuations in Superconductors with Small Superfluid Density”. In: *Nature* 374 (1995), pp. 434–437. DOI: 10.1038/374434a0.

[212] Y. Dubi, Y. Meir, and Y. Avishai. “Nature of the Superconductor–Insulator Transition in Disordered Superconductors”. In: *Nature* 449 (2007), pp. 876–880. DOI: 10.1038/nature06180.

[213] M. F. Crommie, C. P. Lutz, and D. M. Eigler. "Confinement of Electrons to Quantum Corrals on a Metal Surface". In: *Science* 262 (1993), pp. 218–220. DOI: 10.1126/science.262.5131.218.

[214] G. A. Fiete and E. J. Heller. "*Colloquium* : Theory of Quantum Corrals and Quantum Mirages". In: *Rev. Mod. Phys.* 75 (2003), pp. 933–948. DOI: 10.1103/RevModPhys.75.933.

[215] G. Nanda et al. "Current-Phase Relation of Ballistic Graphene Josephson Junctions". In: *Nano Lett.* 17 (2017), pp. 3396–3401. DOI: 10.1021/acs.nanolett.7b00097.

[216] D. I. Indolese et al. "Compact SQUID Realized in a Double-Layer Graphene Heterostructure". In: *Nano Lett.* 20 (2020), pp. 7129–7135. DOI: 10.1021/acs.nanolett.0c02412.

[217] J. Clarke. "Squid Fundamentals". In: *SQUID Sensors: Fundamentals, Fabrication and Applications*. Ed. by H. Weinstock. Dordrecht: Springer Netherlands, 1996, pp. 1–62. DOI: 10.1007/978-94-011-5674-5_1.

[218] E. Grosfeld and A. Stern. "Observing Majorana Bound States of Josephson Vortices in Topological Superconductors". In: *Proc. Natl. Acad. Sci. U.S.A.* 108 (2011), pp. 11810–11814. DOI: 10.1073/pnas.1101469108.

[219] D. Wang et al. "Evidence for Majorana Bound States in an Iron-Based Superconductor". In: *Science* 362 (2018), pp. 333–335. DOI: 10.1126/science.aao1797.

[220] T. Cren et al. "Ultimate Vortex Confinement Studied by Scanning Tunneling Spectroscopy". In: *Phys. Rev. Lett.* 102 (2009), p. 127005. DOI: 10.1103/PhysRevLett.102.127005.

[221] T. Cren et al. "Vortex Fusion and Giant Vortex States in Confined Superconducting Condensates". In: *Phys. Rev. Lett.* 107 (2011), p. 097202. DOI: 10.1103/PhysRevLett.107.097202.

[222] J. Barba-Ortega, E. Sardella, and J. A. Aguiar. "Superconducting Boundary Conditions for Mesoscopic Circular Samples". In: *Supercond. Sci. Technol.* 24 (2011), p. 015001. DOI: 10.1088/0953-2048/24/1/015001.

[223] J. R. Kirtley et al. "Direct Imaging of Integer and Half-Integer Josephson Vortices in High- T c Grain Boundaries". In: *Phys. Rev. Lett.* 76 (1996), pp. 1336–1339. DOI: 10.1103/PhysRevLett.76.1336.

[224] R. G. Mints et al. "Observation of Splintered Josephson Vortices at Grain Boundaries in Y B a 2 C u 3 O 7 - δ". In: *Phys. Rev. Lett.* 89 (2002), p. 067004. DOI: 10.1103/PhysRevLett.89.067004.

[225] D. Roditchev et al. "Direct Observation of Josephson Vortex Cores". In: *Nat. Phys.* 11 (2015), pp. 332–337. DOI: 10.1038/nphys3240.

[226] I. Guillamon et al. "Scanning Tunneling Microscopy and Spectroscopy at Very Low Temperatures". In: *J. Phys.: Conf. Ser.* 568 (2014), p. 022045. DOI: 10.1088/1742-6596/568/2/022045.

[227] R. Boyer and M. A. R. LeBlanc. "Flux Expulsion and Trapping in Rotating Discs of Type II Superconductors". In: *Solid State Commun.* 24 (1977), pp. 261–265. DOI: 10.1016/0038-1098(77)91210-8.

[228] F. Loder et al. "Magnetic Flux Periodicity of h/e in Superconducting Loops". In: *Nat. Phys.* 4 (2008), pp. 112–115. DOI: 10.1038/nphys813.

[229] R. Monaco et al. "Spontaneous Fluxoid Formation in Superconducting Loops". In: *Phys. Rev. B* 80 (2009), p. 180501. DOI: 10.1103/PhysRevB.80.180501.

[230] R. Doll and M. Näbauer. "Experimental Proof of Magnetic Flux Quantization in a Superconducting Ring". In: *Phys. Rev. Lett.* 7 (1961), pp. 51–52. DOI: 10.1103/PhysRevLett.7.51.

[231] A. Abrikosov. "On the Magnetic Properties of Superconductors of the Second Group". In: *JETP* 5 (1957), p. 1174. DOI: http://jetp.ras.ru/cgi-bin/e/index/e/5/6/p1174?a=list.

[232] C. Caroli, P. De Gennes, and J. Matricon. "Bound Fermion States on a Vortex Line in a Type II Superconductor". In: *Physics Letters* 9 (1964), pp. 307–309. DOI: 10.1016/0031-9163(64)90375-0.

[233] S. H. Pan, E. W. Hudson, and A. K. Gupta. "STM Studies of the Electronic Structure of Vortex Cores in Bi2Sr2CaCu2O81d". In: *Phys. Rev. Lett.* 85 (2000), p. 1536.

[234] T. Hanaguri et al. "Scanning Tunneling Microscopy/Spectroscopy of Vortices in LiFeAs". In: *Phys. Rev. B* 85 (2012), p. 214505. DOI: 10.1103/PhysRevB.85.214505.

[235] M. Chen et al. "Discrete Energy Levels of Caroli-de Gennes-Matricon States in Quantum Limit in FeTe0.55Se0.45". In: *Nat Commun* 9 (2018), p. 970. DOI: 10.1038/s41467-018-03404-8.

[236] S. C. Ganguli et al. "Confinement-Engineered Superconductor to Correlated-Insulator Transition in a van Der Waals Monolayer". In: *Nano Lett.* 22 (2022), pp. 1845–1850. DOI: 10.1021/acs.nanolett.1c03491.

[237] M. V. Feigel'man, M. A. Skvortsov, and K. S. Tikhonov. "Proximity-Induced Superconductivity in Graphene". In: *JETP Lett.* 88 (2008), pp. 747–751. DOI: 10.1134/S0021364008230100.

[238] M. Feigel'man and A. Larkin. "Quantum Superconductor–Metal Transition in a 2D Proximity-Coupled Array". In: *Chemical Physics* 235 (1998), pp. 107–114. DOI: 10.1016/S0301-0104(98)00075-5.

[239] A. Allain, Z. Han, and V. Bouchiat. "Electrical Control of the Superconducting-to-Insulating Transition in Graphene–Metal Hybrids". In: *Nature Mater* 11 (2012), pp. 590–594. DOI: 10.1038/nmat3335.

[240] W. Wang et al. "Local Transport Measurements at Mesoscopic Length Scales Using Scanning Tunneling Potentiometry". In: *Phys. Rev. Lett.* 110 (2013), p. 236802. DOI: 10.1103/PhysRevLett.110.236802.

[241] T. Shen et al. “Observation of Quantum-Hall Effect in Gated Epitaxial Graphene Grown on SiC (0001)”. In: *Appl. Phys. Lett.* 95 (2009), p. 172105. DOI: 10.1063/1.3254329.

[242] D. Momeni Pakdehi et al. “Minimum Resistance Anisotropy of Epitaxial Graphene on SiC”. In: *ACS Appl. Mater. Interfaces* 10 (2018), pp. 6039–6045. DOI: 10.1021/acsami.7b18641.

[243] H. S. J. van der Zant et al. “Field-Induced Superconductor-to-Insulator Transitions in Josephson-junction Arrays”. In: *Phys. Rev. Lett.* 69 (1992), pp. 2971–2974. DOI: 10.1103/PhysRevLett.69.2971.

[244] H. S. J. van der Zant et al. “Quantum Phase Transitions in Two Dimensions: Experiments in Josephson-junction Arrays”. In: *Phys. Rev. B* 54 (1996), pp. 10081–10093. DOI: 10.1103/PhysRevB.54.10081.

[245] M. V. Feigelman et al. “Weak Charge Quantization on a Superconducting Island”. In: *Phys. Rev. B* 66 (2002), p. 054502. DOI: 10.1103/PhysRevB.66.054502.

[246] B. M. Kessler et al. “Tunable Superconducting Phase Transition in Metal-Decorated Graphene Sheets”. In: *Phys. Rev. Lett.* 104 (2010), p. 047001. DOI: 10.1103/PhysRevLett.104.047001.

[247] C. Ebner and D. Stroud. “Diamagnetic Susceptibility of Superconducting Clusters: Spin-glass Behavior”. In: *Phys. Rev. B* 31 (1985), pp. 165–171. DOI: 10.1103/PhysRevB.31.165.

[248] P. W. Anderson. “Theory of Dirty Superconductors”. In: *J. Phys. Chem. Solids* 11 (1959), pp. 26–30. DOI: 10.1016/0022-3697(59)90036-8.

[249] R. Kubo. “Electronic Properties of Metallic Fine Particles”. In: *JPSJ* 17 (1962), p. 975. DOI: 10.1143/JPSJ.17.975.

[250] F. Lamberti et al. “High-Quality, Ligands-Free, Mixed-Halide Perovskite Nanocrystals Inks for Optoelectronic Applications”. In: *Adv. Energy Mater.* 7 (2017), p. 1601703. DOI: 10.1002/aenm.201601703.

[251] D. V. Averin and Y. V. Nazarov. “Single-Electron Charging of a Superconducting Island”. In: *Phys. Rev. Lett.* 69 (1992), pp. 1993–1996. DOI: 10.1103/PhysRevLett.69.1993.

[252] A. M. van den Brink et al. “Coherent Cooper Pair Tunneling in Systems of Josephson Junctions: Effects of Quasiparticle Tunneling and of the Electromagnetic Environment”. In: *Z. Physik B - Condensed Matter* 85 (1991), pp. 459–467. DOI: 10.1007/BF01307644.

[253] T. M. Eiles, J. M. Martinis, and M. H. Devoret. “Even-Odd Asymmetry of a Superconductor Revealed by the Coulomb Blockade of Andreev Reflection”. In: *Phys. Rev. Lett.* 70 (1993), pp. 1862–1865. DOI: 10.1103/PhysRevLett.70.1862.

[254] J. Shen et al. “Parity Transitions in the Superconducting Ground State of Hybrid InSb–Al Coulomb Islands”. In: *Nat. Commun.* 9 (2018), p. 4801. DOI: 10.1038/s41467-018-07279-7.

[255] J. C. Estrada Saldaña et al. “Excitations in a Superconducting Coulombic Energy Gap”. In: *Nat. Commun.* 13 (2022), p. 2243. DOI: 10.1038/s41467-022-29634-5.

[256] Y. Yuan et al. “Observation of Coulomb Gap and Enhanced Superconducting Gap in Nano-Sized Pb Islands Grown on $SrTiO_3$”. In: *Chinese Phys. Lett.* 37 (2020), p. 017402. DOI: 10.1088/0256-307X/37/1/017402.

[257] S. Vlaic et al. “Superconducting Parity Effect across the Anderson Limit”. In: *Nat. Commun.* 8 (2017), p. 14549. DOI: 10.1038/ncomms14549.

[258] R.-F. Wang et al. “Observation of Coulomb Blockade and Coulomb Staircases in Superconducting Pr 0.8 Sr 0.2 NiO 2 Films”. In: *Phys. Rev. B* 107 (2023), p. 115411. DOI: 10.1103/PhysRevB.107.115411.

[259] W. P. Halperin. “Quantum Size Effects in Metal Particles”. In: *Rev. Mod. Phys.* 58 (1986), pp. 533–606. DOI: 10.1103/RevModPhys.58.533.

[260] J. Kim et al. “Universal Quenching of the Superconducting State of Two-Dimensional Nanosize Pb-island Structures”. In: *Phys. Rev. B* 84 (2011), p. 014517. DOI: 10.1103/PhysRevB.84.014517.

[261] C. Brun et al. “Remarkable Effects of Disorder on Superconductivity of Single Atomic Layers of Lead on Silicon”. In: *Nat. Phys.* 10 (2014), pp. 444–450. DOI: 10.1038/nphys2937.

[262] B. Jäck et al. “Critical Josephson Current in the Dynamical Coulomb Blockade Regime”. In: *Phys. Rev. B* 93 (2016), p. 020504. DOI: 10.1103/PhysRevB.93.020504.

List of Pubblication

Included in this thesis

- **Stefano Trivini**, Jon Ortuzar, Katerina Vaxevani, Jingchen Li, F. Sebastian Bergeret, Miguel A. Cazalilla, and Jose Ignacio Pascual, "Cooper Pair Excitation Mediated by a Molecular Quantum Spin on a Superconducting Proximitized Gold Film" *Phys. Rev. Lett.*, vol. 130, p. 136004, (2023), 10.1103/PhysRevLett.130.136004

Further Pubblications

- L. Litti, **Stefano Trivini**, D. Ferraro, J. Reguera "3D Printed Microfluidic Device for Magnetic Trapping and SERS Quantitative Evaluation of Environmental and Biomedical Analytes", *ACS Appl. Mater. Interfaces*, vol. 13, p. 34752-34761, (2021), DOI: 10.1021/acsami.1c09771
- Katerina Vaxevani, Jingcheng Li, **Stefano Trivini**, Jon Ortuzar, Danilo Longo, Dongfei Wang, and Jose Ignacio Pascual, "Extending the Spin Excitation Lifetime of a Magnetic Molecule on a Proximitized Superconductor" *Nano Lett.*, vol. 22, p 6075–6082, (2022), DOI: 10.1021/acs.nanolett.2c00924
- Jon Ortuzar, **Stefano Trivini**, Miguel Alvarado, Mikel Rouco, Javier Zaldivar, Alfredo Levy Yeyati, Jose Ignacio Pascual, and F. Sebastian Bergeret "Yu-Shiba-Rusinov states in two-dimensional superconductors with arbitrary Fermi contours", *Phys. Rev. B*, vol.105, p. 245403, (2022), DOI: 10.1103/PhysRevB.105.245403

Resumen extendido

La superconductividad es un fenómeno que nos ha entretenido en la investigación para mas de 100 anos y al dia de hoy siguen muchos descubrimientos y retos abiertos en el tema. El estudio de estos sistemas esta muy correlacionado con la espectroscopia de túnel, que nos perite visualizar y modificar el estado superconductor mediante excitaciones. Esto incorporado, en un microscopio a barrido túnel, nos da herramienta muy variada y potente para medir, manipular, y mapear las propiedades de los superconductores. En esta tesis primero estudiamos la superconductividad por medio de interacción con impurezas magnéticas, que dan acceso a nuevos estados cuánticos y excitaciones superconductoras. El espectro de un superconductor puede ser modificado también través del efecto de proximidad, donde un metal normal, en este caso grafeno, adquiere las propiedades del superconductor por proximidad. Con una nuevo método de manipulación de islas de plomo en grafeno somos capaces explorar como la proximidad depende de confinamiento, campos magnéticos, posición de la isla en grafeno y tamaño de las islas mismas. Estas herramienta de manipulación juntas a colaboraciones teoricas abren muchas posibilidades para modificar la superconductividad a nivel microscópico.

Conceptos de teoría y métodos experimentales

En esta tesis investigo sobre el fenómenos de superconductividad usando varios modelos para describir los experimentos. La teoría BCS describe a nivel microscópico la atracción electrón-electrón que resulta en la formación de pares llamados pares de Cooper que condensan en el estado macroscópico fundamental de BCS (BCS ground-state). Este estado tiene diferentes posibles excitaciones que podemos acceder con el STM por medio de tuneleo de electrones. Para un superconductor limpio la mínima energía de excitación es Δ para la creación de una cuasiparticula (quasiparticle). Estas excitaciones pueden ser modificadas significativamente, por ejemplo cuando cuando una impureza magnética se encuentra en la superficie del superconductor y tiene interacción de canje con las cuasiparticulas del superconductor. Esto fenómeno esta descrito por la teoría de Yu-Shiba-Rusinov, donde se trata el espín de la impureza de manera clásica, análogo a un vector con dirección fija. Esta teoría funciona bien cuando describimos átomos aislados sin anisótropo magnética y puede ser extendida para describir interacciones entre átomos. Una descripción cuántica del espín consiste en el considerar que un espín $1/2$ es isótropo en el espacio y per-

mite de describir espines con S>1/2 en presencia de anisotropia magnética. En esta tesis estudiamos el efecto conjunto de esta anisotropia magnética y del canje en una molécula magnética en interacción con un superconductor.

Hay otras maneras para modificar el espectro de un superconductor. En la interfase de un superconductor y un metal normal los procesos de reflexión de Andreev hacen que los pares de Cooper y la coherencia se trasmita en el metal normal, dando lugar al efecto de la proximidad superconductora (superconducting proximity effect). Esto esta descrito con dos clases de modelos. La diferencia es en el considerar el movimiento de los electrones balísticos, donde el camino libre medio de los electrones es mas largo del tamaño del sistema, o difusivos, donde los procesos de scattering definen un camino libre medio del electron y se pierde la información geométrica del sistema. Solucionando las ecuaciones de Bogoliubov de Gennes con condiciones al contorno (balístico) o de Usadel (difusivo) es posible calcular el espectro de excitaciones que comparamos con experimentos donde podemos modificar la geometría del sistema superconductor-normal.

En esta tesis investigamos también sobre el efecto dramático que las interacciones de Coulomb pueden tener sobre el espectro de un superconductor. Los electrones en un superconductor interaccionan por medio de interacción mediada por fonones (vibraciones del cristal), que gana sobre la una fuerza de repulsión de Coulomb a baja temperatura y energía. Para ver como estas interacciones afectan a la superconductividad hay que reducir el tamaño del superconductor. En esta tesis investigamos como en islas pequeñas (<30 nm) de Pb (superconductor) efectos de Coulomb blockade interaccionan con la superconductividad. Para describirlo damos una interpretación fenomenológica basada sobre los modelos ortodoxos para describir el tuneleo de electrones traves de junciones de tuneling dobles (double tunnel junctions, DBTJ).

Retículos Yu-Shiba-Rusinov 2D de Mn en β-Bi_2Pd modelado por funciones de green

En esta tesis estudio retículos de espines asemblados por medio de manipulación atómica en el superconductor β-Bi_2Pd . En este sistema los estados de Yu-Shiba-Rusinov (YSR) se extienden lejos de la impureza y están afectado de la anisotropia de la superficie de Fermi. La interacción entre estados de YSR es caracterizada de un splitting que depende de como las impurezas alineen sus espines. Mapeamos esto en estructuras de manganeso en 1D y 2D viendo como son afectadas de manera diferente según el alineamiento con red del substrato. Cadenas de átomos magnéticos en superconductores son muy investigados para la posible presencia de estados topológicos a los bordes. Aquí no tenemos evidencias de estados de bordes en cadenas hasta 18 atomos, donde vemos una interacción colectiva de los estados que pero satura a 5-6 átomos de longitud.

Mas interesante son las estructuras a forma de cruz de 5 átomos donde cambiamos la orientación en respecto la red atómica del substrato. Con el STM podemos construir átomo por átomo las estructura y seguir la evolución de el espectro de excitaciones. El splitting inducido por interacción aumenta de manera monotónica por cada átomo añadido a la estructura. El fenómeno esta capturado con el modelo desarrollado en nuestro grupo para describir N impurezas magnéticas en β-Bi_2Pd . Esto nos permite simular un retículo de 25 átomos construido con manipulación atómica. Donde identificamos modos colectivos de YSR con una distribución espacial esta reflejada en la simulación.

Excitación de pares de Cooper promediada por un espín cuántico molecular en un film proximitizado de Oro

Aquí analizamos el espectro a baja energía de un espín molecular acoplado con un superconductor, identificando una excitación de ruptura de pares de Cooper que no ha sido observada en STM hasta ahora. La molécula es la porfirina de hierro FeTPPCl que tiene un átomo de cloro pegado al hierro. Esta molécula tiene un espín total S=5/2 que interacciona con el superconductor dando lugar a estados de Yu-Shiba-Rusinov dentro del gap superconductor, que están separados en varias componentes, que describimos con un modelo de impureza cuántica. Además observamos picos de excitaciones fuera del gap, típicamente asociados a cambios de espín, debido a la anisotropia magnética que separa entre estados de espín con diferente proyección en z, favoreciendo un estado ground Sz=1/2.

En este trabajo damos mucha importancia a la paridad del superconductor (numero de partículas par o impar), siendo que algunas excitaciones como la de ruptura de pares de Cooper no son accesibles con electrones cuando el sistema se encuentra en el estado fundamental de BCS (par). La flexibilidad de la molécula debido a la fuerte interacción del atomo de cloro con la punta permite la modificación del acoplo entre espín y superconductor. Esto induce un cambio en las energía de excitaciones que nos permite ver una transición de fase cuántica, donde hay un cambio del estado fundamental del sistema molécula-superconductor. Esto ha sido observado muchas veces y se entiende como un estado BCS con una cuasiparticula pegada a la impureza dando un estado impar. Al cambio de ground state vemos como aparece la nueva excitación de rupturas de pares de Cooper. La clave para confirmar la natura de esta excitación es la posibilidad de modificar el tamaño del gap superconductor depositando oro en cima del vanadio, comprobando que su energía cambie con 2Δ del superconductor.

Modificar el efecto de proximidad superconductora en grafeno usando la manipulación de islas de Pb

Hasta ahora, en grafeno en su forma aislada, no ha sido observada superconductividad. Una manera utilizada para inducir la superconductividad en grafeno

es por medio de el efecto de proximidad, donde el superconductor esta depositado en cima del grafeno. En esta tesis usamos grafeno depositado en cima de carburo de silicio (SiC), que siendo polar tienes dos posibles superficies una terminada por carbono y la otra por silicio. En la cara carbono el grafeno es multi-capa, donde la orientación de las ultimas dos capas define sus propiedades electrónicas, que cambian en los varios dominios visualizado por STM. Gracias a la posibilidad de mover islas podemos estudiar como la misma proximidad esta afectada en diferentes dominios o como penetra entre un dominio a el otro. También construimos estructuras de tipo superconductor-normal-superconductor donde vemos un cambio radical del espectro al modificar el tamaño de la parte normal, empujando las islas para cerrar la estructura. Las estructuras cerradas que llamamos corrales tienen son interesantes en general para inducir superconductividad de manera localizada y reproducible en cuanto se pueden mover en la superficie. Dentro de estas zonas confinadas medimos el efecto de un campo magnético, que induce estados dentro del gap correlacionados con una diferencia de fase finita que se desarrolla a lo largo del corral.

En la cara carbono del SiC el grafeno tiene el nivel de Fermi en el punto de neutralidad y la superconductividad decae lejos de las islas en la longitud de coherencia (~ 90 nm). Esto cambia para la cara silicio, donde el grafeno esta dopado n y entonces tiene una mayor densidad electrónica al nivel de Fermi. Con un recubrimiento parcial (20-30% Pb) de la superficie del grafeno el material se comporta como un superconductor con un gap homogéneo, que depende débilmente de la estructura local. Este tipo de transición metal-superconductor ha sido descripto en trabajos teóricos y medido en transporte, pero nunca visualizado localmente.

Bloqueo de Coulomb y superconductividad

La superconductividad es debida a la atracción microscópica entre electrones promediada por fonones. Cuando la dimensión del superconductor es reducida las interacciones de Coulomb pueden competir con el estado superconductor. Bajo un tamaño critico, hypotizado por Anderson la superconductividad deja de existir. La repulsión de Coulomb también afecta el transporte de carga través de uniones túnel, como la que constituye la punta de STM acoplado a una isla de superconductor. Reduciendo el tamaño de la isla añadir un electron al sistema cuesta mas energía, dando lugar a fenómenos de bloqueo de Coulomb. Una física muy interesante esta en la interacción de estos fenómenos con la superconductividad, que todavía no esta completamente entendido y investigado experimentalmente.

En nuestro experimento tenemos dos tamaños limites, islas grandes (d>50 nm) que se comportan como superconductores bulk, y islas pequeñas (d<20 nm) en las cual vemos un Coulomb gap sin efectos de superconductividad. En los tamaños intermedios se ve como el espectro del superconductor esta modificado fuertemente con la presencia constante de una asimetría en los picos de coherencia. En estas islas hay un gap de bloqueo de Coulomb de tamaño parecido al gap superconductor. El

Coulomb gap además puede ser asimétrico en energía, a causa de una posible exceso de carga en la isla que cambia dependiendo de cambios en la función de trabajo local. Para confirmar esta interpretación movemos la isla por medio de manipulación y invertimos entre dos extremos de asimetría de manera reproducible.

Conclusiones

En esta tesis uso un conjunto de herramienta experimental, como manipulación atómica, molecular y de islas superconductoras para avanzar en el entendimiento de las excitaciones de superconductores a la escala atómica. Las condiciones controladas de un STM permiten la implementación de modelos teóricos relativamente simples que dan una idea clara de la fenomenología del sistema. El control de las excitaciones many-body en impurezas magnéticas manipuladas establece la importancia de la descripción cuántica del espín. La herramienta de manipulación de islas de Pb proporciona una plataforma potente hacia una comprensión más profunda de la superconductividad y los efectos de proximidad.